2012

Surface plasmon resonance in super-periodic metal nanostructures

Haisheng Leong

SURFACE PLASMON RESONANCE IN SUPER-PERIODIC METAL NANOSTRUCTURES

by

HAISHENG LEONG

A DISSERTATION

Submitted in partial fulfillment of the requirements
for the degree of Doctor of Philosophy in Engineering
in
The Department of Electrical and Computer Engineering
to
The School of Graduate Studies
of
The University of Alabama in Huntsville

HUNTSVILLE, ALABAMA

2012

In presenting this dissertation in partial fulfillment of the requirements for a doctoral degree from The University of Alabama in Huntsville, I agree that the Library of this University shall make it freely available for inspection. I further agree that permission for extensive copying for scholarly purposes may be granted by my advisor or, in his/her absence, by the Chair of the Department or the Dean of the School of Graduate Studies. It is also understood that due recognition shall be given to me and to The University of Alabama in Huntsville in any scholarly use which may be made of any material in this dissertation.

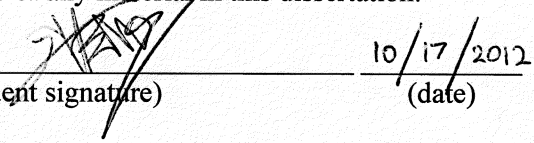

(student signature) 10/17/2012 (date)

Dissertation APPROVAL FORM

Submitted by Haisheng Leong in partial fulfillment of the requirements for the degree of Doctor of Philosophy in Electrical Engineering and accepted on behalf of the Faculty of the School of Graduate Studies by the dissertation committee.

We, the undersigned members of the Graduate Faculty of The University of Alabama in Huntsville, certify that we have advised and/or supervised the candidate on the work described in this dissertation. We further certify that we have reviewed the dissertation manuscript and approve it in partial fulfillment of the requirements for the degree of Doctor of Philosophy in Electrical Engineering.

Oct. 1st, 2012
Committee Chair
(Date)

James K. Baird

Dr. Shen

Shangping Ren

Department Chair

College Dean

Rhonda Kay Steede 10/31/12 Graduate Dean

ABSTRACT

The School of Graduate Studies
The University of Alabama in Huntsville

Degree Doctor of Philosophy in Engineering College/Dept. Engineering/Electrical and Computer Engineering

Name of Candidate Haisheng Leong

Title Surface Plasmon Resonance In Super-Periodic Metal Nanostructures

Surface plasmon resonances in periodic metal nanostructures have been investigated over the past decade. The periodic metal nanostructures have served as new technology platforms in fields such as biological and chemical sensing. An existing method to determine the surface plasmon resonance properties of these metal nanostructures is the measurement of the light transmission or reflection from these nanostructures. The measurement of surface plasmon resonances in either the transmission or reflection allows one to resolve the surface plasmon resonance in metal nanostructures. In this dissertation, surface plasmon resonances in a new type of metal nanostructures were investigated. The new nanostructures were created by patterning traditional periodic nanohole and nanoslit arrays into diffraction gratings. The patterned nanohole and nanoslit arrays have two periods in the structures. The new nanostructures are called "super-periodic" nanostructures. With rigorous finite difference time domain (FDTD) numerical simulations, surface plasmon resonances in super-periodic nanoslit and nanohole arrays were investigated. It was found that by creating a super-period in periodic metal nanostructures, surface plasmon radiations can be observed in the non-zero order diffractions. This discovery presents a new method of characterizing the surface plasmon resonances in metal nanostructures. Super-periodic gold nanoslit and nanohole arrays were fabricated with the electron beam lithography technique. The surface plasmon resonances were measured in the first order diffraction by using a CCD. The experimental results confirm well with the FDTD numerical simulations.

Abstract Approval: Committee Chair _____

Department Chair _____

Graduate Dean Rhonda Kay Gaede 10/31/12

ACKNOWLEDGMENTS

I could not accomplish this dissertation without the support from the people who have been supporting me. First and foremost, I would like to thank my advisor, Dr. Junpeng Guo, who has been a wise and knowledgeable mentor to me. His passion for the work inspired me and his guidance has always led me to the right direction in my research. On numerous accounts, he helped me overcome many obstacles in my research.

Also I would like to thank Dr. Robert Lindquist, Dr. Dashen Shen, Dr. James Baird, and Dr. Shangbing Ai for supporting me in serving in my Ph.D. committee. I would also like to thank Ms. Jackie Siniard, Ms. Linda Grubbs, Ms. Jackie Carlson and Ms. Della West for their administrative support for me to accomplish this dissertation.

I would also like to acknowledge the National Aeronautics and Space Administration (NASA) and the National Science Foundation (NSF) for supporting this research.

Finally, I would like to thank my parents for their continuous support and care throughout the course of this dissertation work.

TABLE OF CONTENTS

LIST OF FIGURES

CHAPTER 1

INTRODUCTION

Surface plasmon nanophotonics is an emerging nanotechnology area, which has been growing exponentially in the past decade due to many potential applications in sensing, information processing, solar optical energy harvesting, high density data storage, enhanced photon detection, and nonlinear optics. Surface plasmons are coherent free electron oscillations on surfaces of metals in contact with dielectric materials. The excitation of free electron oscillations on a metal surface always generates a surface electromagnetic wave that propagates along the metal-dielectric boundary. The coupled physical state between surface plasmons and photons is called the "surface plasmon-polariton". Surface plasmons are generally divided into two categories: one for propagating surface plasmons and another for non-propagating surface plasmons, which is typically called the localized surface plasmons. For localized surface plasmons, the surface plasmon resonance excitation frequencies are not only dependent on the type of metal but also on the geometrical parameters of the nanostructures.

1.1 History

The first observation of the surface plasmon resonance effect can be dated back to the Roman times, in the 4th century A.D., when gold nanoparticles were used for dyeing glasses, tinting glass windows to ruby red [1]. The color ruby red comes from the scattering of light from the embedded gold nanoparticles. In 1902, R. Wood reported the first scientific observation of surface plasmon resonance in metal gratings [2]. Later, it was called "Wood's anomaly" because the phenomena could not be explained by using the classical diffraction grating theory. In 1941, Fano connected Wood's anomaly to the excitation of surface waves [3]. Then, it was realized that the optical energy loss in metal gratings observed by Wood is associated with the excitation of coherent conduction electron oscillations in the metal structures [4-6]. Later, surface plasmon resonance excitations were achieved by using metal gratings [7] and also using a prism coupling technique [8]. Although the initial observation of surface plasmon resonance was in the visible regime, mathematical descriptions of microwave surface waves propagating along the surface of a conductor were theorized in early 1900s [9-11]. This was later backed by ingenuous rediscovery at the turn of the 21st century in both the microwave [12] and terahertz [13] regimes.

Taking advantage of the advancement of nanofabrication technologies developed by the electronics industry, the photonics community has made tremendous progress in surface plasmon photonics over the past decade, spurring many new discoveries such as sub-wavelength field confinement [14, 15], enhanced optical transmission through nanoholes in metal films [16], negative refractive index materials [17, 18] and

transformation optics [19, 20]. The progress in surface plasmonics made within the past decade has created a new research field called “metamaterials” [21].

1.2 Motivation

For biochemical and biomedical sensing applications, compact and sensitive sensors are very much needed in the field. The nanostructure surface plasmon devices and sensing technique developed in this work have potential applications in many sensing areas. When light is impinging onto a metallic film with periodically arranged nanostructure shapes that are much smaller than the wavelength, an effective electric response is generated as a result of the near-field interactions amongst the nanostructures. For the most part, observation of the surface plasmon resonance is seen by determining the resonance peak found in the 0^{th} order spectrum of the transmitted and reflected light. Here, however, by properly designing the nanostructure, manifestation of the surface plasmon resonance in the 1^{st} order spectrum can be observed. The strength and shape of the SPR in the 1^{st} order can be engineered by varying the geometrical parameters of the proposed nanostructure.

This dissertation is outlined as follows. The properties of two types of the surface plasmon resonance, surface plasmon polaritons and the localized surface plasmon and the properties of metal are discussed later in Section 1.3 to Section 1.5. In Chapter Two, the study of surface plasmon resonance properties observed from periodic metallic nanostructures is provided. By varying the geometrical parameters of the subwavelength periodic nanoslit arrays, the surface plasmon resonance properties can be slightly altered. In Chapters Three and Four, the effects of the super-periodicity were investigated on two typical nanostructures, the nanoslits and the nanoholes. The concept, theoretical and the

experimental analyses of the super-periodic nanostructures were provided in those chapters. In Chapter Five, the summary and the future implications of this research are discussed.

1.3 Surface plasmon resonance at a single metal surface

The theory of surface plasmons and the characteristics of surface plasmons in various nanostructures used in sensing are discussed in this section. First, the dispersion relation of the bulk surface plasmon wave along a single interface is introduced to provide a fundamental understanding of the properties of the surface plasmons. More complicated properties of the surface plasmons when considering the geometrical properties of the nanostructures are presented as well.

There are free electron charges on a surface of a metal that can perform coherent fluctuations which are called surface plasma oscillations [5]. The coupling of these oscillations and electromagnetic waves along the interface of a dielectric and a metal gives rise to surface waves that are known as surface plasmon-polaritons (SPPs) [22]. The resonant interaction of the plasma oscillations and the electromagnetic waves establishes the properties of the SPPs and is termed the SPR. Without resorting to quantum mechanics, the interactions of metals with electromagnetic fields and the properties of the SPPs can be sufficiently analyzed with electromagnetic theory because it is the macroscopic response of the metal that contributes mostly to the properties of the SPPs. The Maxwell equations in their general form are

$$\nabla \times \mathbf{E} = -\frac{\partial \mathbf{B}}{\partial t} \tag{1.1}$$

$$\nabla \times \mathbf{H} = \mathbf{J} + \frac{\partial \mathbf{D}}{\partial t} \tag{1.2}$$

$$\nabla . \mathbf{D} = \rho \tag{1.3}$$

$$\nabla . \mathbf{B} = 0 \tag{1.4}$$

where **E** is the electric field, **B** is the magnetic flux density, **H** is the magnetic field, **D** is the electric displacement, **J** is current density and ρ is the charge density. Because the free charges in the metal and the conductivity, σ, are already accounted for in the electric permittivity, $\varepsilon(\omega)$, the Maxwell equations in (1.2) and (1.3) become

$$\nabla \times \mathbf{H} = \frac{\partial \mathbf{D}}{\partial t} \tag{1.5}$$

$$\nabla . \mathbf{D} = 0\,, \tag{1.6}$$

and in a non-magnetic medium, the relative permeability, μ_r has the value 1.

For a linear, homogeneous and isotropic medium, the Hemholtz equation for a transverse magnetic (TM) wave takes the form

$$\nabla^2 \mathbf{H}(r) + k^2 \mathbf{H}(r) = 0\,. \tag{1.7}$$

The solution for the magnetic field, **H**, that satisfies the wave equation is a monochromatic plane wave

$$\mathbf{H}(r) = H_0 e^{-j\mathbf{k}\cdot\mathbf{r}}\,. \tag{1.8}$$

The simplest geometry sustaining SPPs is the single interface between a dielectric material with positive real dielectric, ε_d, and a metal, $\varepsilon_m(\omega)$, as shown in Figure 1.1.

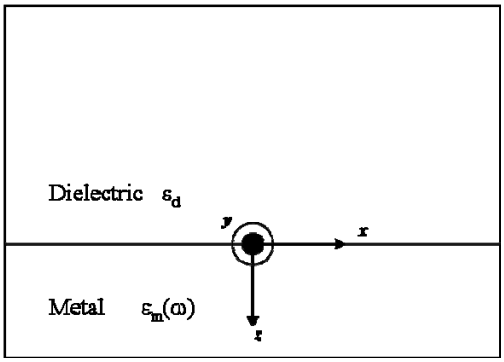

Figure 1.1 Schematic diagram of a single interface between a metal and a dielectric. The plane wave is propagating in the positive x-z plane and its magnetic field is polarized in the positive *y*-direction.

Assuming that the TM wave is propagating in the x-z plane with the magnetic field, **H**, polarized in the positive *y*-direction, it has the form

$$H_y(z) = H_0 e^{-j(\beta x+\gamma z)}. \tag{1.9}$$

Substituting (1.9) into (1.1) and (1.5), the following equation sets in both half spaces are

$$H_y(z) = AH_0 e^{-j(\beta x+\gamma_1 z)} \tag{1.10a}$$

$$E_x(z) = \frac{\gamma_1 AH_0}{\omega\varepsilon_d} e^{-j(\beta x+\gamma_1 z)} \tag{1.10b}$$

$$E_z(z) = -\frac{A\beta H_0}{\omega\varepsilon_d} e^{-j(\beta x+\gamma_1 z)} \tag{1.10c}$$

for z < 0 and

$$H_y(z) = BH_0 e^{-j(\beta x+\gamma_2 z)} \tag{1.11a}$$

$$E_x(z) = \frac{\gamma_2 BH_0}{\omega\varepsilon_m} e^{-j(\beta x+\gamma_2 z)} \tag{1.11b}$$

$$E_z(z) = -\frac{B\beta H_0}{\omega\varepsilon_m} e^{-j(\beta x+\gamma_2 z)}. \tag{1.11c}$$

To satisfy boundary conditions, the continuity of H_y, E_x and εE_z at z = 0 requires that $A=B$ and

$$\frac{\gamma_1}{\varepsilon_d} = \frac{\gamma_2}{\varepsilon_m}. \tag{1.12}$$

The wave equation, (1.7) yields the following in both half spaces:

$$k_0^2 \varepsilon_d = \beta^2 + \gamma_1^2 \tag{1.13a}$$

$$k_0^2 \varepsilon_m = \beta^2 + \gamma_2^2. \tag{1.13b}$$

Combining (1.13) and (1.12) results in the central point of this discussion, the dispersion relation of the SPPs propagating at the interface between a metal and a dielectric,

$$\beta = k_0 \sqrt{\frac{\varepsilon_d \varepsilon_m}{\varepsilon_d + \varepsilon_m}}. \tag{1.14}$$

For the SPPs to be confined at the surface of the metal, both the dielectric permittivity, ε_d, and the metal permittivity, ε_m, have to be in opposite signs where the $\mathrm{Re}[\varepsilon_m] < 0$ due to the contribution of the surface plasma oscillations. Figure 1.2 plots the dispersion relation of the SPPs at the interface between silver with the dielectric function, $\varepsilon_m(\omega)$ and air where the permittivity, $\varepsilon_r = 1$. In this plot, the dashed and the solid lines represent the light line and the wave vector of the SPPs respectively. The light line is the dispersion relation of light in air. It can be seen that the wave vector of the SPPs lies to the right of the light line, where the SPPs could not be excited by a transverse electromagnetic wave. Thus, phase-matching methods such as the prism and grating coupling methods are used to overcome the momentum mismatch between the impinging photons and the SPPs.

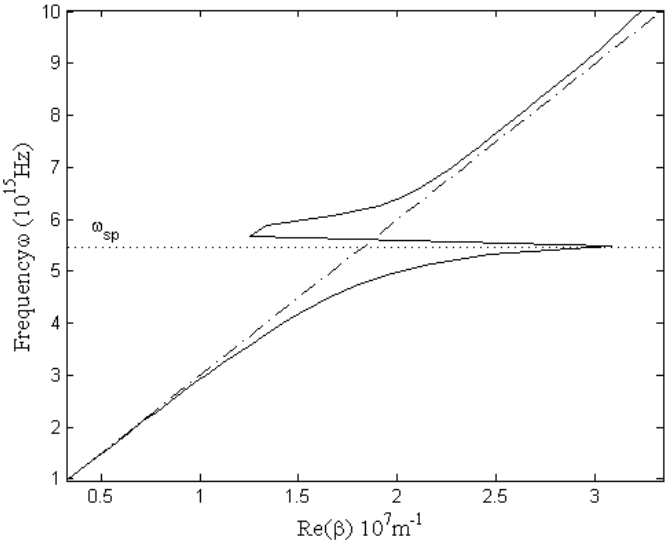

Figure 1.2 Dispersion of the surface plasmon polaritons (SPPs) at the interface between silver and air.

At low frequencies, the SPPs wave vector is close to the light line, but remains larger than it. In this regime, the SPPs inherit the properties of a grazing-incidence light field, also known as the Sommerfeld-Zenneck wave. As the frequency approaches the surface plasmon frequency of a free-electron model,

$$\omega_{sp} = \frac{\omega_p}{\sqrt{1+\varepsilon_d}} \tag{1.14}$$

where ω_p is the plasma frequency of the metal, the wave vector of the SPPs begins to increase very quickly. For a free-electron model with negligible damping, the SPPs would extend to infinity as it approaches the surface plasmon frequency. The mode would thus be localized as the group velocity of the SPPs approaches zero. However, in actuality there is no negligible damping. Therefore the SPPs at the surface plasmon frequency is finite. Above the plasma frequency of the metal, the light radiates into the

metal as the electron plasma could not oscillate quickly enough to screen out the light. Here the plasma frequency is

$$\omega_p = \frac{ne^2}{\varepsilon_0 m} \tag{1.15}$$

where *n*, *e* and *m* are the density of the free electrons, electron charge and electron mass respectively. Due to the damping properties in the metal, the wave vector of the SPPs is also damped, preventing the SPPs from propagating far without losing energy. The damper in the metal is usually described as the imaginary part of the dielectric function, $\varepsilon_m(\omega)$, which can be expressed as a complex function, $\varepsilon_m = \varepsilon_m^{'} - j\varepsilon_m^{''}$. As a result, the wave vector of the SPPs can be decomposed into real and imaginary parts. Assume that $\left|\varepsilon_m^{'}\right| > \varepsilon^{''}$, a complex $\beta = \beta^{'} - j\beta^{''}$ is obtained with

$$\beta^{'} = \frac{\omega}{c}\left(\frac{\varepsilon_m^{'}\varepsilon_d}{\varepsilon_m^{'} + \varepsilon_d}\right)^{1/2} \tag{1.16}$$

$$\beta^{''} = \frac{\omega}{c}\left(\frac{\varepsilon_m^{'}\varepsilon_d}{\varepsilon_m^{'} + \varepsilon_d}\right)^{3/2} \frac{\varepsilon^{''}}{2(\varepsilon_m^{'})^2}, \tag{1.17}$$

where *c* is the speed of light. The imaginary part of the β, corresponds to the propagating length of the SPP which is given by

$$L = \frac{1}{2\beta^{''}}. \tag{1.18}$$

In Figure 1.3, the imaginary part of the SPP wave vector is plotted. At low frequencies, the $\beta^{''}$ is small, but at frequencies near the surface plasmon frequency, the $\beta^{''}$ is large. This means that the propagation lengths of the SPPs at low frequencies are much higher

than the propagation lengths of the SPPs at frequencies near the surface plasmon frequency.

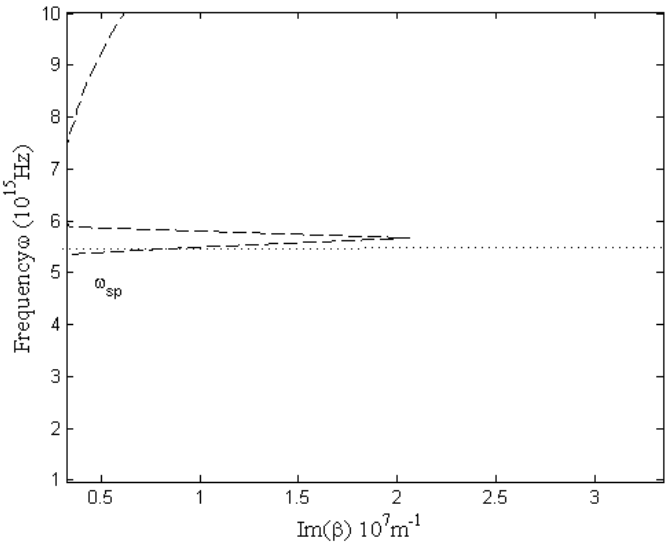

Figure 1.3 The imaginary part of the SPPs wave vector, indicating loss due to damping in the metal.

The SPPs fields in both mediums decrease exponentially with *exp(-|γ||z|)*, away and normal to the surface of the metal. Due to the relations that the wave vector β is greater than the k_0 and the real part of $\varepsilon_m(\omega)$ is less than one, the normal components of the wave vectors in both the dielectric and metal are imaginary. The value of the penetration depth in both mediums at which the field decreases to 1/e are given by

$$\delta_d = \frac{\lambda}{2\pi}\left(\frac{\varepsilon_m + \varepsilon_d}{\varepsilon_d^2}\right)^{1/2} \tag{1.19a}$$

in the dielectric and

$$\delta_m = \frac{\lambda}{2\pi}\left(\frac{\varepsilon_m + \varepsilon_d}{\varepsilon_m^2}\right)^{1/2} \tag{1.19b}$$

in the metal. From (1.13), one can see that for large values of β, the field is tightly confined to the surface in both media, while at small values of β, the field extends far into the dielectric space. However, when quantifying energy confinement at the surface of the metal, one should account for the energy within the metal. This can be quantified by calculating the spatial distribution of the electric energy density, u_{eff}, which is given by

$$u_{eff} = \frac{1}{2}\mathrm{Re}\left[\frac{d(\omega\varepsilon)}{d\omega}\right]_{\omega_0} \langle \mathbf{E}(\mathbf{r},t).\mathbf{E}(\mathbf{r},t)\rangle \qquad (1.20)$$

where $\langle \mathbf{E}(\mathbf{r},t).\mathbf{E}(\mathbf{r},t)\rangle$ represents the field-averaging over one optical cycle and ω_0 is the frequency evaluated. Figure 1.4 and Figure 1.5 show the field characteristics of the SPPs at the interface between gold and air. The magnetic field is polarized in the *y*-direction, perpendicular to the *x*-*z* plane and is oscillating along the surface of the metal with the field extending far into the air space. Near the surface plasmon frequency, the field is more confined to the surface and enhanced, as expected. However, as shown in Figure 1.5, the SPPs near the surface plasmon frequency has a smaller propagation length than the SPPs at lower frequencies. This is a typical trade-off between confinement and propagation length. The confinement of the SPPs field is crucial in enhancing the sensitivity of the SPR biosensor and will be discussed later in this chapter.

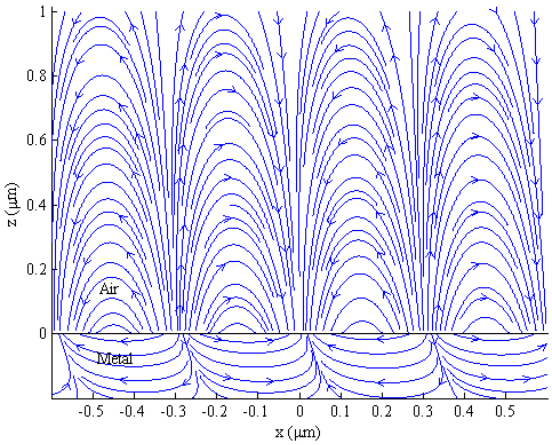

Figure 1.4 The electric field vectors of the SPPs are calculated. The calculations show the electric field lines moving from the positively charged ions to the oscillating conduction electrons.

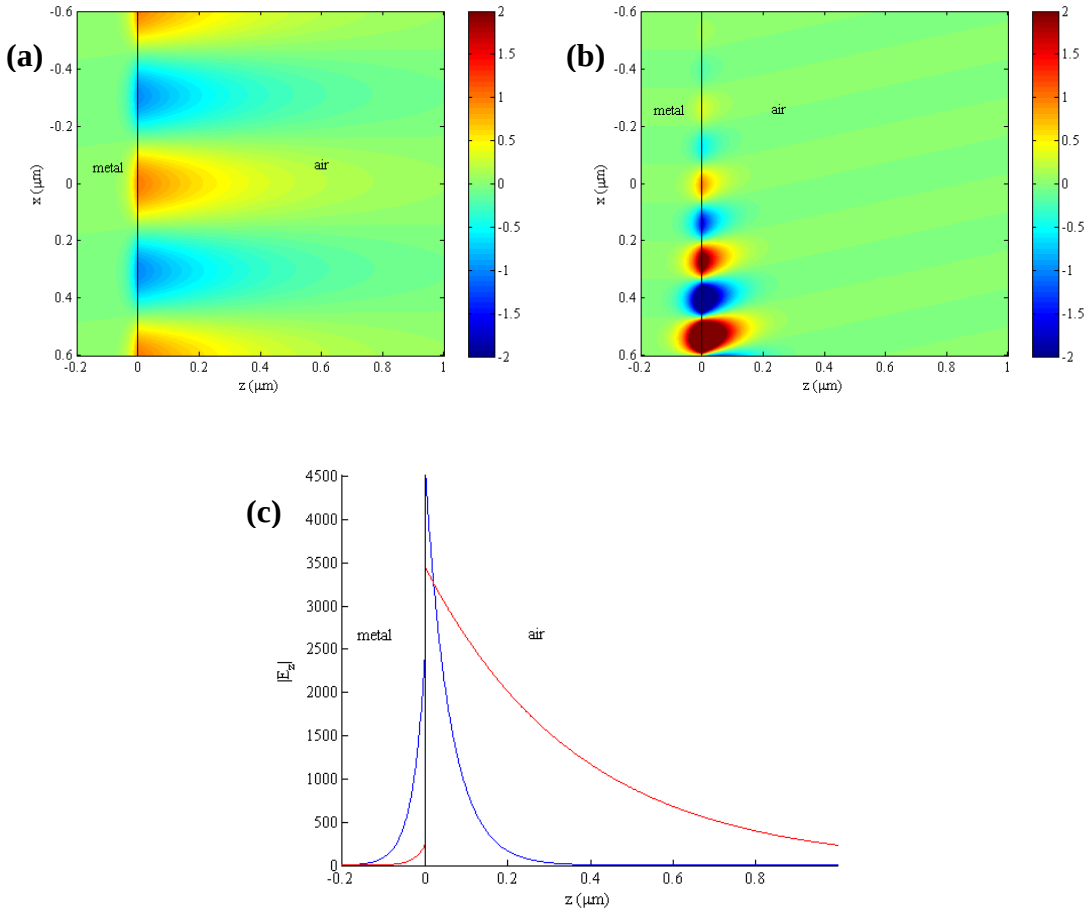

Figure 1.5 Confinement versus the propagation length. The magnetic field of the SPP at the wavelength (a) 633 nm and (b) 363 nm. Comparing (a) and (b), the magnetic field in (b) is much stronger than that in (a), but decay rate of the field in (a) is much slower than in (b), (c) the field confinement at the interface of the metal and air for the frequencies near the surface plasmon frequency (blue) and at a lower frequency (red).

1.4 Surface plasmon resonance on a thin metal film

SPPs on a smooth metal surface cannot be excited directly by light since the transverse momentum required to excite the SPPs is much greater than incident momentum. This can be seen from Figure 1.2, where the incident longitudinal wave vector, $k_x = k \sin \theta$, is always to the left of the SPP wave vector when exciting the SPPs at the interface between the incident medium and the metal. Exciting the SPPs, however can be achieved by implementing a three layer system, where a metal is sandwiched by two dielectrics with different dielectric constants. The common and well-known configuration that is used to excite SPPs is the Kretschmann configuration. It consists of a prism made of high refractive index material and a thin metal film on the base of the prism. Light incident on the metal film through the prism at a certain angle can excite a propagating surface plasmon wave along the metal-air interface. As shown in Figure 1.6, the light line of the glass is greater than the wave vector of the SPPs at the metal-air interface and thus can be excited by varying the angle of incident light. However, the SPPs at the interface between metal and prism cannot be excited by light from the incident dielectric. This coupling scheme is also known as the attenuated total internal reflection, which involves the tunneling of the fields of the excitation light through the metal and onto the metal-air interface. The SPPs manifest itself as a dip in the reflected light. This dip is due to the destructive interference between a leakage radiation and the reflected light where ideally, the dip is a perfect zero. But SPPs excited by prism coupling are leaky waves; the energy is lost not only due to absorption in the metal but also leakage of radiation into the prism. At a certain optimal metal film thickness, the dip is perfectly zero such that the leakage radiation is not observed.

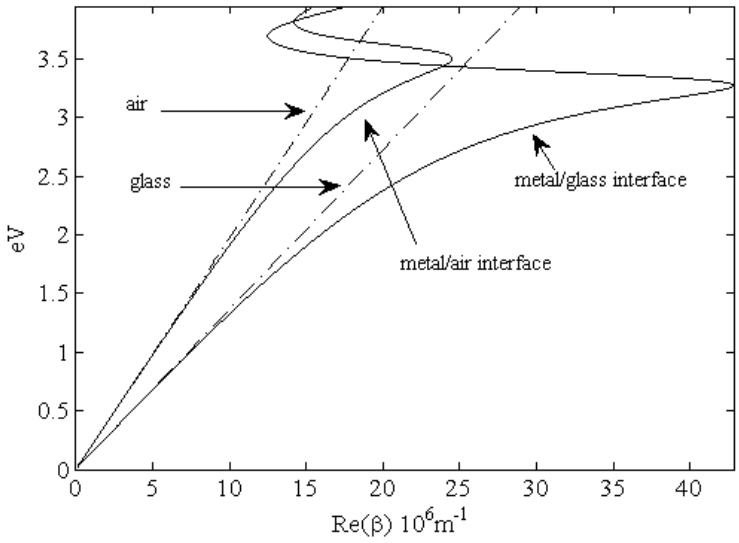

Figure 1.6 Dispersion relation of the SPPs at both the metal-air interface and metal-glass interface of the Kretschmann configuration. The dashed lines represent the light line of air and glass and the solid lines represent the propagation constant of the SPPs.

Using Fresnel equations, an analysis of the radiation loss due to absorption in the metal and leaky waves have shown that the optimum thickness can be achieved by equating the two losses, leaky radiation and absorption to each other. Assuming that $\left|\mathbf{R}e\left[\varepsilon_m\right]\right| >> 1$ and $\left|\mathbf{I}m\left[\varepsilon_m\right]\right| << \left|\mathbf{R}e\left[\varepsilon_m\right]\right|$, the Fresnel reflection coefficient can be approximated with the Lorentzian

$$R = 1 - \frac{4\Gamma_L \Gamma_{abs}}{\left[\beta - \left(\beta_0 + \Delta\beta\right)\right]^2 + \left(\Gamma_L + \Gamma_{abs}\right)^2}. \tag{1.21}$$

Γ_L is loss due to leakage radiation into the prism and Γ_{abs} is loss due to absorption in the metal [22]. It can be seen from (1.21) that there is a shift $\Delta\beta$ in the SPP wave vector at metal interface from the value, β_0, calculated for a semi-infinite metal. The imaginary part of the shift gives an additional damping to the loss due to the metal. Ultimately, it is

desired that Γ_L is zero. Reducing backscattering fields into the prism by optimizing the film thickness achieves this.

1.5 Surface plasmon resonance in metallic nanostructures

In the previous section, the properties of the bulk surface plasmon on a metal film were reviewed when the width and length of the metal film are much larger than the incident wavelength. In this section, however, the surface plasmon properties are reviewed when the dimensions of the nanostructure are taken into consideration. In general, this type of surface plasmon resonance is due to the localized surface plasmons (LSP) which are non-propagating excitations coupled between the electromagnetic wave and the free electrons on the metallic nanostructure [23]. At resonance, the curved surface of the structure exerts a restoring force on the driven electrons that leads to field enhancement in and outside of the particle. For gold and silver nanoparticles, the resonances occur in the visible region of the electromagnetic spectrum.

When the size of the particle is much smaller than the wavelength, the quasi-static condition can be applied, where the field is varying very slowly such that the phase of the oscillating field is constant over the region of the particle. For a sphere, the electric fields can be obtained by solving the Laplace equation, $\nabla^2\Phi = 0$, from which the electric field $E = -\nabla\Phi$. The general solution then is of the form,

$$\Phi(r,\theta) = \sum_{l-0}^{\infty} \left[A_l r^l + B_l r^{-(l+1)} \right] P_l(\cos\theta), \tag{1.22}$$

where $P_l(\cos\theta)$ are the Legendre Polynomials of order l, and θ is the angle between position vector **r** and the z-axis. Due to the requirement that the field at the origin of the sphere has to be finite, the potentials inside, Φ_{in}, and outside, Φ_{out}, takes the form

$$\Phi_{in}(r,\theta)=\sum_{l=0}^{\infty} A_l r^l P_l(\cos\theta) \tag{1.23a}$$

$$\Phi_{out}(r,\theta)=\sum_{l=0}^{\infty}\left[B_l r^l + C_l r^{-(l+1)}\right]P_l(\cos\theta). \tag{1.23b}$$

The coefficients can then be determined from the boundary conditions when $r\to\infty$ and when at the surface of the sphere, $r=a$. As r approaches infinity, it is required that the $B_1 = E_0$ and $B_l = 0$ for $l \neq 1$.

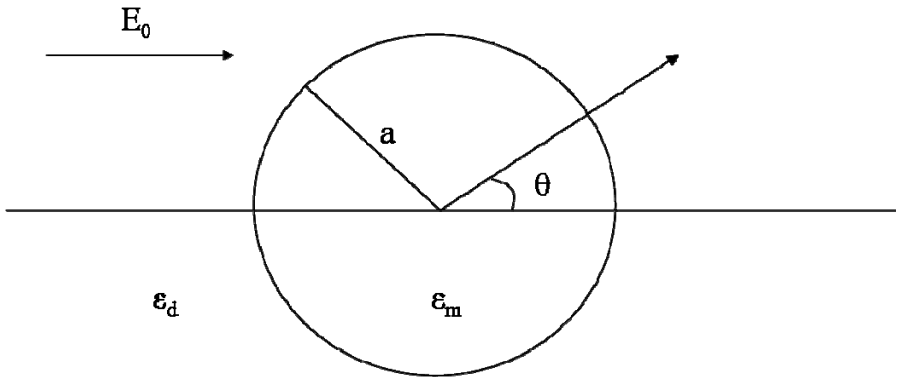

Figure 1.7 A metal nanosphere embedded in a dielectric medium.

Applying the boundary conditions at $r = a$, the tangential components of the electric field have to be continuous,

$$-\frac{1}{a}\frac{\partial\Phi_{in}}{\partial\theta}\bigg|_{r=a} = -\frac{1}{a}\frac{\partial\Phi_{out}}{\partial\theta}\bigg|_{r=a}, \tag{1.24a}$$

and the normal components of the displacement field have to be continuous as well,

$$-\varepsilon_0\varepsilon_m \left.\frac{\partial \Phi_{in}}{\partial \theta}\right|_{r=a} = -\varepsilon_0\varepsilon_d \left.\frac{\partial \Phi_{out}}{\partial r}\right|_{r=a}. \tag{1.24b}$$

From the boundary conditions, the potentials inside and outside are

$$\Phi_{in} = -\frac{3\varepsilon_d}{\varepsilon_m + 2\varepsilon_d} E_0 r\cos\theta \tag{1.25a}$$

$$\Phi_{out} = -E_0 r\cos\theta + \frac{\varepsilon_m - \varepsilon_d}{\varepsilon_m + 2\varepsilon_d} E_0 a^3 \frac{\cos\theta}{r^2} \tag{1.25b}$$

The total field outside the sphere can be described as the superposition of the incident field and the field induced by a dipole with the dipole moment **p**, as

$$\mathbf{p} = 4\pi\varepsilon_0\varepsilon_d a^3 \frac{\varepsilon_m - \varepsilon_d}{\varepsilon_m + 2\varepsilon_d} E_0 . \tag{1.26}$$

With the definition of the $\mathbf{p} = \varepsilon_0\varepsilon_d\alpha\mathbf{E}_0$, with α defined as the polarizability, α, can be written as

$$\alpha = 4\pi a^3 \frac{\varepsilon_m - \varepsilon_d}{\varepsilon_m + 2\varepsilon_d}. \tag{1.27}$$

From this equation, the LSP resonance can be characterized. In Figure 1.8, the absolute value of α for a gold nanosphere with 50 nm radius is plotted as a function of wavelength. The electric permittivity response of the gold is obtained from the Lorentz-Drude model [24] which fits its value to the experimental data from the handbook of optics [25]. The polarizability of the gold nanosphere undergoes a resonant feature at the wavelength, λ = 535 nm, when the absolute value of the denominator is at the minimum, which under a small varying $\mathrm{Im}(\varepsilon_m)$, the condition is

$$\mathrm{Re}\left[\varepsilon_m(\lambda)\right] = -2\varepsilon_d , \tag{1.28}$$

which is known as the Fröhlich condition. This shows that the resonance is dependent on the surrounding electric permittivity. As ε_d increases, the resonance shifts to a longer wavelength. Dielectric materials cannot undergo this resonance because of the absence of the free electrons that contribute to the negative part of the electric permittivity.

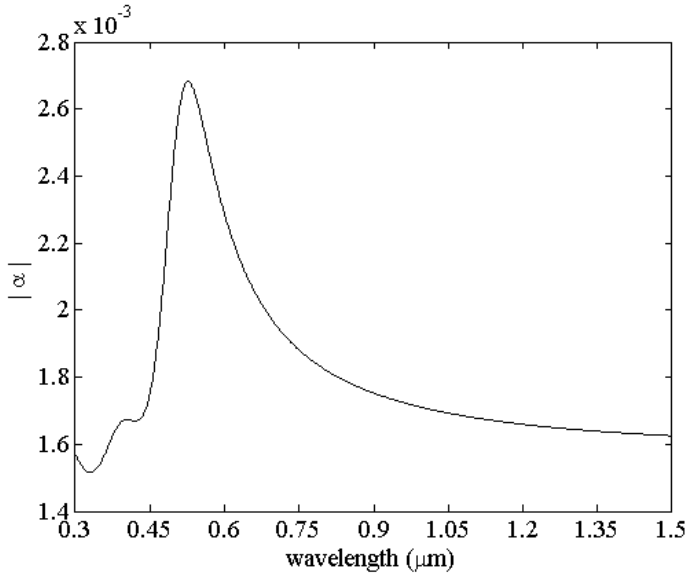

Figure 1.8 Absolute value of the polarizability α of the gold nanosphere with 50 nm radius versus the wavelength.

Also, from the dipole moment, equation (1.26), the electric field surrounding the metallic sphere is at the strongest when in resonance. Figure 1.9 plots the electric field intensity of the gold nanospheres. Light is polarized in the direction of the red arrow. It is apparent that the field emanating from the nanosphere behaves similarly as a radiating electric dipole.

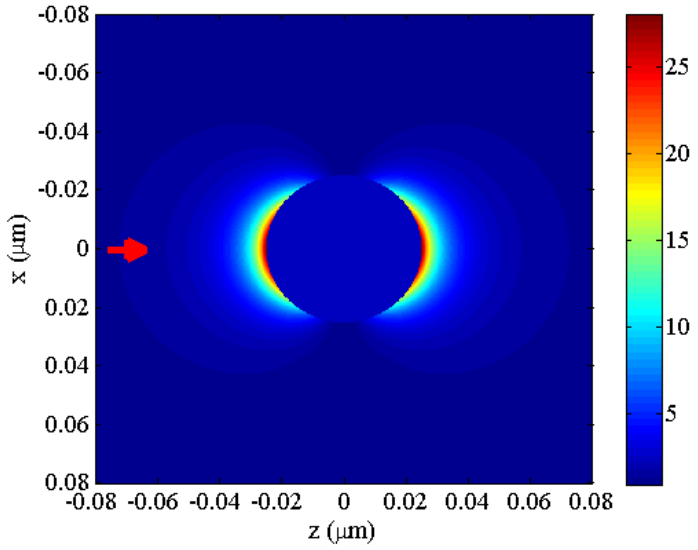

Figure 1.9 Electric field intensity distribution of the gold nanosphere at the resonance. The red arrow indicates the polarization of the incident electric field.

CHAPTER 2

SURFACE PLASMON RESONANCE IN 1-D PERIODIC METALLIC NANOSTRUCTURES

The properties of SPPs and LSP have been discussed in the previous chapter. LSP properties associated with metallic nanoparticles exhibit strong field confinement. When the nanoparticles are placed within close proximity of each other, the interaction of LSP modes of the individual nanoparticles will form new hybrid modes. For multiple nanoparticles arranged in a periodical manner, the retarded field interactions amongst them will give rise to a coherent light scattering that will give effective plasmonic properties that differ slightly from the plasmonic properties of the constituents. In this section, the SPR properties on a 1-D subwavelength periodic nanoslit array are discussed.

2.1 Collective resonances

First, collective resonances due to electric field interactions between nanoparticles are discussed. This will provide a background in understanding how the field interaction between nanoparticles can change the overall surface plasmons property of the nanoparticles array. In the previous chapter, the surface plasmons properties of a metallic sphere can be determined from its polarizability, which is described in equation (1.27).

In an array of metallic spheres, the retarded dipolar interactions between them change the collective surface plasmons properties of the metallic spheres. The contribution of the retarded dipolar interactions between the metallic spheres can be explained via the coupled dipole method [26]. The induced polarization, $\mathbf{P_i}$, in each sphere in the presence of an applied field, $\mathbf{E}_{inc,i}$, is $\mathbf{P}_i = \alpha_i \mathbf{E}_{loc,i}$ (where $i = 1,2,\ldots,N$), where $\mathbf{E}_{loc,i}$ is the sum of incident and retarded dipolar fields of the metallic spheres. At a specific wavelength, the local field,

$$\mathbf{E}_{loc,i} = \mathbf{E}_{inc,i} + \mathbf{E}_{dipolar,i} = \mathbf{E}_0 e^{i\mathbf{k}\bullet\mathbf{r}_i} - \sum_{\substack{j=1 \\ j\neq i}}^{N} \mathbf{A}_{ij}.\mathbf{P}_j \tag{2.1}$$

where E_0 and $\mathbf{k}$ are the amplitude of the applied field and the wavevector, $k = 2\pi/\lambda$, respectively. The dipole interaction matrix $\mathbf{A}$ is expressed as

$$\mathbf{A}_{ij} \bullet \mathbf{P}_j = k^2 e^{ikr_{ij}} \frac{\mathbf{r}_{ij} \times \left(\mathbf{r}_{ij} \times \mathbf{P}_j\right)}{r_{ij}^3} + e^{ikr_{ij}} \left(1 - ikr_{ij}\right) \frac{\left[r_{ij}^2 \mathbf{P}_j - 3\mathbf{r}_{ij}\left(\mathbf{r}_{ij} \bullet \mathbf{P}_j\right)\right]}{r_{ij}^5} \tag{2.2}$$
$$\left(i = 1,2,\ldots N,\ j = 1,2,\ldots N, i \neq j\right)$$

where $\mathbf{r}_{ij}$ is the vector from sphere i to sphere j. The polarization vectors, $\mathbf{P}$, can be determined by solving the 3N linear equations of the form

$$\mathbf{A}'\mathbf{P} = \mathbf{E}. \tag{2.3}$$

Solving for $\mathbf{P}$, the following expression for the effective polarizability is obtained.

$$\mathbf{P} = \frac{\alpha_s E_0}{1 - \alpha_s S} \tag{2.4}$$

where

$$S = \sum_{spheres} e^{ikr} \left[\frac{\left(1 - ikr\right)\left(3\cos^2\theta - 1\right)}{r^3} + \frac{k^2 \sin^2\theta}{r} \right]. \tag{2.5}$$

This collective behavior of the metallic nanoparticle arrays can be seen in the extinction spectra of the metallic nanoparticle arrays. The extinction spectra is proportional to the absorption spectrum, $A = 1\text{-}R\text{-}T$, where R and T represent the reflectance and transmittance of the spectrum respectively. The absorption spectrum of the array of metallic nanoparticles exhibits a more sharp resonance linewidth than that of the single nanoparticle due to the suppression of the radiative damping [27]. The same concept can be applied to the array of metallic nanoholes – where the surface waves generated by each aperture in the metallic film interact with the other surface waves generated by the other apertures. Thus, not only does the overall electric response of the perforated metal film differ slightly from that of a single hole, but the fields are enhanced as well. In the next section, the SPR in a subwavelength grating is investigated. The results of this investigation would provide some insight into designing the super-periodic nanoslits.

2.2 Surface plasmon resonance in subwavelength metal nano-gratings

It is known that the periodicity in gratings can provide the required momentum to excite the surface plasmon polaritons (SPPs). When the period of the grating is smaller than the wavelength, the periodicity of the grating can alter or split the dispersion relation of the SPPs into multiple bands [22]. The dispersion relation of the perturbed SPPs in sinusoidal metallic gratings [28] and subwavelength Gaussian grooves [29,30] have been investigated with the analytical model based upon the Chandezon method [31]. The study of the dispersion relation for SPPs in optically thick lamellar transmission gratings have shown that localized SPP modes can be excited within the nanoslits [32]. The dispersion relation of a semi-infinite thick sinusoidal metallic grating in the Otto configuration was studied by Masale [33] and the dispersion relation of the SPP in thin metal films which

are corrugated on both sides has been investigated by Schröter and Heitmann [34]. Here, the SPR in a subwavelength grating is investigated under the Kretschmann configuration. The subwavelength grating is a rectangular subwavelength grating that is etched into a gold metal film, with its period and thickness smaller than the wavelength. Because the period is much smaller than the wavelength, the subwavelength grating can be regarded as effective materials [35-37]. The rectangular subwavelength grating is placed directly on top of a prism with no intermediate metal layer in between the grating and the prism. Light is incident upon the grating through a high refractive index prism as shown in Figure 2.1. The grating has the following parameters: the thickness of the grating, d, the period of the grating, Λ, and the fill factor, f. The fill factor is defined as the ratio of the slit width to the period of the grating. The subwavelength grating is illuminated with a transverse magnetic (TM) polarized 850 nm wavelength laser at the incidence angle, $\theta_{inc.}$ The refractive index of the prism is 1.723 and the refractive index of the dielectric material in the exiting medium and within the slits is 1.333. The electric permittivity of the gold at 850 nm is -24.830-2.239i taken from Lorentz-Drude model [24].

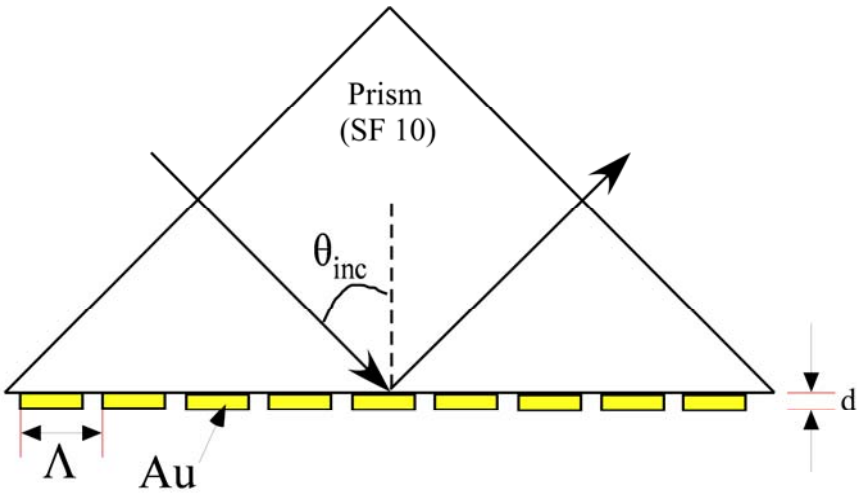

Figure 2.1 Diagram illustrating the subwavelength gold grating in the Kretschmann configuration.

The reflection, transmission and absorption of the subwavelength grating versus the angle of incidence are calculated. The numerical technique used for calculating these is the well-known Fourier modal method (FMM) [38-44]. This technique is also known as the rigorous-coupled wave analysis (RCWA), which expands the fields and the electric permittivity into Fourier components with a large finite number of modes. The coefficients of the fields are obtained by solving the eigenvalue problem and satisfying the boundary conditions. Use of this method to calculate the periodic metallic nanostructures have been successfully confirmed with experiments [45-48]. The convergence of the numerical results is validated with 121 Fourier modes retained in the calculations.

Typically, the SPR can be seen by tracking the dip in the reflectance in the Kretschmann configuration. For a uniform thin metal film, at a specific wavelength, the excitation of SPPs is known when the reflectance is at the minimum at a certain angle of incidence. Hence, by tracking the angle of incidence of which the minimum reflectance

takes place, the dispersion relation of a thin subwavelength grating can be investigated. No higher diffraction orders are radiated at that wavelength. Using this method, the overall behavior of the SPP in rectangular subwavelength grating can be found [49]. Figure 2.2 shows the reflectance, transmittance and absorption as functions of the incidence angle for a uniform gold film and a subwavelength rectangular gold grating. Absorption is defined as the total energy loss of the system, A = 1-R-T, where and A, R, and T, represents the absorption, reflectance and transmittance, respectively. Both the uniform thin gold film and subwavelength grating are 50 nm thick. The period of the grating is 200 nm and the width of the dielectric filled slits is 40 nm, which results in a fill factor of 0.2. Figure 2.2(a) shows that the minimum in the reflectance spectrum occurs at the incidence angle of 53.7°, the angle where the SPPs are excited. The angle where the minimum occurs for the subwavelength grating is at the incidence angle of 51.2° as shown in Figure 2.2(b). The reduction in the SPR angle indicates that less momentum is required for matching the momentum of the effective SPPs in the subwavelength grating. The reduction in the SPPs propagation constant can be explained as the localization of the free electrons in the grating has increased the intrinsic oscillation frequency of the bulk plasma frequency of the effective structured metal film, equivalent to the increase in the bulk plasma frequency in the Drude model. The increase in the bulk plasma frequency results in a more negative real part of the electric permittivity. The smaller the value of the real part of the electric permittivity is, the smaller the SPPs propagation constant, similar to shifting the excitation optical frequency to a lower frequency. Comparing the reflection curve of the subwavelength grating with that of the uniform thin film, it can be seen that the subwavelength grating exhibit a much

sharper resonance than that of the uniform thin film. This sharper SPR indicates that there is less attenuation along the subwavelength grating. For this case, it is shown that the effective SPPs excited in the subwavelength grating is less confined to the surface and is less lossy than the SPPs excited at the interface of the thin metal film.

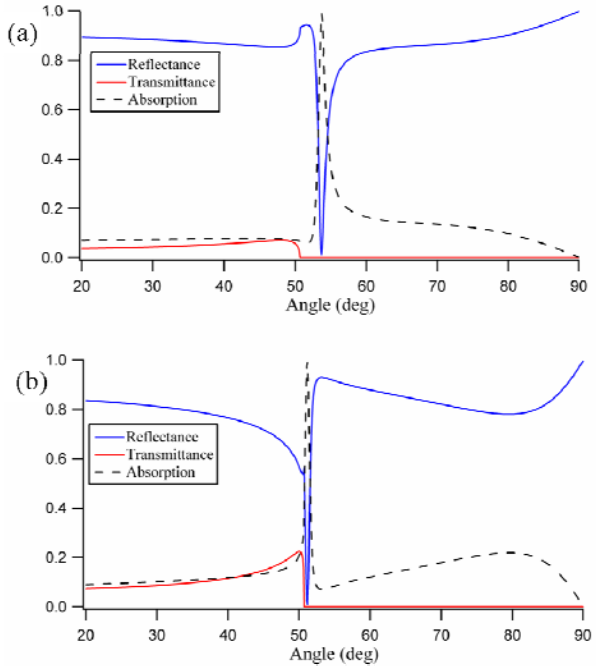

Figure 2.2 Reflectance, transmittance and absorption as functions of the incidence angle of (a) uniform gold film and (b) subwavelength grating gold film with the fill factor = 0.2. The solid blue and red curves represent the reflectance and transmittance respectively, and the dashed curve represents the absorption in the metal films.

Fixing the period of the structure at 200 nm and the metal thickness at 50 nm the fill factor of the grating is varied from 0 to 0.9. Again, the fill factor, f, is defined as the ratio of the slit width to the grating period. Figure 2.3 show the reflectance, transmittance and absorption of the subwavelength grating versus the incidence angle for different fill factors varying from 0 to 0.9. In Figure 2.3(a), where $f = 0$, the grating is essentially a

uniform film. The SPR angle is 53.7°. With Figure 2.3(a) as the base for comparison, one can see how the SPR angle evolves with the change in fill factor. The SPR shifts to the incidence angles of 52.1°, 51.2° and 50.7° for the fill factor f = 0.1, 0.2 and 0.3, respectively. As the fill factor is further increased, the SPR angle approaches 50.68°, which is the critical angle for total internal reflection between the high index prism and the low index dielectric material on the other side of the subwavelength grating. The progressive shift of the SPR angle towards the critical angle of total internal reflection indicates that less momentum is required to excite the effective SPPs in the subwavelength grating. This behavior is due to the increase in the bulk plasma frequency in the effective medium in the Drude model caused by the subwavelength grating. The increase in bulk plasma frequency results in a lesser SPPs mode confinement at the surface. As the fill factor further increases, the total internal reflection dominates and the SPR disappears near the critical angle. However, another SPR occurs at the large angle of incidence (see f = 0.3, 0.4 and 0.5). This SPR is probably due to the coupling between the localized SPP and the propagating SPP. For the fill factor from 0.6 to 0.9, the SPR is negligible because there are very small amounts of metal in the subwavelength grating.

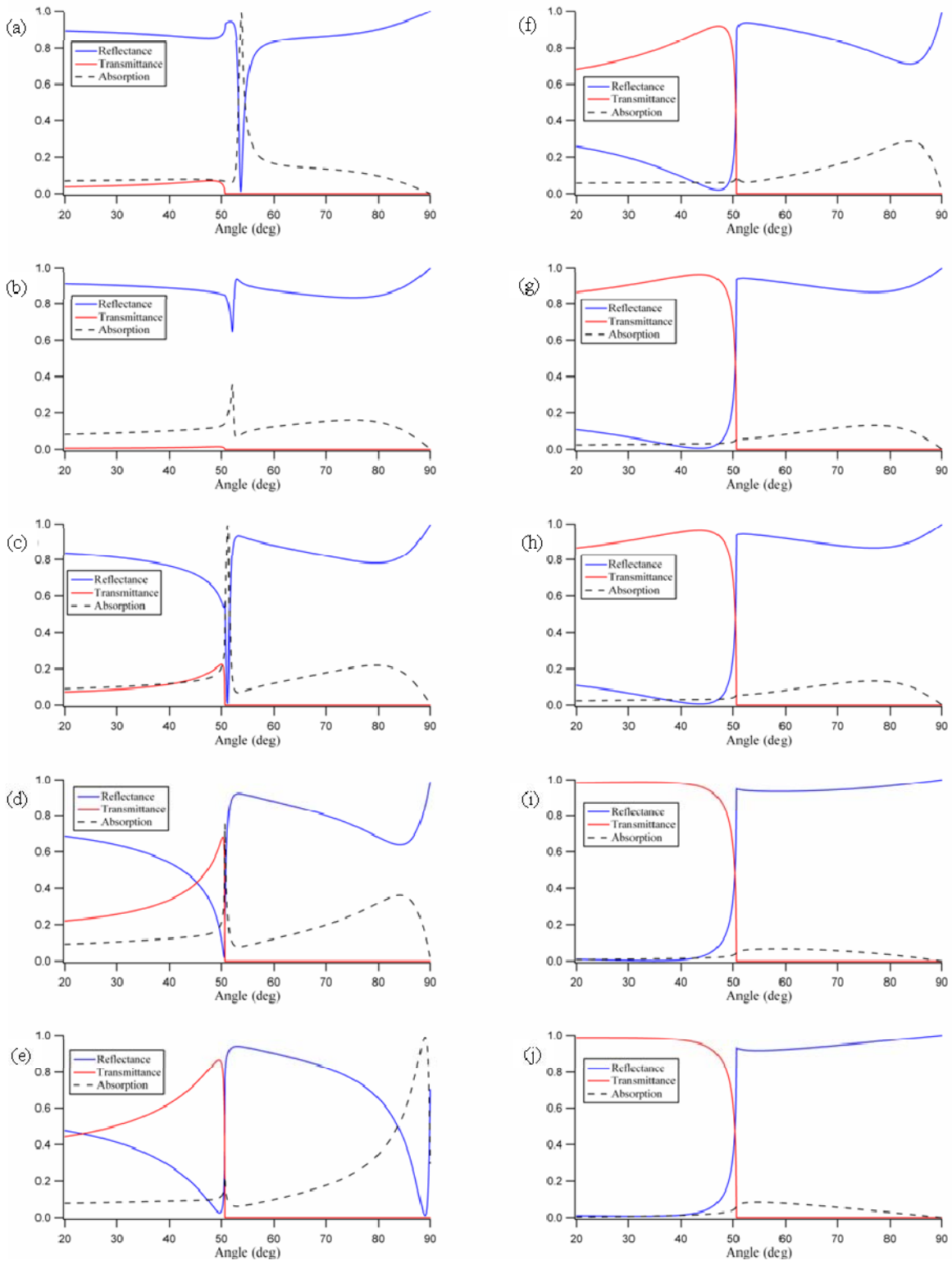

Figure 2.3 Surface plasmon resonance curves in the metal nanogratings of different fill factors: (a) f = 0, (b) f = 0.1, (c) f = 0.2, (d) f = 0.3, (e) f = 0.4, (f) f = 0.5, (g) f = 0.6, (h) f = 0.7, (i) f = 0.8, and (j) f = 0.9.

Keeping the fill factor at f = 0.2, and the thickness of the film at 50 nm, the reflectance and absorption of the reflectance and absorption as a function of the incidence angle for the period varying from 100, 150, 200 and 250 nm is plotted. Figure 2.4(a) shows the calculated reflectance versus the angle of incidence. Figure 2.4(b) shows the absorption versus the angle of incidence. It is clearly seen that as the period of the grating increases, the SPR occurs at a smaller incidence angle, implying that less momentum is required to match the momentum of the SPPs. The strongest SPR occurs when the period of the subwavelength grating is 200 nm, where maximal coupling between the incident light and the SPPs occur in the subwavelength grating. As the period increases toward the half of the wavelength, the SPR gradually diminishes because of the diminishing coupling between the incident optical wave and SPP wave.

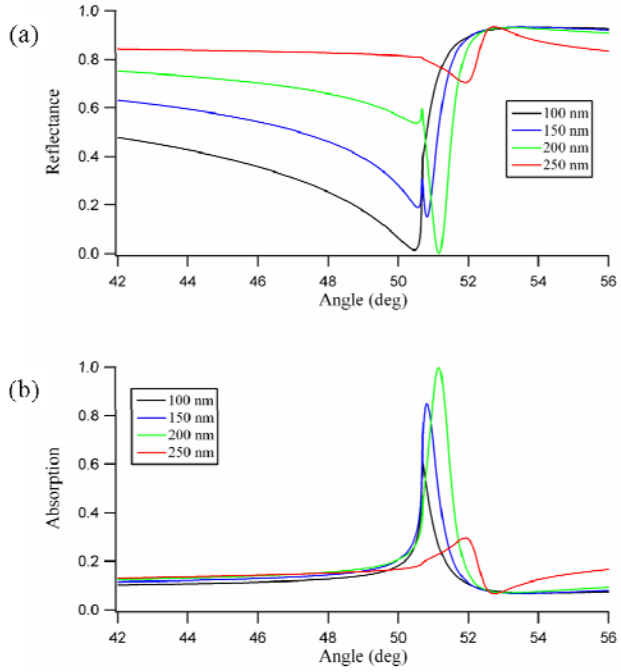

Figure 2.4 (a) Optical power reflection and (b) absorption from the gold metal nanogratings with different nanograting periods.

Fixing the fill factor of the subwavelength grating at f = 0.2, and the subwavelength grating at 200 nm, the reflectance and absorption versus the angle of incidence for subwavelength grating is calculated with thickness of different values, from t = 30, 35, 40, 50 and 60 nm. Figure 2.5(a) shows the reflectance as a function of the incidence angle while absorption as a function of the incidence angle is plotted in Figure 2.5(b). From Figure 2.5(b), the absorption appears to be the strongest at the incidence angle of 51.2° and at a thickness of 50 nm. This again shows that the maximum energy transfer from the incident light occurs at this thickness. Also seen is that the SPR angle increases slightly as the metal film thickness increases. This is because the thicker films support more tightly confined propagating SPPs. A similar trend is seen for uniform metal films, although the change in SPR angle is not as dramatic as the change observed when the period is changed as has been shown earlier from the Lorentzian type relation, equation 1.21, where the FWHM and the strength of the SPR dip are affected by the thickness of the metal film.

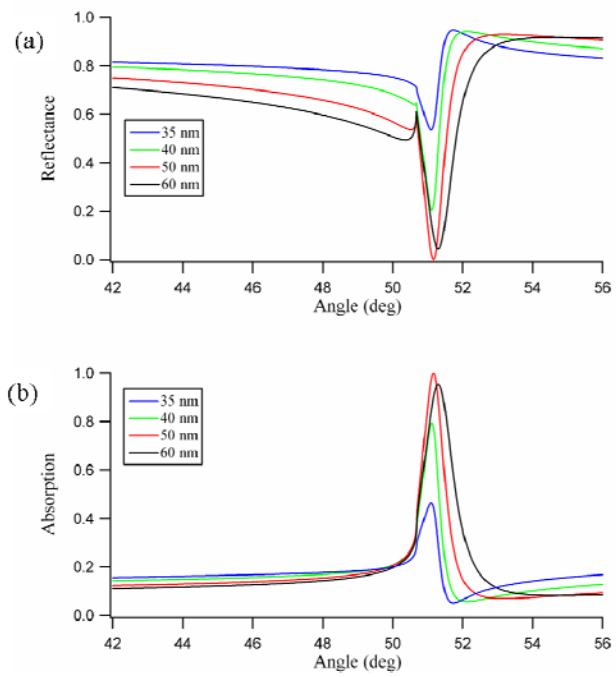

Figure 2.5 Reflectance, (a), and absorption, (b), spectrums for different thickness

Figure 2.6 shows the amplitudes of the electric fields (Ex and Ez), the magnetic field (Hy), as well as the electromagnetic energy density. The light is incident upon the subwavelength grating from the high index prism at the SPR angle of 51.2°. The parameters of the subwavelength grating are $f = 0.2$, $t = 50$ nm and $\Lambda = 200$ nm. The electric field is strong in the slits of the subwavelength grating and strongest near the edges of the slits. This is because the SPPs energy is highly localized near the edges of the slits.

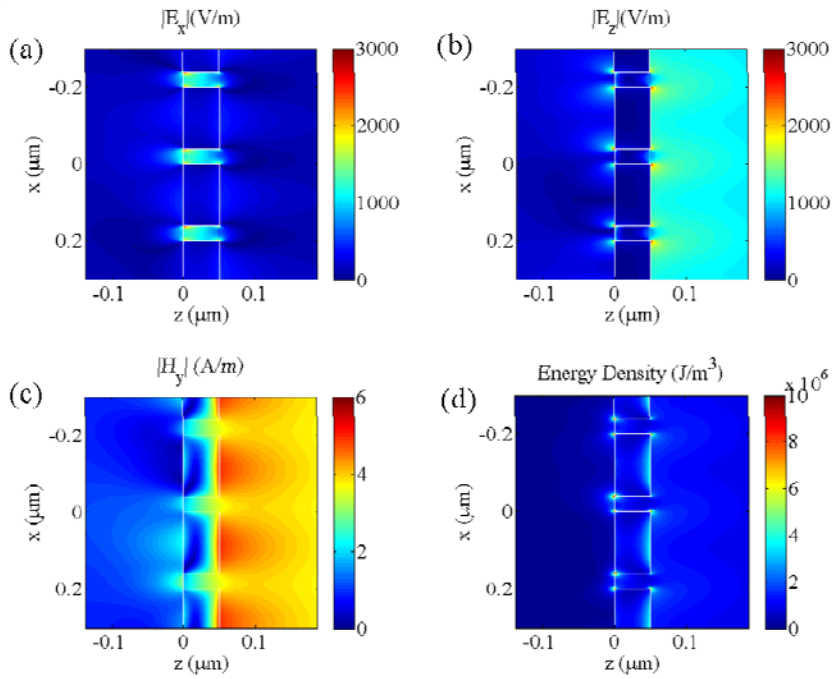

Figure 2.6 (a) The amplitude of the tangential component (x-axis) of the electric field, (b) the amplitude of the normal component (z-axis) of the electric field, (c) the amplitude of the magnetic field, and (d) the energy density distribution. Light is incident from the left and the angle of incidence is 51.2° at resonance.

Here, it was shown that by varying the geometrical parameters of the subwavelength grating, the overall characteristic of the SPPs can be changed as well. At a specific parameter, where $f = 0.2$, $t = 50$ nm and $\Lambda = 200$ nm, the SPR has a better FWHM then the SPR from a uniform thin film, meaning that there is less backscattered radiation. But because the momentum needed to excite the SPPs in subwavelength grating is less than the momentum required to excite the SPPs in the uniform thin film, the SPPs in the subwavelength grating is less confined. To reiterate, this is because the localization of free electrons in the subwavelength grating has increased the intrinsic free electron oscillation frequency. The increase in intrinsic oscillation frequency reduces the SPP confinement to the surface. To demonstrate this, one can include the intrinsic

oscillation frequency from the Drude model in the SPPs mode and expand the equation about the fundamental $k_{0,x}$. The following is the Drude model equation:

$$\varepsilon_m = 1 - \left(\frac{\omega_p}{\omega} \right)^2 \tag{2.6}$$

where ω_p is the plasma frequency or the intrinsic oscillation frequency and letting the the SP wavevector be as follows:

$$\beta = \frac{\omega}{c} \sqrt{\frac{\varepsilon_d \varepsilon_m}{\varepsilon_d + \varepsilon_m}} = k_0 n_{eff} \tag{2.7}$$

The SP wavevector can be expanded about $k_{0,x}$:

$$\beta = k_0 n_{eff}^0 + \frac{k_0}{2 n_{eff}^0} \frac{\partial}{\partial \omega_p} \left(\frac{\varepsilon_d \left(1 - \left(\frac{\omega_p}{\omega} \right)^2 \right)}{\varepsilon_d + 1 - \left(\frac{\omega_p}{\omega} \right)^2} \right) \left(\omega_p - \omega_p^0 \right) \tag{2.8}$$

The final result is

$$\beta - \beta^0 = \frac{-k_0}{n_{eff}^0} \frac{\omega_p^0 \omega^2 \varepsilon_d^2 \left(\omega_p - \omega_p^0 \right)}{\left(\omega^2 \varepsilon_d + \omega^2 - \omega_p^0 \right)^2}. \tag{2.9}$$

Equation (2.9) can be rewritten as

$$\beta - \beta^0 = -\kappa \left(\omega_p - \omega_p^0 \right). \tag{2.10}$$

Equation (2.10) shows that when the surface plasmon wave vector decreases, the intrinsic oscillation frequency or the plasma frequency increases.

In this Chapter, the behavior of the SPR in an array of metal nanostructures, specifically the rectangular subwavelength grating is investigated. By changing the geometrical parameters of the periodic grating, the collective resonances due to the field interactions from neighboring slits can change the overall behavior of the array of

nanoslits. In the following chapter, the SPR from a super-periodic nanoslit array is investigated where there are two periods that affect the behavior and the characteristics of the SPR on the metal film.

CHAPTER 3

SURFACE PLASMON RESONANCE IN 1-D SUPER-PERIODIC METALLIC NANOSTRUCTURES

In the previous chapters, the theory and the background of the SPR have been discussed. Also, the characteristics of SPR observed in both the reflected and transmitted spectrum of light from a periodic metal nanostructure was shown. It was shown that not only does the periodicity provide an additional momentum in exciting SPPs on a metal film, but it also perturbs the properties of the SPPs when the variations in the metal film is smaller than the wavelength. In this chapter, the concept of the super-periodic metallic nanostructure is explained and investigated. Numerical methods are used to give a systematic analysis of the SPR arising from two nanostructures in the super-periodic pattern, the nanoslit and nanohole arrays. The experimental setup and the results used to characterize the nanostructures are also discussed in this chapter.

3.1 Numerical method

The numerical method used to analyze the optical characteristics of the structure is the RCWA and the commercially available software, Lumerical that employs the

finite-difference time-domain (FDTD) method [50]. The FMM method is suitable due to the periodic nature of the nanostructure and has been confirmed with experiments [45-48]. The method expands the fields and the effective permittivity into a Fourier series with an infinite (ideally) number of modes. Since, infinite number modes are not possible, the number of modes is truncated such that the number of modes retained in the calculation provides a converged solution. The higher the amount of modes the more accurate the solution, but that requires a much longer computation time. In the RCWA, the regions of interest are divided into the external and the grating regions. The grating region can comprise of a single or various homogeneous and modulated layers. In order to calculate the amplitudes of the reflected and transmitted fields, the tangential components of the electric and magnetic fields are matched at the boundaries of each layer, resulting in a system of equations. This system of equations is then solved for the reflectance and transmittance coefficients. Numerical inaccuracy can arise if the system of equations become too large, hence enhanced transmittance techniques are used to reduce numerical inaccuracies [42].

3.2 Transmission from periodic subwavelength slits

To lay the groundwork for the super-periodic nanoslit arrays, an understanding of how the SPR behaves in periodic nanoslits is addressed. It was known that by corrugating the metal film, SPPs can be excited by the grating momentum. There were works done in investigating the reflection metallic gratings where they were usually tied to the study of SPPs and localized electromagnetic modes of the grooves [22, 51-55]. However, since the discovery of the extraordinary optical transmission (EOT), there has been a renewed interest in investigating the transmission characteristics of nanoslit arrays [32, 56-67] and

it was shown that the optical transmission peak relates to the excitation of SPPs and the localized modes within the slits. Here, the mechanism behind the SPR mediated optical transmission peak in periodic nanoslit arrays is illustrated in Figure 3.1 [68]. When light is incident onto the slits, the amplitude component is diffracted into the SPPs mode at slit 1 with efficiency β. This SPPs mode will propagate along the surface of the metal until it reaches slit 2. At slit 2, the SPPs then reconverts back to propagating mode within the slit with an efficiency β' and interferes with the incident field. The phase collected by the SPPs at slit 2 is then $e^{ik_{spp}p}$, where k_{spp} is the wave-vector of the SPPs mode. A similar process takes place when the roles of slit 1 and 2 are switched. The superposition of the fields, $H_0 + \beta\beta' H_0 e^{ik_{spp}p}$, at the entrance side of both slits is then transmitted to the exited side with an overall efficiency of *T*. Likewise, a similar process takes place at the exited side and the total amplitude at the output aperture of each slit is then expressed in the following form

$$H = H_0 T\left(1 + \beta\beta' e^{ik_{spp}p}\right)^2. \tag{3.1}$$

The interference process gives a transmission intensity normalized to the intensity of a single $(H_0T)^2$ is of the form

$$\eta = \left\{1 + \left|\beta\beta'\right|^2 + 2\left|\beta\beta'\right|\cos\left[k_{spp}p + \arg\left(\beta\beta'\right)\right]\right\}. \tag{3.2}$$

For multiple slits, the transmission intensity takes the form

$$\eta = \left\{1 + \left|\beta\beta'\right|^2 - 2\left|\beta\beta'\right|\cos\left[k_{spp}p + \arg\left(\beta\beta'\right)\right]\right\}^{-2}. \tag{3.3}$$

The expression for the multiple slits resembles the expression obtained for a Fabry-Perot cavity containing propagating modes. Here, the 'mirrors' are the slits, and the propagating modes are the SPPs modes. There are various explanations as to how the

optical transmission relates to the SPR. However, there are some works that have resembled the mechanism presented here in this dissertation [58, 59, 67, 69].

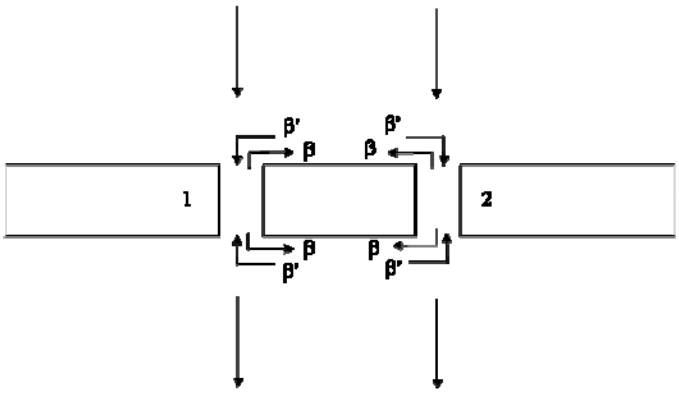

Figure 3.1 Diagram illustrating the mechanism behind the transmission resonance in the subwavelength metallic nanoslits

Using the FMM technique, the optical transmission of a periodic nanoslit is calculated. The period is 420 nm, the slit width is 140 nm and the thickness of the nanoslit array is 60 nm. The material of the nanoslit array is gold. The Lorentz-Drude model is used to obtain the electric permittivity of gold [24]. Light is incident from the glass substrate, with refractive index n= 1.45, and is exited into air. The polarization of the incident light is transverse magnetic (TM), perpendicular to the long axis of the nanoslit. The result is plotted in Figure 3.2, and a resonance peak is seen at the wavelength of 609 nm, above the wavelength where the grating period occurs. The 0^{th} order transmission here depicts a trend similar to that seen in another work [67]. Also, note that there is diffraction at the resonance wavelength, for it is much larger than the grating period. Another characteristic of the SPPs is displayed in Figure 3.3. The results are plotted with different grating periods 420 nm and 480 nm. The fill factor, the ratio of the slit width to the grating period, and the thickness are kept constant. It is easily seen

that when the grating period increases, the resonance peak shifts to the wavelength 696 nm. This is consistent with the SPPs characteristics for a periodic structure where the SPPs wave-vector equals to the incident transverse wave-vector and the addition of the grating orders.

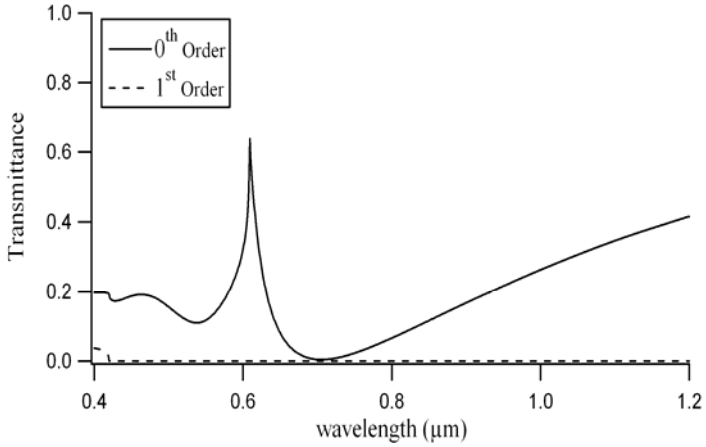

Figure 3.2 Transmission spectra of the gold nanoslit arrays. The slit width is 140 nm, the grating period is 420 nm and the thickness is 60 nm. The solid and dashed lines represent the 0^{th} and 1^{st} orders respectively.

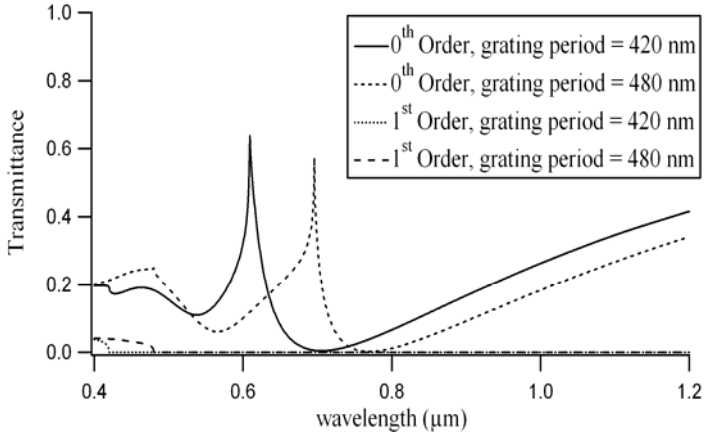

Figure 3.3 Transmission spectra of the gold nanoslit arrays with varying grating period.

3.3 Super-periodic metal nanoslit arrays

In section 3.2, there are two main SPR behaviors for nanoslit arrays. They are that the SPR occurs at the wavelength approximately 1.2 to 1.5 times the grating period and that the resonance wavelength placement is sensitive to the grating period and not to the slit width and thickness. In this section, the SPR in the super-periodic nanoslit arrays is investigated. The super-periodic structure is a 1-D gold rectangular grating that has two periods of different lengths. The first period is defined as the sub-period, Λ, and the second period is a larger period defined as the super-period, Λ_s, of which its length is the multiple integer of the sub-period's length. After every certain number of slits with period, Λ, there is a defect created where there is simply a patch of metal of which its width equals the period, Λ. The distance from one defect to the next is the super-period, Λ_s, as illustrated in Figure 3.4. The thickness of the gold grating film is 60 nm and is placed on a glass substrate of refractive index 1.45. Light is incident upon the grating from the substrate and is transmitted into air. Using the RCWA method, the zeroth order transmission and the first order diffraction as functions of the incidence wavelength were calculated.

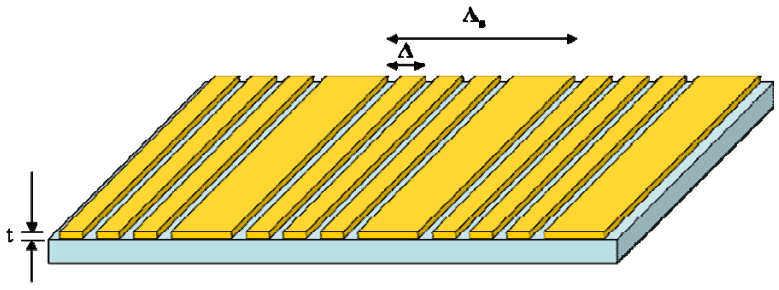

Figure 3.4 Schematic diagram of the super-periodic metal nanoslit arrays.

The light is polarized perpendicular to the grating lines and is normally incident on the super-periodic gold nanoslit arrays. As was previously stated, the electrical permittivity of the gold film is obtained from the Lorentz-Drude model. The calculations were run at a total number of 170 Fourier modes after a series of convergence test. First, the zeroth order transmission and the first order diffraction of the super-periodic device were calculated with different small nanoslit periods. The slit width was kept at 140 nm. The number of nanoslits per super-period is four and the spectral resolution is 1.0 nm. Figure 3.5(a) shows the zeroth order transmission spectra for the devices with three different nanoslit periods, 390 nm, 420 nm and 450 nm. Figure 3.5(b) shows the first order diffraction efficiencies from the three devices. For the super-periodic nanoslit with small period 390 nm, the zeroth order transmission peak is at 575 nm. The first order diffraction peak is at 566 nm, which is slightly smaller than the zeroth order transmission peak wavelength. For the device with period 420 nm, the zeroth order transmission peak occurs at 612 nm. For the device with period 450 nm, the zeroth order transmission peak is at 653 nm and the first order diffraction peak is at 653 nm. It can be seen that the surface plasmon resonance shifts to a longer wavelength as the small period increases. This shift is also observed in the first order diffraction but at different resonance wavelengths. To compare with the surface plasmon resonance in regular metal nanoslit arrays, the zeroth order transmission of the regular nanoslits is calculated with periods of 390 nm, 420 nm and 450 nm, as shown in Figure 3.5(c). The gold film thickness is 60 nm. The resonance wavelength observed for the regular nanoslits is similar to that observed in the first order diffraction for the super-periodic nanoslit arrays. In addition to the fundamental surface plasmon resonance mode, there are additional modes excited by

the super-periodic nanoslit arrays. For the super-periodic nanoslit arrays with 420 nm small period and 2100 nm super-period, the fundamental plasmonic resonance mode is found at 609 nm. And there is another additional surface plasmon resonance at 672 nm, which manifests itself as a small peak observed in the zeroth order transmission. This surface plasmon mode is observed much clearer in the first order diffraction.

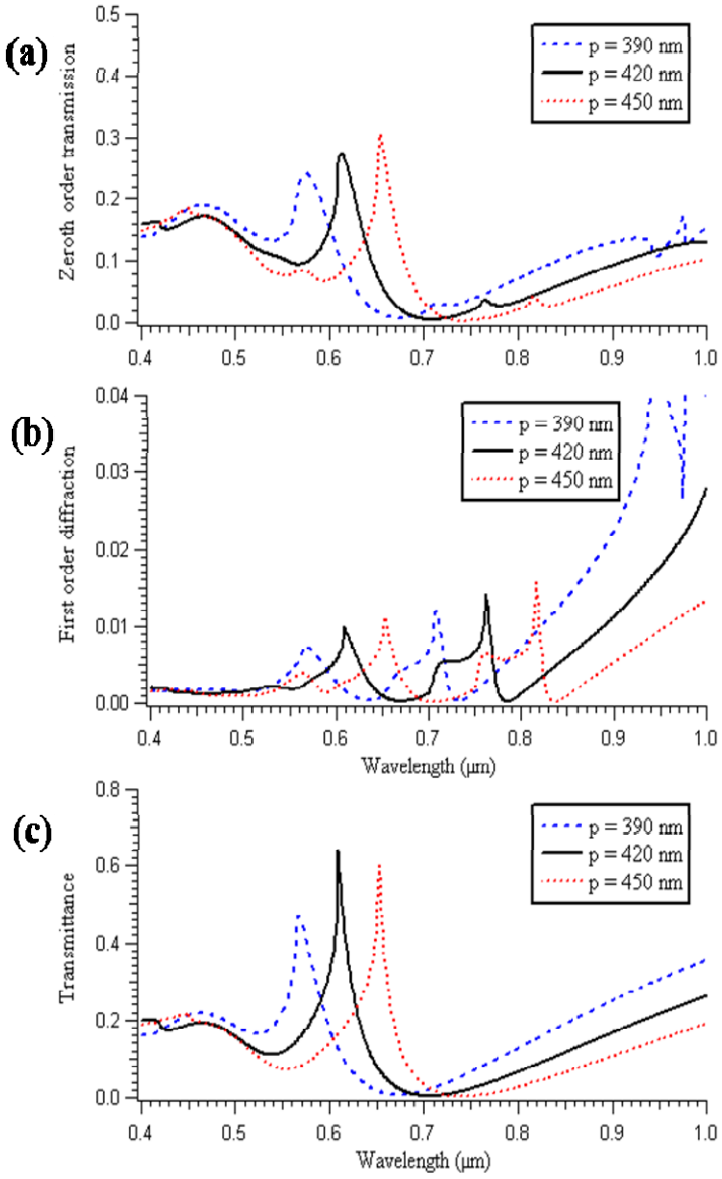

Figure 3.5 (a) 0^{th} order transmission spectra of the non super-periodic nanoslit array (*solid*) and the super-periodic nanoslit arrays (*dotted*), (b) 0^{th} (*solid*) and (c) 1^{st} (*dashed*) order transmission spectra of the super-periodic nanoslit arrays.

To better understand the behavior of modes at wavelengths 609 nm and 672 nm, the electric field distribution at the surface of the nanoslit array is calculated. Figures 3.6(a) and (b) show the Ex and Ez components of the electric field distribution in the device at 609 nm in the log scale, respectively. Figures 3.6(c) and (d) show the Ex and Ez

components of the electric field distribution of the device at 612 nm in the log scale, respectively. It is seen clearly, that the electric field in the device is stronger at 609 nm than at 612 nm. This indicates that the resonance observed in the first order diffraction reveals more accurately the surface plasmon resonance occurring in the super-period metal nanoslit arrays. Each of the nanoslits in the array can be thought of as an optical antenna that radiates when excited. In Figure 3.6(a), the x-component of the electric field distribution focuses at a distance 1.2 μm above the nanoslits. This is due to the interference of the nanoslits and the surface plasmon resonance in the nanoslits enhances that radiation.

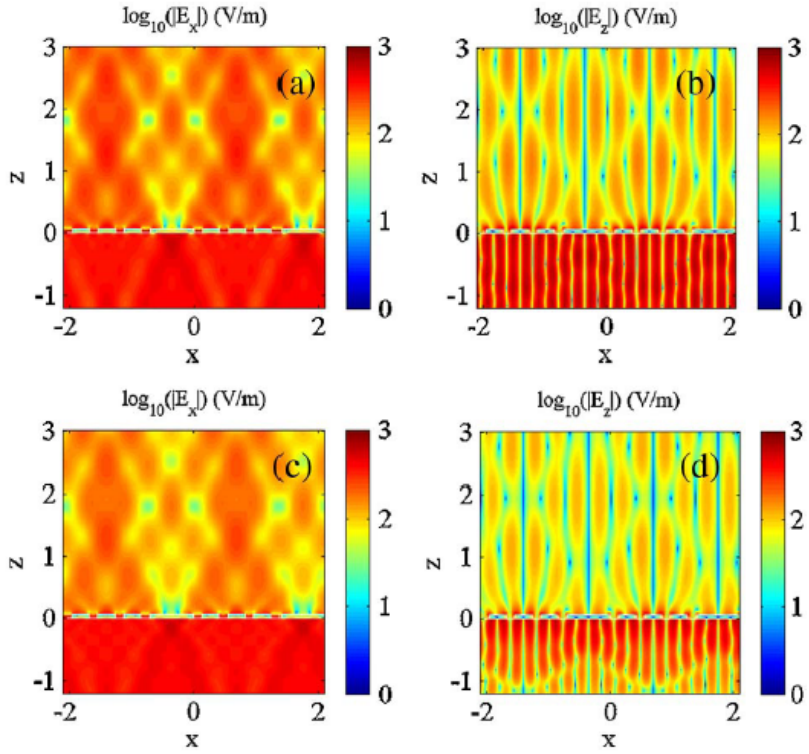

Figure 3.6 Electric field distributions in the super-periodic metal nanoslit arrays in the log scale (a) Ex component of the electric field at the peak first order diffraction wavelength of 609 nm; (b) Ez component of the electric field at the peak first order diffraction wavelength of 609 nm; (c) Ex component of the electric field at the zeroth order peak transmission wavelength of 612 nm; and (d) Ez component of the electric field at the 612 nm wavelength.

Figures 3.7(a) and (b) show the x- and z- components of the electric field distributions for the first order diffraction peak at 764 nm, respectively. It can be seen that the electric field at the first order diffraction peak wavelength is stronger than the electric field at the zeroth order transmission peak wavelength. This means that the first order diffraction reveals the surface plasmon resonance in the nanostructure more accurately than the zeroth order transmission does.

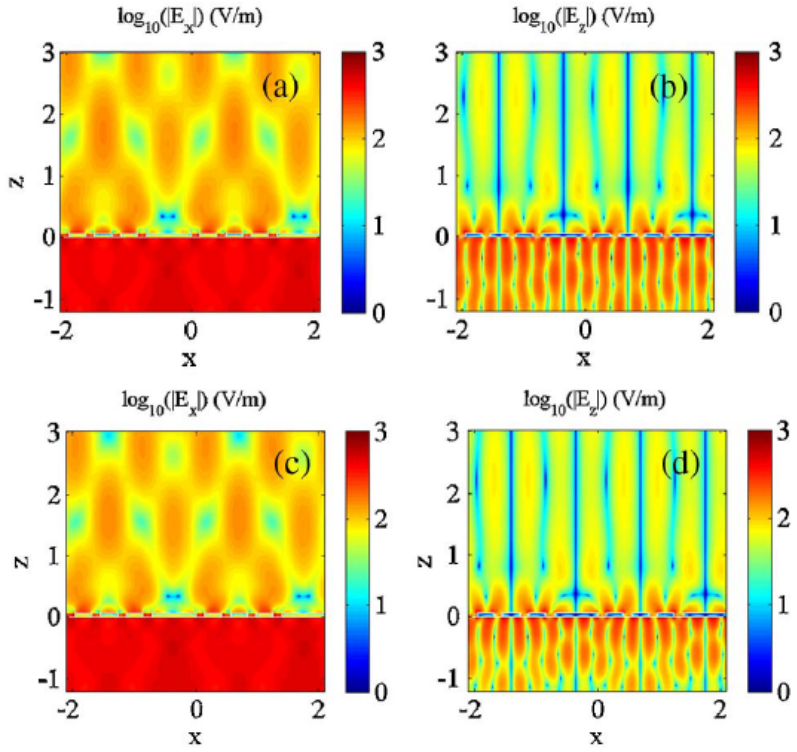

Figure 3.7 Electric field distributions in the super-periodic metal nanoslit arrays in the log scale (a) Ex component of the electric field at the peak first order diffraction wavelength of 762 nm; (b) Ez component of the electric field at the peak first order diffraction wavelength of 762 nm; (c) Ex component of the electric field at the zeroth order peak transmission wavelength of 764 nm; and (d) Ez component of the electric field at the 764 nm wavelength.

How the surface plasmon resonance modes change when varying the slit width is investigated next. The thickness of the gold film and the super-period is kept constant. Figures 3.8(a) and (b) show the zeroth order transmission and first order diffraction respectively, of three different nanoslit widths, 120 nm, 140 nm and 160 nm. Figure 3.8 shows that the change in nanoslit width does not determine position of the resonance wavelength, but it has a significant impact on the linewidth of the resonance; the smaller the slit width, the narrower the linewidth of the resonance.

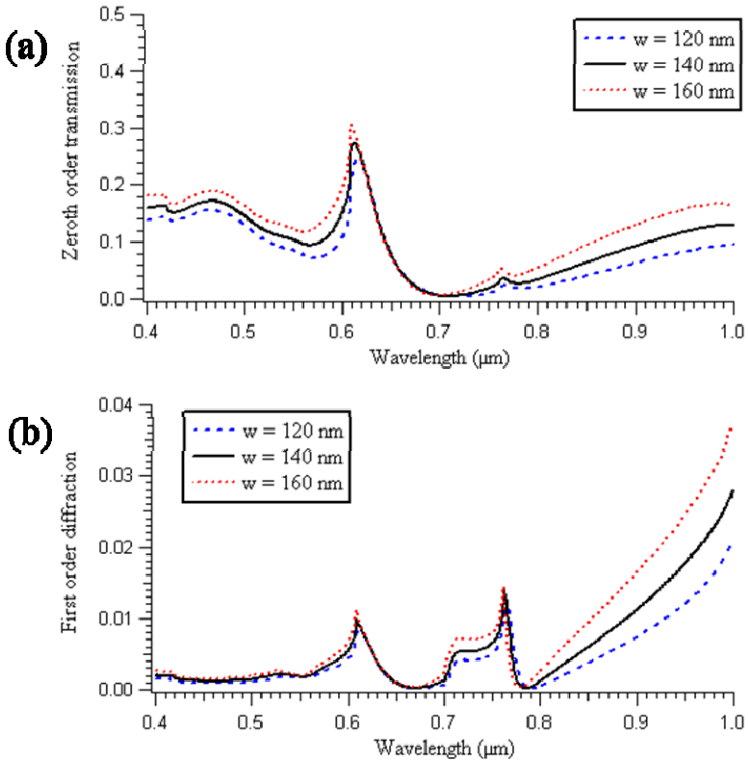

Figure 3.8 (a) The 0th order transmission and (b) the 1st order diffraction from the super-periodic gold nanoslits arrays with different nanoslit widths.

To determine how the number of slits per super-period affects the resonance, the zeroth order transmission and first order diffraction of three different super-period

lengths are calculated. The length of the super-period is determined by the number of slits per super-period while keeping the small period constant. The slit width is 140 nm and the small period is 420 nm. Figure 3.9(a) shows the zeroth order transmission spectra of the super-period nanoslits with increasing super-period. The super-period is 1680 nm, 2100 nm, and 2520 nm, respectively. The zeroth order transmission peaks for all three super-periods occur at 612 nm, although they have different strength in resonances. The first order diffraction peaks occur at 609 nm. From Figure 3.9(a), the resonance wavelength does not change when the number of slits in the super-period changes. The resonance strength in the first order diffraction decreases as the number of nanoslits per the super-period increases, as shown in Figure 3.9(b). This is because less energy resides in the first order diffraction as more diffraction orders appear as the super-period increases. This is consistent with the observation that as the number of slits increases, the more define and stronger the resonance is in the zeroth order transmission [67].

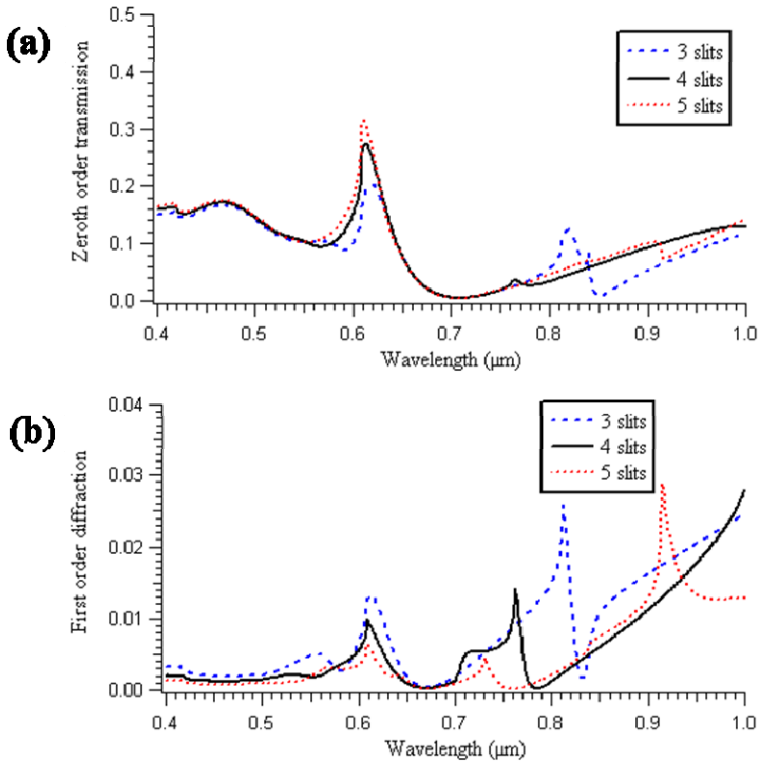

Figure 3.9 (a) 0th order transmission and (b) 1st order diffraction of the super-periodic gold nanoslit arrays with different number of nanoslits in the super-period unit cell.

3.4 Gold super-periodic nanoslit arrays device fabrication

After numerical calculations were completed, the super-periodic nanoslit arrays were fabricated to experimentally characterize the nanoslits. The electron beam lithography (EBL) process, a well-known and standard procedure for fabricating nanostructures is being used here. The EBL is a technique where a beam of electrons transfers energy to a layer, the photoresist that is spread across the surface and is sensitive to electrons. The reaction of the photoresist to the exposure of the electrons depends on the tone of the resist that is either a positive or a negative tone. If the photoresist is positive, the exposed portion of the photoresist to the beam of electrons becomes soluble in the photoresist developer where the unexposed portions of the photoresist remain

insoluble. For a negative tone, the dynamics are the exact opposite. The unexposed portions of the resist are soluble in the photoresist developer whereas the exposed ones are not. Once the patterns are made on the photoresist using the EBL technique, the patterns on the photoresist are then transferred unto the substrate via the etching or lift-off method. The EBL technique serves our purpose well as it is capable of making nanostructures with feature sizes of roughly 10 nanometers. However, at such a high resolution, the conditions of the electron gun, the environment and the sample play important roles in successfully fabricating the structure.

The standard procedure in the EBL technique comprises of three main stages: photoresist film deposition, exposure and developing. The parameters in all three stages are crucial in determining the outcome of the process. For fabricating nanoapertures of different geometrical shapes, the process does not change except during the exposure stage. First, a 2 nm-thick chromium (Cr) film was deposited on a quartz substrate (Pyrex 7070) via the sputtering deposition method. This film acts as an adhesion layer between the quartz substrate and the gold film. This was then followed by the deposition of the gold film with the desired thickness via the same sputtering deposition method. Next, the positive electron beam resist (ZEP 520A) was spin-coated on top of the gold film at 4500 revolutions per minute (RPM) to give a uniform thickness of approximately 150 nm. The samples were then baked on a hot plate at 90°C for 3 minutes to harden the photoresist. The electron beam exposure was performed using the LEO 1550 scanning electron microscope (SEM) and lithography system and selected areas of the samples were subjected to the electron beam irradiation at an acceleration voltage of 30 kV. The aperture size of the electron gun was set to 10 μm and the measured beam current was

approximately 18 pA. The size of the nano-aperture patterns on the photoresist are determined by the amount of dose they get. Here, the dosage used is defined as the area dose, where

$$\textbf{Area Dose} = \frac{(\textbf{Beam Current}) \times (\textbf{Exposure Time})}{(\textbf{Center - to - Center}) \times (\textbf{Line Spacing})}. \qquad (3.1)$$

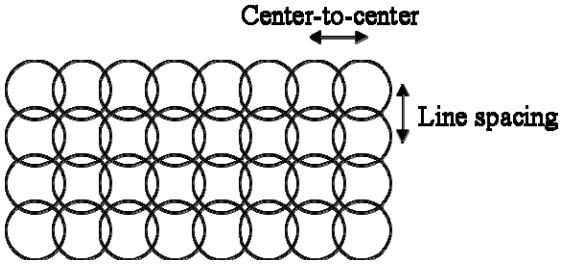

Figure 3.10 Diagram illustrating the 'center-to-center' and 'line spacing' distances between adjacent beam spots.

The amount of 'area dose' used varies with the different nanostructures but is within the range of 70 – 200 $\mu C/cm^2$. For EBL, the proximity effect occurring from the forward and backward scattering of electrons is an important consideration when determining the exact shape and resolution of the patterns. Corrections for the proximity effect can be done by manipulating the amount of area dose and the shape design in the virtual mask as is shown in Figure 3.11. The proximity effect can be seen prominently for the bowtie structure.

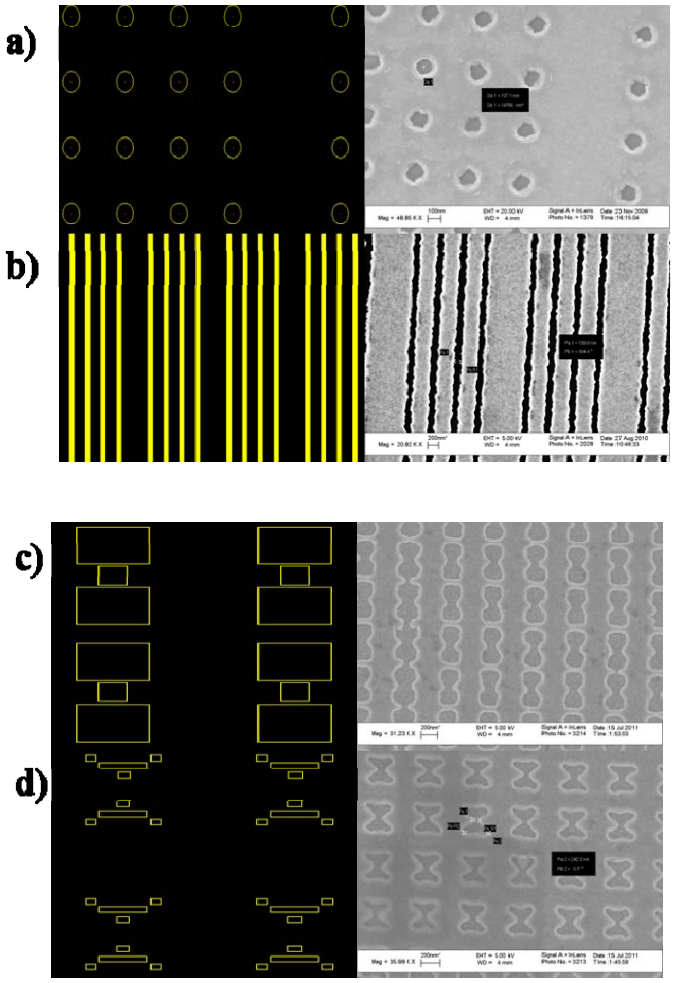

Figure 3.11 This figure shows the corresponding design (*left*) and the actual result (*right*) for (a) circular holes, (b) slits, (c) I-shape, and (d) bowtie.

Once the sample has been exposed to the electron beam irradiation, the sample is then developed in developing solution for ZEP 520A, the ZED-N50, for 1.5 minutes. The ZED-N50 removes the area of the photoresist that has been exposed to the electron beam irradiation, forming a nanostructure pattern on the photoresist. After immersing the sample in developer ZED-N50, the sample was then rinsed with isopropyl alcohol and de-ionized (DI) water, and blow-dried with Nitrogen. The sample was then oven baked at 120°C for 2 minutes to dehydrate the sample. To transfer the pattern from the photoresist

to the gold film, the ion milling method was employed. In short, the ion milling method uses ions to collide with the ions of the subjected film at a velocity that is driven by the potential difference between two electrodes in the reactive ion (RIE) chamber. The ions that are bombarded out of the film are then flowed out of the chamber to prevent recombination at the surface of the film. In this case, Argon ions were used because they are inert. The etch rate for gold is approximately 7.5 nm per minute at the platen power of 200 Watts and the Argon gas flow rate of 20 sccm. After the gold film is etched all the way through, the remaining photoresist is removed by immersing the sample in the ZEDMAC solution for about an hour. The sample is then rinsed with DI water, blow-dried with the nitrogen gas and baked in the oven at 120°C for 2 minutes to dehydrate the sample.

3.5 Experimental setup

An apparatus was set up to characterize the zeroth order transmission and the first order diffraction of the fabricated super-periodic nanoslit arrays. Because the first order diffraction of each wavelength disperses at a different angle of diffraction, a linear charge-coupled device (CCD) array was used to capture the first order diffraction efficiency. A spectrometer is used to obtain the zeroth order transmission of the super-periodic nanoslits. The optical setup for characterizing the super-periodic device is illustrated in Figure 3.12 and the actual setup is shown in Figures 3.13 and 3.14. In order to have a correct characterization of the super-periodic nanoslits, the incident light has to be polarized in either the transverse electric (TE) or transverse magnetic (TM) state and has to be from a broadband source. To achieve a good signal-to-noise (SNR) ratio, the light has to focus to a spot size of approximately 300 x 300 μm^2, the total area of the

super-periodic nanoslit arrays, so that the light passing through the area outside of the nanoslits does not muddle the transmission characteristics of the nanoslits. The broadband light source used in this experiment is a super continuum broadband laser (SuperK from NKT photonics), which emits low repetition rate (21 kHz) broadband coherent light with a relatively flat spectrum from 500 nm to 2400 nm wavelength. It is required that the spot size of the beam that emits from the source be roughly the size of the patterned area so as to prevent the background noise from muddling the transmission characteristics of the super-periodic nanoslit arrays, as was stated earlier. To achieve this, an objective lens (20X) was use to collimate the beam. This was done by adjusting the distance between the facet of the fiber source and the objective lens. The distance is roughly the length of the focal length of the objective lens.

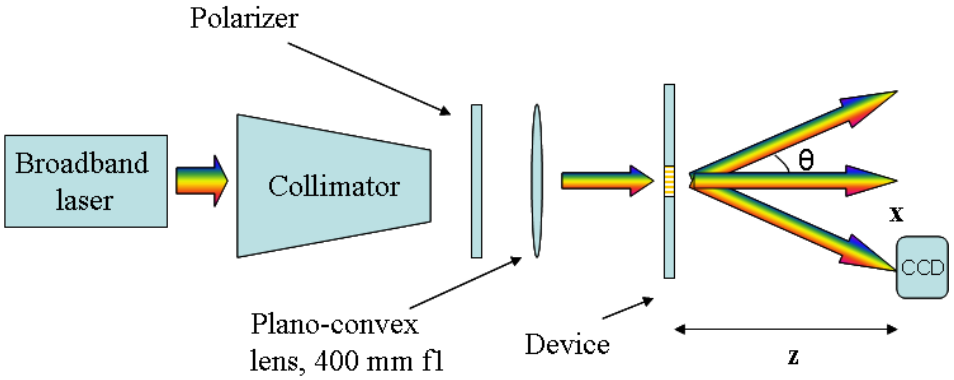

Figure 3.12 The optical setup for characterizing the super-periodic nanostructure device. The CCD sensor array captures the angular dispersion of one first order diffraction which carries the surface plasmon resonances.

Figure 3.13 The optical setup for characterizing the super-periodic nanostructure device. The experiment system is placed on an optical bench.

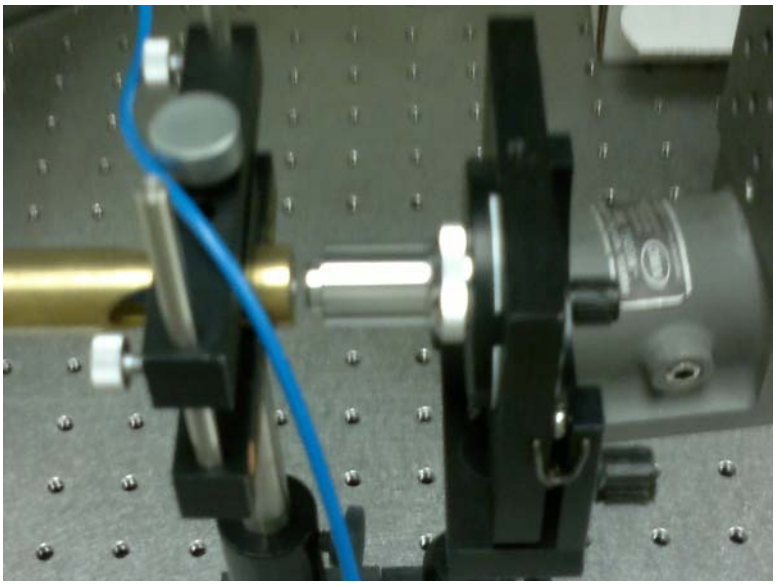

Figure 3.14 The end facet of the photonic crystal fiber from the broadband source and objective lens.

The collimated beam is then passed through a convex lens of focal length 400 mm shown in Figure 3.15, to focus the beam size to within 300 x 300 μm^2. The half beam spot size can be estimated using the equation for a Gaussian beam

$$w_0 = \frac{4}{\pi}\lambda\frac{f}{D}, \tag{3.2}$$

where λ is the central wavelength of the spectrum emitted from the source, f is the focal length of the convex lens and D is the width of the beam measured at the lens. Letting λ be 700 nm, the central wavelength of the spectrum between 400 nm and 1000 nm, and D being 3 mm, the half beam spot size is approximately 119 μm, where the full beam spot size is 238 μm at the focal point of the lens. Hence, the total area of the device illuminated by the broadband source covers roughly the rectangular area 238 x 238 μm^2, well within the area of the patterned portion of the device. A polarizer here was placed before the convex lens to control the polarization state of the light between TE and TM polarization states. A shutter was then placed near the device to remove the unwanted background noises from the reflections and shadows from the optical components in the system as shown in Figure 3.16. Because the output of the super continuum laser was greater than 100mW, neutral density filters are placed within the system to reduce the output power of the laser. Alignment of the optical system was done by tracking the reflection of the source back to the facet of the fiber laser. Once the system was aligned the device was situated at the focal point of the lens, where the beam size is at its tightest.

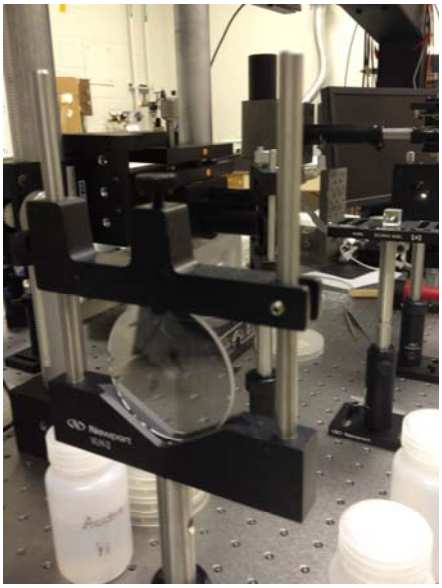

Figure 3.15 Convex lens to focus the beam to a spot size roughly the size of the patterned area.

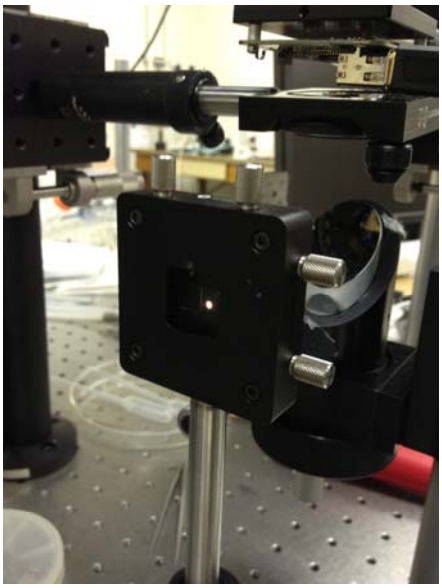

Figure 3.16 The shutter in the experiment system was used to prevent unwanted background noise in the system from entering the CCD.

In order for the liquid to sustain atop of the device for a longer period of time, the device was placed such that the device is perpendicular to the floor. A mirror was used to reflect the incident light to the device as shown in Figure 3.17. To ensure total

illumination of the source on the patterned area, a spectrometer was used to measure the transmission across the device. By adjusting the bearings on the optical component that holds the device to obtain maximum transmission across the device, this means that the entire beam is within the patterned area. Lastly, a charged-couple device (CCD) imager (Unibrain, Inc.) was used to capture the angularly dispersed distribution of the first order diffractions. The CCD imager was a black-white photo-detector array of 640 by 480 square pixels manufactured by Sony (SONY ICX098BL), also shown in Figure 3.17. The pitch of the pixels on the CCD is 5.6 μm in two dimensions and each physical pixel on the CCD corresponds to one pixel on the captured image.

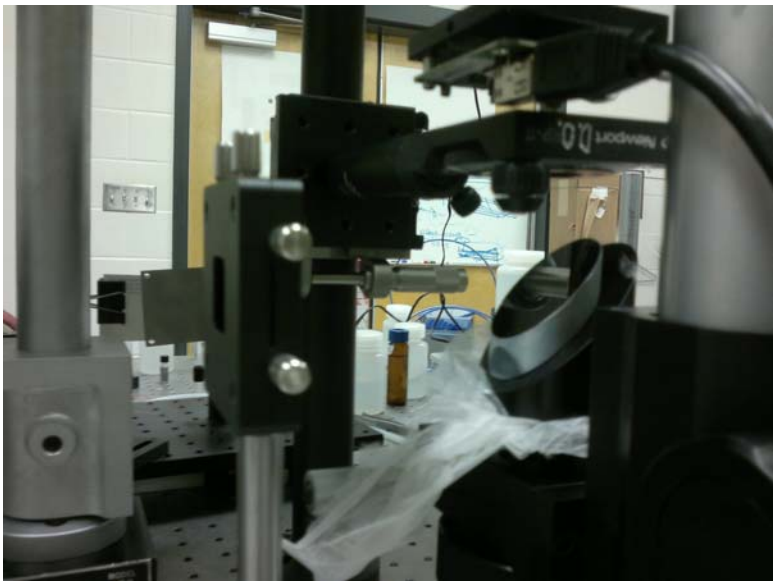

Figure 3.17 The mirror is used to reflect the incident light onto the device.

Obtaining the zeroth order transmission spectrum of the device is simple, as one has to simply collect the transmitted light that does not diffract using a spectrometer. However, finding the first order diffraction requires additional steps. First, it is important to note that light is normally incident on the device, and there is a slight deviation

between the surface normal and the incidence angle. This deviation can be corrected later in the data analysis. The surface of the super-periodic nanoslit arrays and the CCD were normal to the direction of the incident light. The distance between the device and the CCD array was z. The CCD camera was placed on a translation stage that can be moved along the direction of diffraction. By moving the CCD, the one first diffraction spot can be moved on the CCD. A variable neutral density filter was used to ensure that the intensity of the broadband laser light does not saturate the CCD. To find the correspondence between the wavelength and the pixel on the CCD, a calibration is needed. The position of the first order diffraction on the CCD chip in term of the "x" can be obtained for the specific wavelength from

$$x = z\tan(\theta) = z\tan\left[ArcSin\left(\frac{\lambda}{\Lambda s}\right)\right] \tag{3.3}$$

where x is the distance between the zero-order position and the first order diffraction position on the CCD, z is the distance between the CCD and the device under test. To determine the wavelength from the pixel number on the CCD, the Equation (3.3) can also be written as

$$\lambda = \frac{\Lambda_S x}{\sqrt{x^2 + z^2}}. \tag{3.4}$$

On the CCD, the position x is the pixel number multiplied by the size of the CCD pixels. In order to find the correspondence between the wavelength and the "x" position on the CCD, a HeNe laser of 632.8 nm wavelength was used to replace the broadband light source to do the calibration. A beam splitter was used to allow the HeNe laser to enter the optical system without removing the broadband source. First, we ensured that the surfaces of the CCD imager and the device were parallel. Then, we adjusted the position

of the CCD so that the zero-order transmission of the HeNe laser was at the center of the CCD. Once the position of the zero-order transmission is obtained, the CCD was moved using the translation stage to record the position of the HeNe laser's first order diffraction while keeping the surface orientation. Like the zero-order, the center of the first order diffraction was moved to the center of the CCD. The distance that the CCD moved, gave the value x for the 632.8nm wavelength. The distance (z) between the device and the CCD was calculated using the Equation (3.4). In our experiment, the distance between the device and the CCD was found to be 14.59mm. With the HeNe laser's first order diffraction position as the reference point and the CCD pixel pitch (Δx) of 5.6 μm, the correspondence between wavelengths and the pixels of the CCD were uniquely determined. After the calibration, the HeNe laser was turned off and the broadband light source was switched back to conduct the measurement. A beam splitter was used to switch back and forth between the broadband source and the HeNe laser. The procedure described above is illustrated in both Figures 3.18 and 3.19.

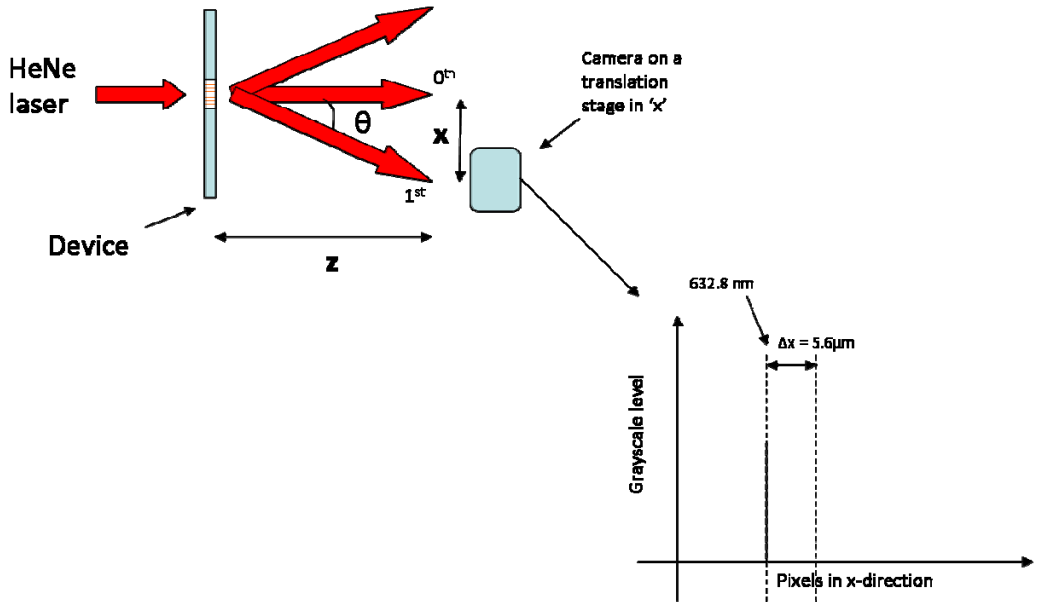

Figure 3.18 This illustrates the determination of the HeNe laser on the CCD sensor array. The information provides the unknown distance, z and x.

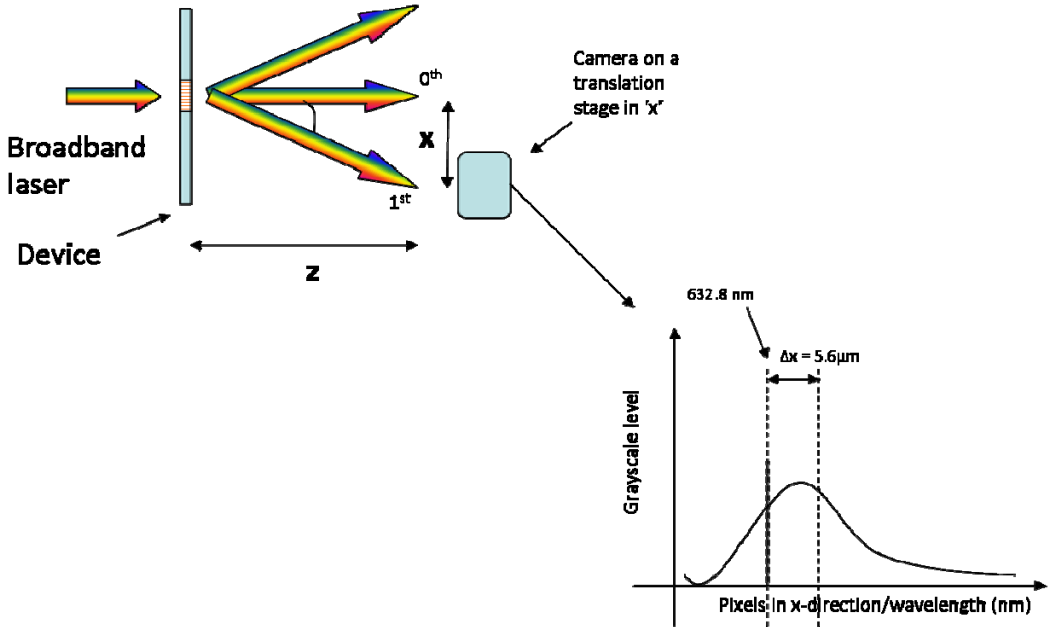

Figure 3.19 Illustration showing the wavelength position on the CCD after calibration with the HeNe laser.

Once both the images of the first order diffraction illuminated using both the HeNe and the broadband source on separate occasions were captured, the images were processed using the MATLAB program. The amount of current generated by the CCD was controlled by adjusting the variable neutral density filter in the experimental system and also by adjusting the gain in the CCD. Here, the gain in the CCD has been set at zero for there are more than enough photons from the broadband source to generate reasonable amounts of current for data analysis. Figure 3.20 shows the diffraction orders scattered from the super-periodic gold nanoslit arrays when illuminated with the broadband laser. Figure 3.21 shows the images captured by the CCD when the nanoslits were illuminated with the HeNe laser, Figure 3.21(a), and the broadband source, Figure 3.21(b). The first order diffraction image of the super-periodic nanoslits when illuminated by the HeNe laser was first captured, and then while maintaining the CCD's position, the first order diffraction image of the super-periodic nanoslits when illuminated by the broadband source was taken. Figure 3.22 shows the intensity level generated by the CCD for the two different images, Figure 3.21(a) and Figure 3.21(b). The slice of each image was taken at the row that has maximum grey intensity level. The images show that they do not have smooth edges at the top of the peaks. This is due to the noise level in the system. However, one can still determine the pixel that corresponds to the peak of the HeNe laser in the image and therefore the pixel of the HeNe laser in the image of the first order diffraction illuminated by the broadband source.

Figure 3.20 The diffraction orders from the super-periodic nanoslit arrays when the device was illuminated at normal incidence.

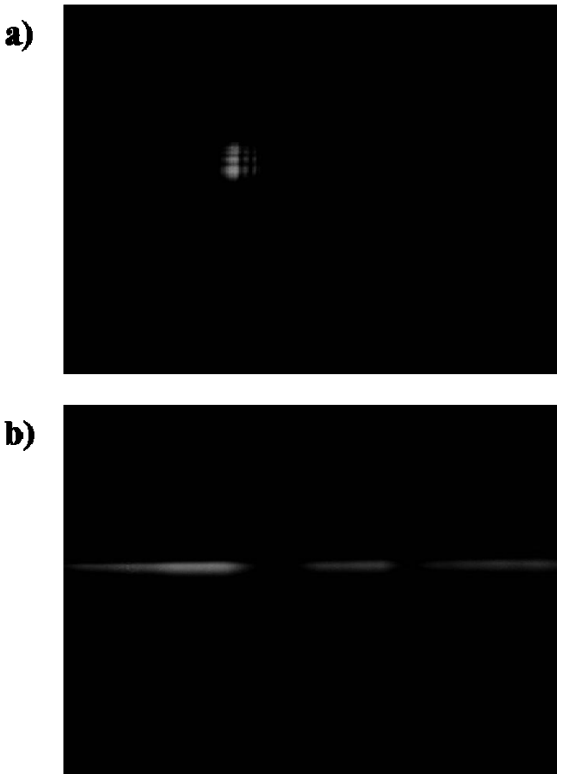

Figure 3.21 (a) The first order diffraction image of the super-periodic nanoslit arrays captured by the CCD when illuminated with the HeNe laser. (b) The first order diffraction image of the super-periodic nanoslit arrays captured by the CCD when illuminated with the broadband source.

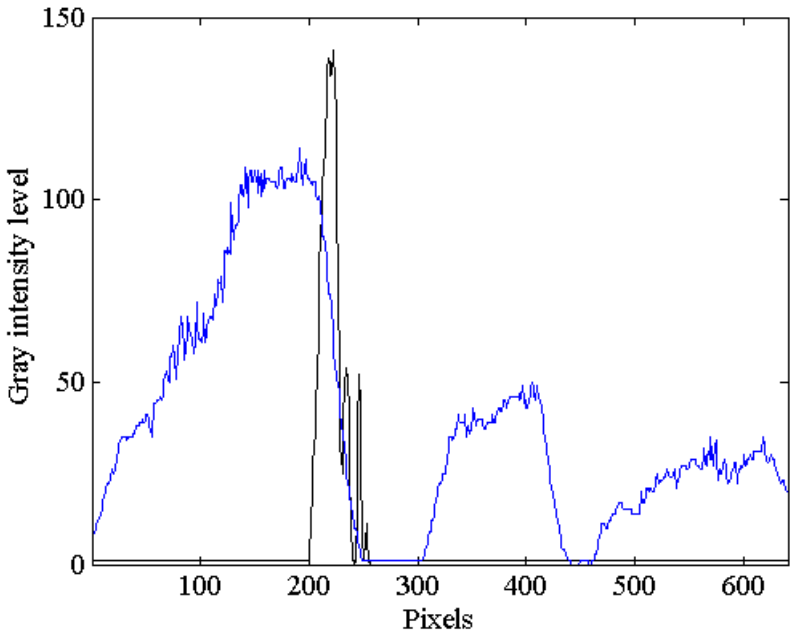

Figure 3.22 The gray intensity level of the CCD when the super-periodic nanoslit arrays were illuminated with HeNe laser (black) and the broadband source (blue).

The next step in processing CCD image of the first order diffraction of the super-periodic nanoslit arrays is to calculate the rest of the spectrum relative to the position of the HeNe wavelength, 632.8 nm. To calculate corresponding wavelengths as illustrated in Figure 3.18 and Figure 3.19, equation (3.4) is used. The next step is to then sum up of the values in all rows in each column to compensate the spread of energy in the vertical direction, parallel to the 'grating' lines. The black areas are around the curve are set to zero, as we expect those to be background noise. Because the range of the responsitivity curve of the CCD provided by the manufacturer is only within 400 nm and 1000 nm, whatever wavelength captured by the CCD that is outside that range is cut off. Figure 3.23 shows the photodetector responsitivity of the CCD obtained from the technical data sheet of the manufacturer.

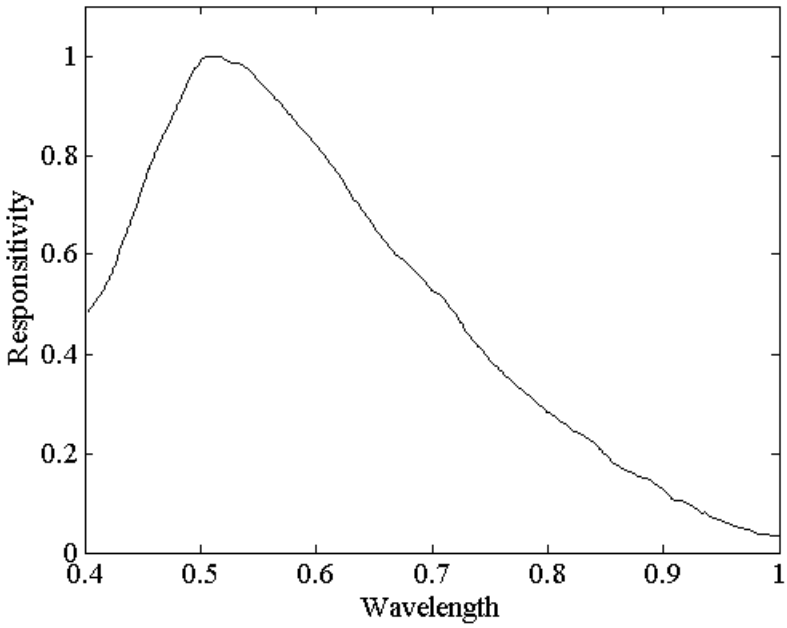

Figure 3.23 The responsitivity of the CCD from 400 to 1000 nm wavelength.

Therefore the signal generated by the first order diffraction of super-periodic nanoslit arrays as a function of wavelength is the summed up values in all rows in each column minus the values of the dark areas in the CCD image, divided by the responsitivity of the CCD. Figure 3.24 shows the signal generated by the first order diffraction efficiency of the super-periodic nanoslits as a function of the wavelength. As it can be seen, there are three peaks that closely resembles the simulation result shown in Figure 3.5(b).

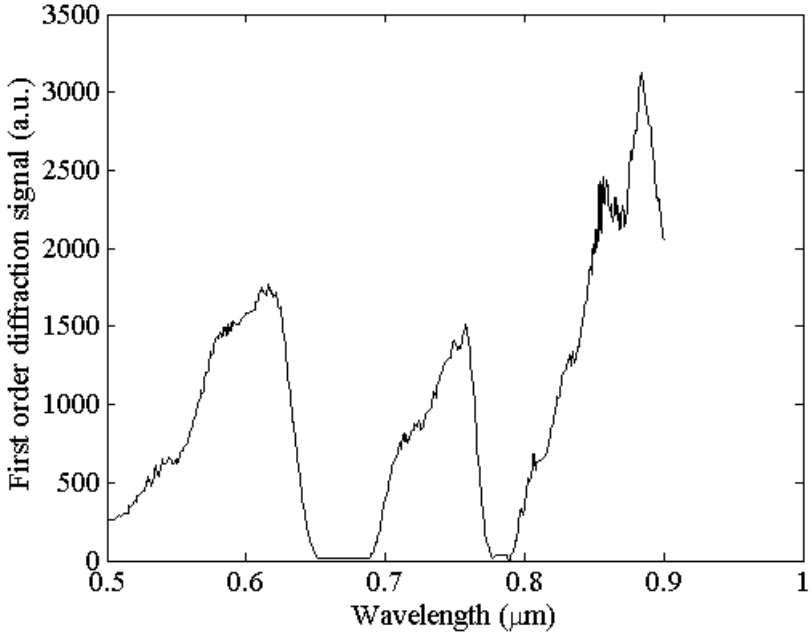

Figure 3.24 The first order diffraction signal of the super-periodic nanoslits as a function of wavelength.

The zeroth order transmission of the super-periodic nanoslit arrays was taken using the commercial spectrometer, Ocean Optics USB 2000. To take the zeroth order spectrum, the CCD was removed from the experimental system and was replaced with the multimode fiber that has the central wavelength at 760 nm that is then connected to the spectrometer. Therefore, the zeroth order transmission and the first order diffraction signal were taken at different times. Although the results were taken at different times, they still remain valid because the conditions of the system do not change with the exception of the constant switch in places between the CCD and the optical fiber that is connected to the spectrometer. Also, gold is an inert element, where it is not reactive and is not prone to change over time.

This section 3.5 describes the experimental system that was used to obtain the zeroth and first order diffraction efficiencies of the super-periodic nanoslit arrays that characterize the surface plasmon resonances of the structure. Because each wavelength diffracts at a unique diffraction angle, a linear CCD array or a CCD in this case was used to obtain the spectrum of the first order diffraction signal. After the first order diffraction efficiency was recorded by the CCD, the data image was processed and calibrated to determine the corresponding signal generated by the first order diffraction with its unique wavelength. Once this procedure was determined, the super-periodic nanoslit were characterized and studied.

3.6 Transmission characteristics of the super-periodic metal nanoslits

After setting up the optical system and determining the procedure for transforming the image into a plot of the first order diffraction signal versus the wavelength, the transmission measurements of the super-periodic nanoslit arrays are taken. Light is normally incident from the quartz substrate through the super-periodic device. For the TE polarization state, the electric field is perpendicular to the super-period grating vector. For the TM polarization, the electric field is parallel to the super-period grating vector. To reiterate, the width of the slit is 140 nm and the thickness of the gold film is 60 nm. The period is 420 nm and the super-period is 2100 nm. The zeroth order transmission of the super-periodic nanoslits was obtained using the spectrometer and the first order diffraction images were obtained using the CCD and the first order diffraction signal was provided using the process described in the previous section. Data was also taken for the super-periodic nanoslits when the surface of the device was

covered with different alcohols to understand the behavior of the SPR with changes in the refractive index at the surface of the device.

With the CCD, we first captured the angular distribution of the first order diffraction versus the wavelength when there was no chemical presence on the device. Then a tiny drop of methanol was applied to the surface of the device using a syringe and once the methanol was spread out evenly to develop a thin layer of methanol, the first order diffraction image was recorded. After the image was recorded, the surface of the device was blow-dried with nitrogen. Before applying the next chemical, a wait time of 10 minutes was given to allow the methanol to completely evaporate from the surface. The next chemical, acetone was then applied to the surface of the device. The method used to apply the methanol was also the same for the application of acetone. Figure 3.25 shows the false color images of first order diffraction from the nanoslits with the different exiting mediums: air, methanol and acetone. The first order diffraction image for the air Figure 3.25(a) shows the distinct bright spots, with the brightest occurring approximately in between pixels 150 and 210. But when methanol is applied, the brightest spot is seen shifted to the left. Another bright spot is seen to have occurred near the 200^{th} pixel. This is the same for the image when acetone is applied. However, the difference between the methanol and acetone images is that the brightest spot seen in the acetone's image is longer than the brightest spot seen in the methanol's image. Also, the bright spot seen near the 200^{th} pixel in the methanol's image appears to have shifted to the right in the acetone's image.

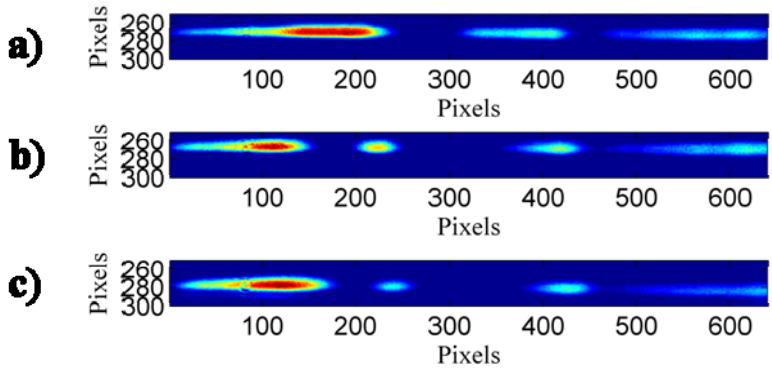

Figure 3.25 False color images captured by the CCD when probed with different solutions (a) no solution, (b) methanol and (c) acetone.

By applying the procedure described in Section 3.5, the first order diffraction signal of the super-periodic nanoslits for all three cases, air, methanol and acetone, were calculated. Figure 3.26 plots the zeroth order transmission and the first order diffraction signal of the super-periodic nanoslits for all three cases. Figure 3.26(a) shows the zeroth-order transmission spectrum from the device in air (solid black line), methanol (dotted blue line) and acetone (dotted red line). The zeroth order transmission was obtained using the commercial spectrometer, Ocean Optics USB 2000. There is only one resonance observed in the zeroth order transmission for all three cases. The resonance peak observed in the zeroth order transmission when no chemical is applied is 615 nm. That resonance peak shifts to 636 nm when methanol is applied and it shifts again to 641 nm when acetone is applied. The strength in resonance decreases with the application of methanol and acetone. This decrease in strength resonance is due to the decrease in coupling strength between the incident light and the SPPs on the surfaces of the gold ridges of the grating, and therefore there is less de-coupling of SPPs into the transmitted light.

Figure 3.26(b) shows the first order diffraction signal spectrum of the super-periodic nanoslits for the three different cases, air (solid black line), methanol (dotted blue line) and acetone (dotted red line). There are three distinct peaks observed for the first diffraction order signal when material at the surface of the device is simply air. However, when the alcohols were applied, there are four peaks seen in the spectrum. The first resonance at the wavelength 616.2 nm was tracked when the alcohols were applied to the surface of the device. When methanol is applied, the resonance shifts 637.9 nm and again to 646.9 nm when acetone is applied. Again, similar to the trend observed in the zeroth order transmission, the strength in resonance decreases when both methanol and acetone were applied. However, not only does the first SPR peak from the left shifts for different alcohol. Both the peaks at the longer wavelengths shift as well, consistent with the characteristic of the SPP; that the SPPs are sensitive to the conditions at the surface of a metal. However, unlike the trend observed for the first resonance that was tracked, the resonances at the longer wavelengths did not reduce in strength. Also, these resonances that occur at the longer wavelengths do not appear in the zeroth order transmission. The resonances in the first order diffraction occur close to the resonances observed in the zeroth order transmission as predicted by the simulation results in Figure 3.5. Therefore as the study showed in Section 3.3, the super-period allows the resonance observed in the zeroth order transmission to occur in the first order diffraction. The super-period also gives additional resonances not observed in the zeroth order transmission, as is clearly seen in the experimental results.

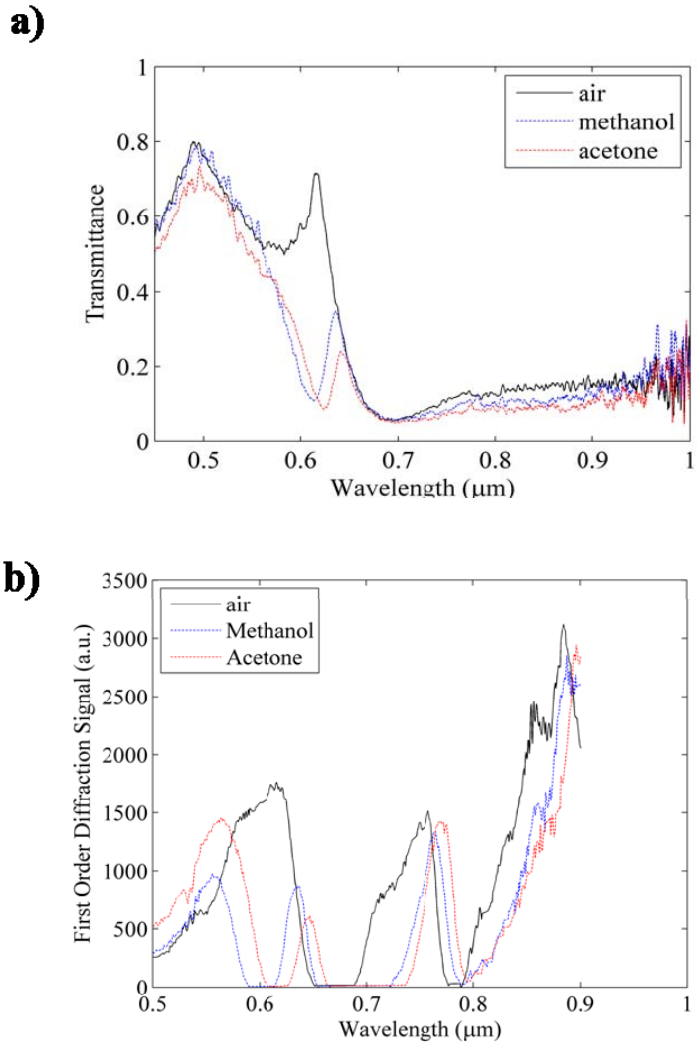

Figure 3.26 Experimental results obtained for the super-periodic nanoslit arrays with varying refractive indexes (air – black, methanol – blue, acetone – red). (a) 0^{th} order transmission (b) 1^{st} order diffraction.

Since the transmission resonance changes when the surface conditions change, these super-periodic nanoslit arrays are expected to be bio-chemical sensors. Hence, the sensitivity of the super-periodic nanoslit arrays is determined. The refractive index of the solutions, methanol and acetone are 1.3284 and 1.3586 respectively. The resonance wavelength induced from the four slits shifted from 616.2 nm to 636.9 nm when methanol applied to the surface device, and it shifted again to 645.9 nm when acetone

was applied to the surface device. Here, we define the sensitivity to be the shift in wavelength divided by the difference in refractive index between methanol and acetone and is found to be 298 nm/RIU. Tracking the resonances in the center of the spectrum, the SPR peak when the surface is in air is at the wavelength is 757.7 nm. The resonance wavelength shifted to 764.7 nm when methanol was applied and finally the resonance wavelength shifted to 769.2 nm when acetone was applied. The sensitivity for this resonance between methanol and acetone is found to be 149.0 nm/RIU. This means that the surface plasmon mode confinement at the first resonance of the spectrum from the left is much more confined than the mode confinement of the resonance the at the wavelength 757.7 nm. Unlike the conventional periodic nanoslit arrays, the super-periodic nanoslit arrays have two resonances to track in the first order diffraction. This additional resonance in the center of spectrum allows one to track both resonances and ascertain the difference between when sensing is required. To determine the capability of this method, the sensitivity here is compared with other known results. A group reported that using nanoslits with regular periodicity, this group has been able to achieve a sensitivity of 669 nm/RIU [70]. The sensitivity defined in this group is taken from the slope of the line of the resonance wavelength versus the refractive index. However the change in resonance wavelength in [70] as it approaches a refractive index of 1.342 from 1.333 is getting smaller. Should we take the resonance wavelength values at 1.342 and 1.342, respectively, it is found that the sensitivity is roughly 200 to 400 nm/RIU.

3.7 Spectral and angular dispersions

The super-periodic structure acts a resonance diffraction grating for spectral measurement because it disperses different wavelengths into different propagation

directions. This super-periodic device is also an integrated surface plasmon spectroscopic sensor for it combines the functions of a surface plasmon sensor and a spectrometer into a single device. In this section, the angular and spectral dispersions of the integrated surface plasmon spectroscopic sensor are discussed. The angular dispersion of this device is the mapping between the variation in the angle of diffraction and the corresponding wavelength. The angular dispersion can be derived from the dispersion relation

$$\frac{2\pi}{\lambda}\sin\theta = \frac{2\pi}{\Lambda}, \tag{3.5}$$

where λ is the wavelength, θ is the angle of diffraction and Λ is the super-period. Taking the derivative of the equation, one will arrive at the angular dispersion,

$$\frac{d\theta}{d\lambda} = \frac{1}{\sqrt{\Lambda^2 - \lambda^2}}. \tag{3.6}$$

The spectral resolution is the ability of the spectrometer to resolve features in the electromagnetic spectrum. It tells how each wavelength is dispersed laterally in the imaging plane of the CCD. The spectral resolution is obtained by inserting the dispersion relation, equation (3.5) into the trigonometric equation

$$\tan\theta = \frac{x}{z}, \tag{3.7}$$

where x is the distance of the diffracted wavelength from the incident plane, and z is the distance from the super-period nanoslit arrays to the image plane. Taking the derivative on both sides, one would arrive at the equation

$$d\lambda = \frac{dx}{z}\frac{\left(\Lambda^2 - \lambda^2\right)^{3/2}}{\Lambda^2}, \tag{3.8}$$

where dx is distance between the pixels on the CCD which is 5.6 μm. The spectral resolution of the commercial spectrometer used in the experiment is 2.0 nm. From

equation (3.8), the spectral resolution of the super-periodic nanoslits, calculated at the 615 nm wavelength and with the distance between the device and the CCD plane being 14.5 mm, is 0.7 nm. The small difference of resonance wavelengths measured with the external optical spectrometer and the super-periodic nanoslit arrays is within the uncertainty range of the external optical spectrometer and the measurement technique used here.

To summarize this chapter, the SPR in super-periodic nanoslit arrays was characterized by studying the transmission resonances arising from the super-periodic nanoslits. It was found that the super-period excites more surface plasmon modes that are typically not generated from the regular periodic nanoslit arrays. Also, transmission resonance associated with the fundamental surface plasmon mode is seen in the first order diffraction. This is because at that wavelength, the first order diffraction is not evanescent as oppose to the regular periodic nanoslit arrays. Additionally, it was found that the resonances in the first order diffraction better reveals the resonances in the near-field than the resonances seen in the zeroth order transmittance.

CHAPTER 4

SURFACE PLASMON RESONANCE IN SUPER-PERIODIC NANOHOLES

In the previous chapter, the transmission resonance characteristics associated with the SPR in the super-periodic nanoslit arrays have been investigated. The super-period excites more surface plasmon modes and the fundamental mode can be observed in the first order diffraction. In this chapter, the SPR in the super-periodic nanohole arrays are investigated. Unlike the nanoslits, the nanoholes are two-dimensional structures on a surface plane. Before delving in the surface plasmon characteristics of the super-periodic nanohole arrays, the surface plasmon in periodic nanohole arrays are briefly reviewed.

4.1 Surface plasmon resonance in regular periodic metal nanohole arrays

Like the nanoslits, the effects of surface plasmons in nanohole arrays are observed in the transmittance spectrum as resonances. These resonances are called the extraordinary optical transmission (EOT) phenomena. The near-field effects of the surface plasmons aid in enhancing the field at the aperture and thus increasing radiation power in the far-field. EOT is a phenomenon where more light is transmitted across the film per unit surface area. EOT through periodic nanohole arrays in opaque metal films was first reported in 1998 [16]. Prior to the discovery, it was initially thought that the

transmission efficiency of light through the aperture in an opaque metal would follow the scale $(r/\lambda)^4$, where *r* is the radius of the aperture and λ is the wavelength. The optical transmission would drop rapidly as λ becomes larger than the *r* [71, 72]. This means that light cannot propagate through the aperture if the wavelength of the light, λ, is greater than four times the radius of the aperture, *r*. In addition to that, the transmission efficiency also drops exponentially across the metal film. Hence, in a sense, the light passing through an aperture much smaller than the incident wavelength will suffer high attenuation. However, due to improved nanofabrication technology, it was found that periodic subwavelength apertures in metallic films were shown to increase transmission efficiency at certain wavelengths larger than the period, debunking the traditional thought that the transmission efficiency through an aperture in a metallic film will drop exponentially.

An example of the extraordinary optical transmission phenomenon is shown in Figure 4.1. Light is normally incident unto the perforated 100 nm-thick gold film that is placed on a glass substrate. The radius of the circular apertures is 70 nm and the period of the square array is 420 nm. The transmission efficiency divided by the fraction of the surface area occupied by the holes shows that the absolute transmission efficiency is greater than unity. Because the thickness of the film is 100 nm, being an order thicker than the skin depth, light impinging unto the 'opaque' part of the film does not tunnel across the film and thus does not contribute to the overall absolute transmission efficiency.

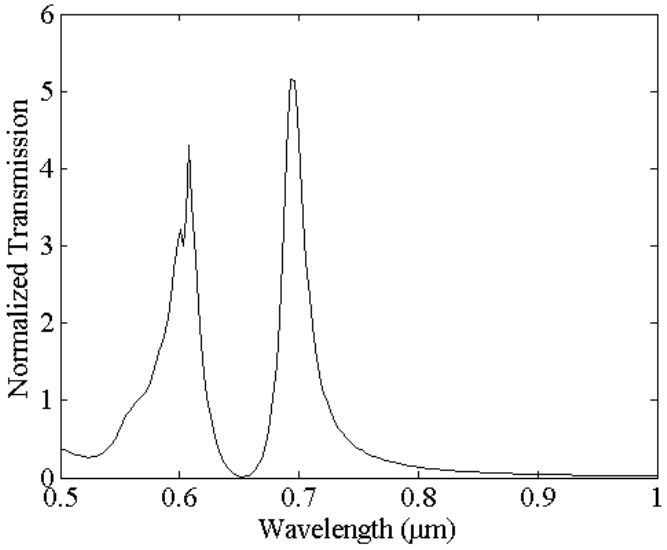

Figure 4.1 Normal-incidence transmission spectrum for a thin gold film with square array of holes of radius, r = 70 nm and period, p = 420 nm. The thickness of the gold film is 100 nm. The transmission is normalized to the area of the hole.

Figure 4.1 shows that EOT occurs at the wavelengths, 600 and 700 nm, of which both are longer than the period of the nanohole array. And according to the diffraction theory, it is impossible for light to propagate through the hole at these wavelengths, without assuming the presence of surface modes. Therefore, it is suggested that the EOT resonances are due to surface plasmons acting as 'carriers', carrying light incident across the film and radiating it into the far-field on the other side. The role of surface plasmons in EOT has been thoroughly investigated both experimentally [73-81] and theoretically [82-100] for the past decade.

The mechanism of the EOT phenomenon can be explained as follows. Light is incident on the nanohole arrays. The periodic corrugation of the metal film provides additional momentum to excite the SPPs at the incident surface. The excited SPPs and then couples with the incident field to tunnel across the metal film through the apertures.

The field exiting from the apertures then couples with the SPPs on the exiting side that enhances the fields at the apertures. Light is then decoupled from the SPPs and radiates into the exiting medium. When the momentum-matching condition is applied, one can see that the transmission resonance at normal incidence can be approximately predicted by the dispersion equation show in (4.1), where ε_d is the permittivity of the incident medium and ε_m is the permittivity of the metal. This equation shows that the SPPs on the incidence side are excited by the momentum due to the period of the circular nanoholes in both *x*- and *y*- directions.

$$k_0 \sqrt{\frac{\varepsilon_d \varepsilon_m}{\varepsilon_d + \varepsilon_m}} = k_0 \sin\theta \pm \frac{n2\pi}{\Lambda_x} \pm \frac{m2\pi}{\Lambda_y} \tag{4.1}$$

Figure 4.2 plots the resonance wavelengths of the EOT and the corresponding wavelengths determined from equation 4.1. Because equation (4.1) does not account for the scattering loss due to the shape of the apertures, the interference effects between the adjacent holes that contribute to the resonance shift is disregarded. Hence, the resonances occur at a longer wavelength than that predicted by equation (4.1). Geometrical parameters of the periodic nanohole arrays affect the SPPs and thus the EOT resonances. For example, the thickness of the metal film influences the spectral placement and the broadening of the EOT resonances. When the thickness of the metal is within the skin depth range, two characteristics of the EOT resonance change. Not only does the EOT resonance blue shifts, the FWHM of the EOT resonance broadens as well. These changes are due to the coupling of both the asymmetric and symmetric SPPs modes when the film is thinner than the skin depth of the metal film [91]. Also, considerably more light is transmitted across the film when the thickness of the metal film is reduced.

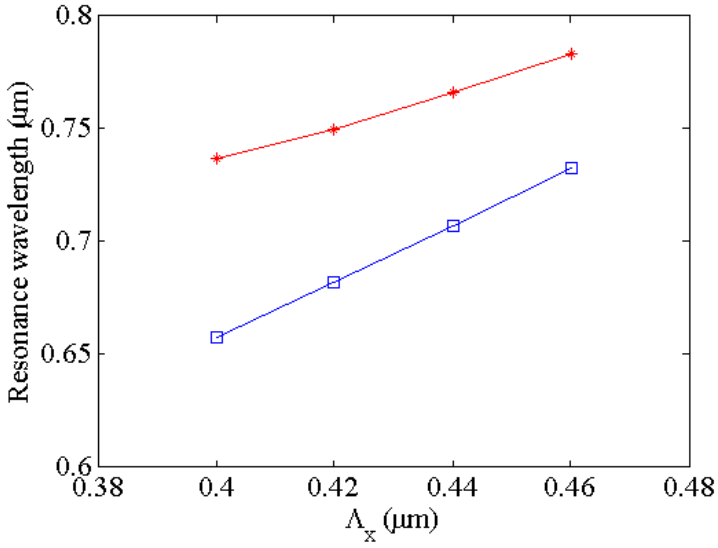

Figure 4.2 The red-star lines correspond to the EOT resonance calculated using Lumerical FDTD solutions and the blue-square lines correspond to the resonance wavelengths computed from Equation 4.1.

The SPPs are not the sole contribution to the EOT resonance. LSP also play an important role in the EOT phenomenon. When the hole is illuminated, the LSP are excited on the rim of the hole on the exit side [101]. The surface plasmon modes are localized on the sides of the rim where they are parallel to the electric field polarization. On the exiting interface, the field at the center of the aperture behaves like a dipole-moment, similar to its complementary counterpart, a metallic nanosphere [102, 103]. The field at the rims is enhanced which leads to an increase in the transmission resonance where the LSP mode is. The localized modes can be seen in Figure 4.3, where the electric field enhancement of a single hole in a periodic array on the exit side is being plotted. The field is strongest at the edges of the rim parallel to the electric field polarization and has an enhancement of about 90 times the incident field.

However, recent studies show that the near-field enhancement at a wavelength that is slightly shifted then the resonance observed in the far-field transmission [104]. The

shape of the aperture influences the field localized at the aperture [74]. This can be easily seen when changing the shape of the aperture from a circle to a rectangle. The rectangular aperture emits a resonance at a wavelength much longer than the circular apertures. For an array of holes, the field at the aperture is influenced not only by the shape but also by the fields excited from adjacent apertures [4, 26, 88, 105].

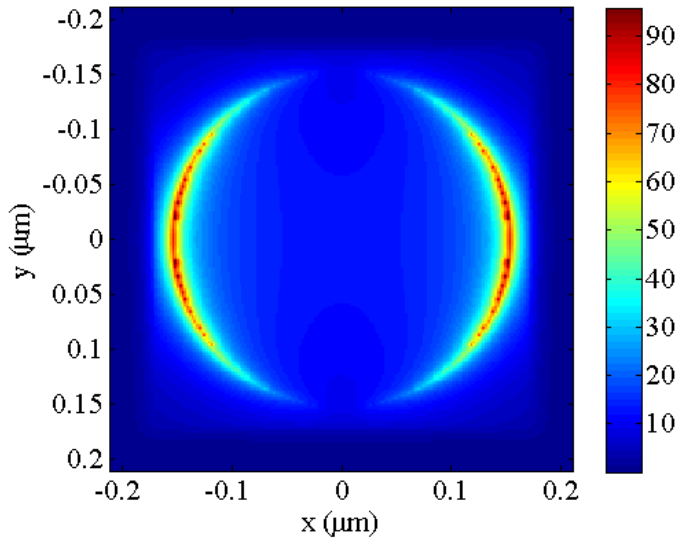

Figure 4.3 The electric field intensity of the circular aperture at the surface on the transmitting side. The light is polarized in the x-direction, causing surface plasmons to congregate at the edges along the polarized direction.

The emergence of the EOT phenomenon in nanohole arrays has been recently used in many applications because of their near-field and resonance line-width properties. A research field that has an extensive research on nanohole arrays is the bio-chemical sensing area. Much work has been put into optimizing the functions of the nanohole arrays, integrating them into microfluidic systems [106-108].

4.2 Surface plasmon resonance in super-periodic metal nanohole arrays

In the previous section, the surface plasmons in regular periodic nanohole arrays were discussed and it was shown that surface plasmons enhance the transmission of light across the perforated metal film. The surface plasmons are excited by the corrugation of the metal and the frequency of which EOT occurs depend on the period of the nanohole arrays. Also, the behavior of the electric field at the surface of the metal on the transmitted side was shown. Here, in this section, the surface plasmons in super-periodic nanohole arrays are presented and studied against the regular periodic nanohole arrays.

The super-periodic metal nanohole array is a one dimensional grating that has nanohole arrays that spread out in two directions on the surface plane, illustrated in Figure 4.4. In one direction, the period remains the same throughout. In another direction, however, there exists two periods, where one is a multiple of the other. The two periods that exist within the same direction creates the super-period. The super-periodic metal nanohole arrays consist of a small period (p) that is smaller than the surface plasmon resonance wavelength. The small period of the nanoholes are arranged within a larger period (P) in one-dimension. The large super-period (P) is five times of the small period (p). Here, the thickness of the metal film was set at 50 nm and the choice of metal is gold. As was mentioned earlier, EOT occurs in metal films that are less than the skin depth. The super-periodic nanohole arrays device is placed on a quartz substrate. Because the super-periodicity is applied only in one direction, the device is investigated under two polarizations, TE and TM for it was learnt that the polarization of the incident field excites different surface plasmon modes. TE polarization is when the electric field is

parallel to the grating lines while TM polarization is when the electric field is perpendicular to the grating line.

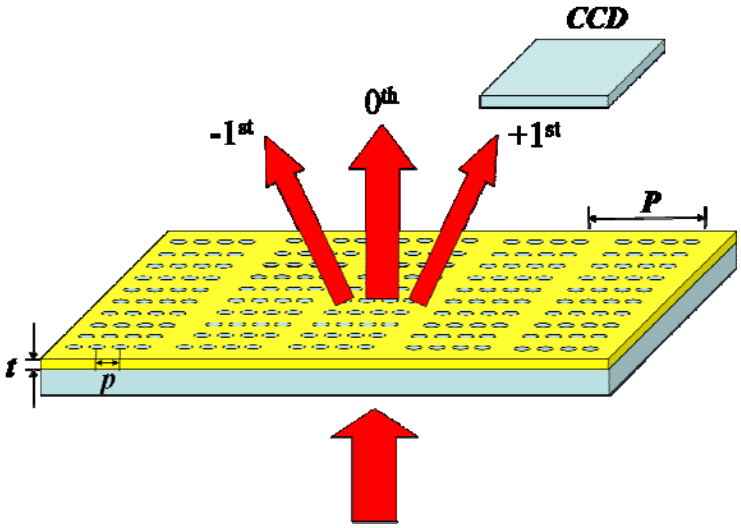

Figure 4.4 A super-periodic nanohole array with small period (p) and larger period (P).

First, the super-periodic nanohole array is investigated under the TE polarization, when the electric field of the incident field is polarized parallel to the grating lines.

4.3 Surface plasmon resonance in a super-periodic gold nanohole arrays under the TE polarized light excitation

To determine the transmission characteristics of the super-periodic nanohole arrays illuminated with TE polarized light at normal incidence, the zeroth order transmission and the first order diffraction from the super-periodic nanohole arrays were calculated. The calculations were carried out using a FDTD commercial software (Lumerical Solutions, Inc.). In the simulation setup, the plane wave is incident from the quartz substrate, 1.45 μm below the 50 nm thick gold film. The gold film was modeled according the Lorentz-Drude model [24]. Light is polarized in the y-direction as is

indicated by the arrows in Figure 4.5. The size of the FDTD simulation region was set at the length of the super-period, 2100 nm in the x-direction and 420 nm in the y-direction. Because the simulation region was periodic in both x and y directions and was symmetric about the center, the boundary conditions in x and y directions can be set at 'symmetric' and 'anti-symmetric' boundary conditions, respectively. 'Symmetric' boundary condition is used when the electric field polarization is parallel to the boundary, where else the 'anti-symmetric' boundary condition is used when the electric field polarization is perpendicular to the boundary. The boundary condition used at the top and bottom (z direction) of the simulation region are the perfectly matched layers (PMLs) that absorb nearly all of the power. They were both set at 1.5 μm away from the center, one in the positive z-direction and the other in the negative z-direction. The zeroth order transmission and the first order diffraction were obtained by putting a monitor 1.45 μm away from the center of the simulation region, above the gold film. Using the algorithm provided by the commercial FDTD software, the zeroth order transmission and the first order transmission were extracted from the data collected by the monitor in the transmitted region. The range of the light spectrum was in between 500 and 1000 nm. The data points calculated were set at 500 points. The accuracy of the calculation was determined by the optimization algorithm provided by the commercial software. It optimizes between the size of the mesh and the convergence of the result. For greater accuracy, the accuracy of the calculation was set at the highest, 8. The simulation time was set long enough to account for the decay of the field in the metal, at 400 femtoseconds.

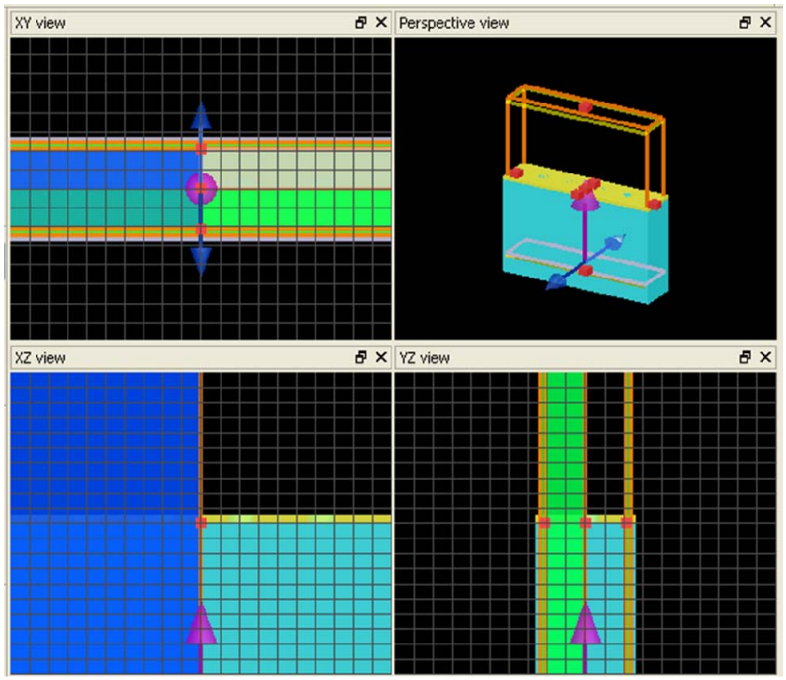

Figure 4.5 Simulation setup of the super-periodic nanohole arrays. The purple arrow indicates the direction of plane wave propagation. The blue arrows represent the direction of the electric field polarization.

The zeroth order transmission and the first order diffraction spectrums were calculated and are shown in Figure 4.6. The zeroth order transmission and the first order diffraction spectrums are represented by the black dashed line and the solid red line, respectively. Clearly seen are two surface plasmon modes excited in the device as resonances in both the zeroth order transmission and the first order diffraction. These two resonances observed both in the zeroth order transmission and the first order diffraction resemble closely to the resonances observed for the regular periodic nanohole arrays. However, at close inspection, the resonances in the zeroth order transmission do not coincide with the resonances in the first order diffraction. The resonance at the longer wavelength corresponds to the excitation of the surface plasmons at the 'substrate mode' because it gives a stronger electromagnetic field enhancement in the metal-substrate

interface. For the 'substrate surface plasmon mode', the resonance wavelength observed in the zeroth order transmission is at 761.3 nm and the resonance wavelength found in the first order diffraction is at 751.3 nm. The resonance at the shorter wavelength corresponds to the excitation of the surface plasmons at the 'air mode', because it gives a stronger electromagnetic field enhancement in the metal-air interface. This mode occurs at the wavelength 618.1 nm in the zeroth order transmission and at 620.6 nm in the first order diffraction.

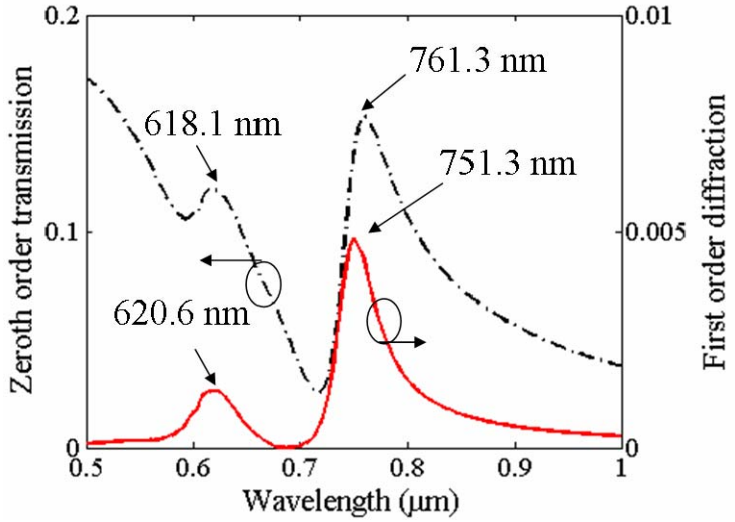

Figure 4.6 Calculated zeroth order transmittance (black dashed curve) and the first order diffraction (red line curve) from a superperiodic nanohole array device.

It is important to note that previously without the presence of the super-period, the EOT wavelength is evanescent in the first order diffraction. The discrepancy in the resonances observed in both the zeroth order transmission and the first order diffraction can be explained by further investigating the electric field near the surface of the metal. Figure 4.7 shows the electric field distribution on the plane 20 nm above the surface of the super-periodic nanohole arrays at the peak wavelengths near the near-infrared region

found in the zeroth order transmission and the first order diffraction. Figure 4.7(a) plots the electric field intensity at the wavelength 751.3 nm, the peak wavelength observed in the first order diffraction and Figure 4.7(b) plots the electric field intensity at the wavelength 761.3 nm, the peak wavelength observed in the zeroth order transmission. It is apparent that the electric field intensity at the wavelength 751.3 nm is much stronger than the electric field intensity at the wavelength of 761.3 nm. This indicates that the first order diffraction reveals near-field resonance of the super-periodic nanohole array better than the zeroth order transmission. The yellow shaded parts indicate that the field is strongest at the edges in the y-direction, parallel to the direction of the electric field polarization, as expected. For the surface plasmons would congregate at the edges that are perpendicular to the direction of the electric field polarization. In both figures 4.7(a) and (b), the electric field intensity is not equal in all of the holes. The electric field intensity is stronger in the two center holes than the holes at the side. This behavior has not been reported before but it seems that in a symmetric structure, the surface plasmons tend to congregate near the center of the structure as is demonstrated in Figure 4.7.

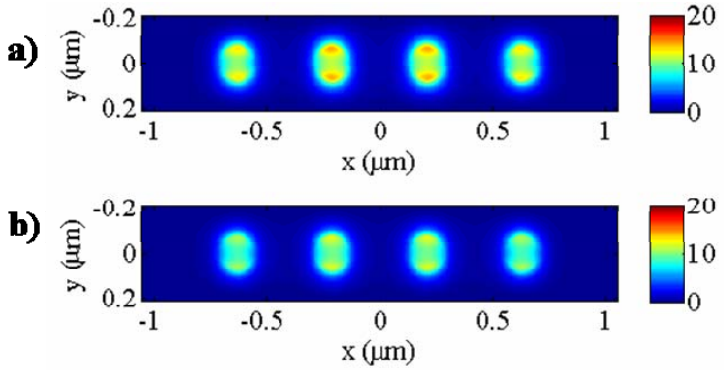

Figure 4.7 (a) Electric field intensity 20 nm above the metal surface at 751.3 nm wavelength; (b) electric field intensity 20 nm above the metal surface at 761.3 nm wavelength.

To determine the near-field resonance, two monitors were placed at the centers of the two holes within the super-period unit cell, 20 nm above the metal surface, where the electric field intensity is the strongest there. One monitor is placed at the center of one of the two ‘inner’ holes and one monitor is placed the center of one of the two ‘outer’ holes in the super-period unit cell. Figure 4.8 plots the electric field intensity versus wavelength captured 20 nm above the metal surface. The shape of the resonance shows that it is similar to the resonances seen in the zeroth order transmission and the first order diffraction. For the ‘outer’ hole, the near-field electric field intensity peaks at 749.5 nm, while for the ‘inner’ hole, the near-field electric field intensity peaks at 750.5 nm. The strength of the electric field intensity in the ‘inner’ hole is more intense than the electric field intensity at the ‘outer’ hole.

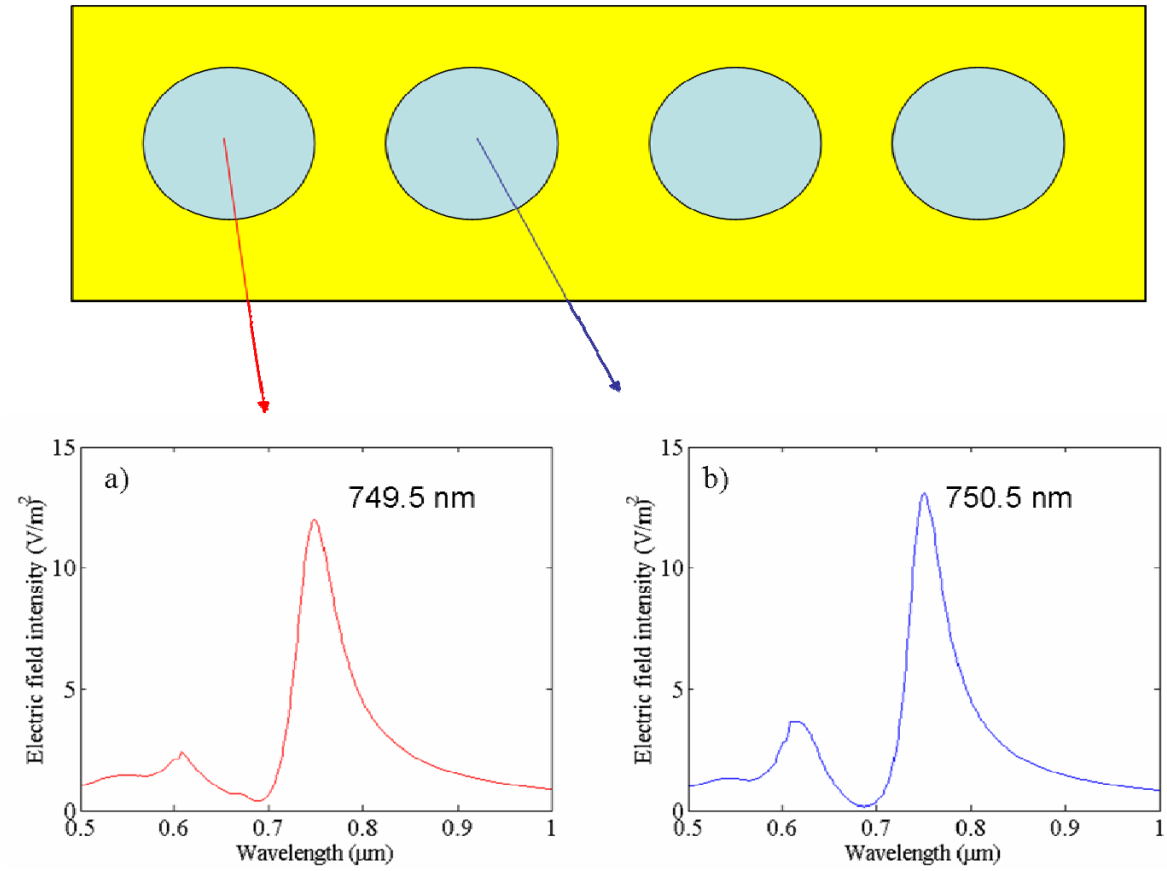

Figure 4.8 Electric field intensity 20 nm above the metal surface, where the monitor is placed above (a) the outer hole and (b) the inner hole.

Comparing the resonance wavelengths at the near-infrared region of all four spectrums, the zeroth order transmission, the first order diffraction, the near-field monitor in the 'inner' hole and the near-field monitor in the 'outer' hole, there is a trend that exists where the resonance wavelength for each of the four spectrums is at a shorter wavelength than the other. For the zeroth order transmission, the resonance wavelength is at 761.3 nm. For the first order diffraction, the resonance wavelength is at 751.3 nm. For the 'inner' hole monitor, the resonance wavelength is at 750.5 nm and lastly, for the 'outer' hole monitor, the resonance wavelength is at 749.5 nm. Discrepancy between the near field resonance wavelength and the far-field resonance wavelength for nanoparticles

has been documented and investigated [104,109-113]. The nanoparticles can be modeled as harmonic oscillators because they radiate fields in the far-field like nanoantennas. In general, there are two kinds of damping, one relates the electron collision and the other relates to the accelerating charge that radiates energy. When the accelerating electron releases energy in the form of radiation, by conservation of energy, the electron loses its kinetic energy. This lost in kinetic energy results in a red-shift of the resonance wavelength in the near-field spectrum. Yet, however, in this case for super-periodic nanohole arrays, the near field resonance wavelength is blue-shifted relative to the zeroth order transmission and the first order diffraction resonances.

In Figure 4.9, the electric field intensity taken at different heights above the surface of the perforated metal film is plotted. From the plot, it shows that the electric field intensity drops with distance away from the surface of the metal film. This is consistent with the characteristic of the surface plasmons that is strongest at the surface of the metal film and decays with distance away from the film.

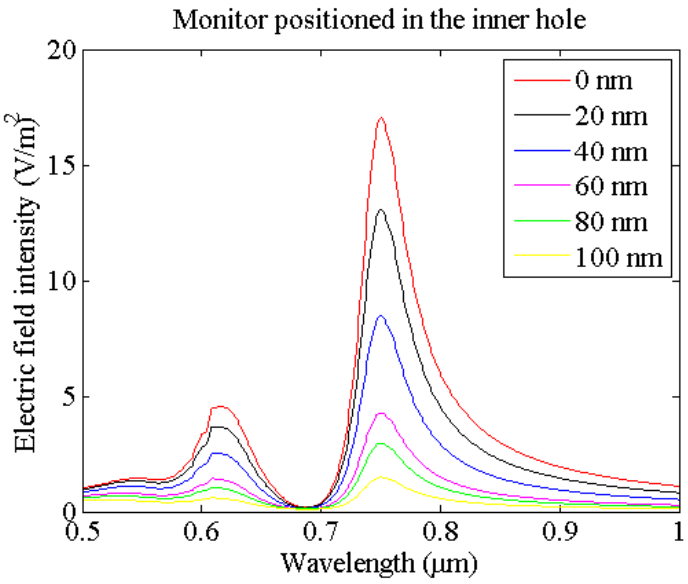

Figure 4.9 Electric field intensity as a function of wavelength plotted with different distances away from the surface of the metal film.

The zeroth order transmission and the first order diffraction of the super-periodic nanohole arrays when illuminated with the TE polarized light at the normal incidence were confirmed experimentally. The super-periodic nanohole arrays were etched in a thin gold film on a glass substrate and spanned the area of 300 x 300 μm^2. The holes were 140 nm in diameter and the spacing between the holes, period, is set at 420 nm. The super-period is five times the period and is 2100 nm. The electron beam lithography process was employed to fabricate these nanoholes, similar to the process used to fabricate the nanoslits. First, 60 nm of gold was sputtered unto a glass substrate that was cut into approximately 3 x 3 mm pieces. The glass substrate was prepared by first cleaning it with soap water. Organic residues were removed by immersing the glass substrate in an acetone bath for about 10 minutes. Then the glass substrate was placed in methanol bath for 5 minutes. The glass substrate was then rinsed with de-ionized (DI) water and then blow-dried with nitrogen. The electron-beam photoresist, ZEP-520A was spin coated

atop the glass substrate chip at the speed of 4000 RPM which gave a thickness of approximately 350 nm. ZEP-520A was chosen because of its strong resistance towards the mechanical plasma etching method. The photoresist was then baked on the hot plate at 180°C for 3 minutes. The pattern was transferred unto the photoresist via electron beam at 30kV. The amount of electron dose that was applied was determined by the amount of coulomb charge per area. And that amount was 100 $\mu C/cm^2$. Once the pattern has been written on the photoresist, the sample was then developed for 3 minutes in the ZED-N50 developer. With the photoresist as the mask, transference of pattern from the photoresist to the gold film was done via reactive ion etching (RIE) using Argon as the etching agent. The etching time was 20 minutes. Figure 4.10 shows the SEM image of the fabricated super-periodic nanohole array.

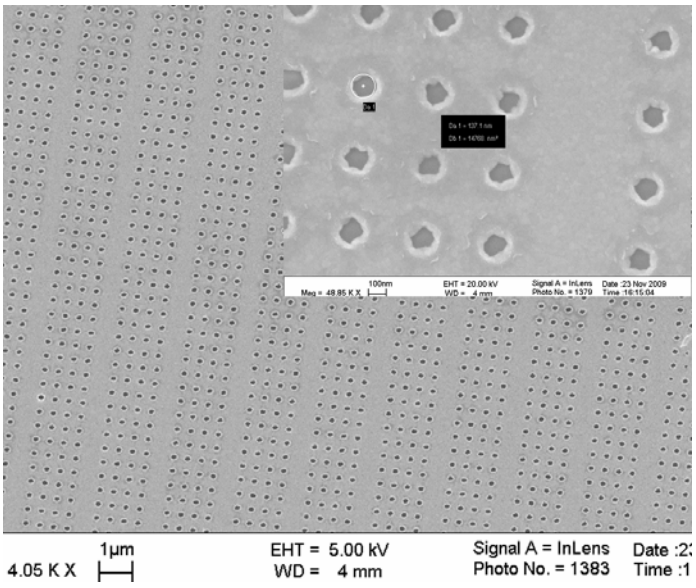

Figure 4.10 A SEM image of the fabricated super-periodic nanohole arrays.

The super-periodic nanohole arrays were fabricated and characterized using the same technique and experimental setup used to fabricate and characterize the 1-D nanostructures. The distance between the zero order HeNe laser beam and the first order diffraction HeNe laser beam is 4.0056 μm. This value is achieved by first capturing the image of the zero order HeNe laser beam at the first position and finding its maximum value on the image. Next, the CCD is moved 4 mm in the direction of the first order diffraction beam and the image of the first order diffraction was captured there. Once the maximum value was determined, the difference in between the two maximum peaks in the images is then added to the overall distance of 4 mm. Using trigonometric relations described in Section 3.5, the distance between the super-periodic device and the CCD is 12.6751 mm.

First, the transmission characteristics of the super-periodic circular nanohole arrays were investigated under TE polarization. Using the polarizer, the electric field of the broadband laser was aligned along the 'grating lines' of the super-periodic nanohole array. To determine maximum diffraction possible, the nanostructure was aligned so that the all of the beam power was within the total area of the nanostructure. With the CCD, the angular distribution of the first order diffraction was captured versus the wavelength when there was no chemical presence on the device. Figure 4.11 shows the single-shot image captured by the CCD for the TE polarization incidence. By color-mapping the image in Figure 4.11, two bright spots are seen near the center of the image. The brighter the spots are, the greater the intensity. The two bright spots here in Figure 4.11 correspond to two surface plasmon resonances of the super-periodic nanohole arrays.

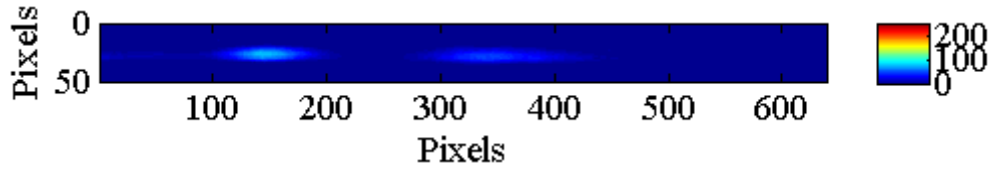

Figure 4.11 False-color image of the first order diffraction captured by the CCD when no chemical is present on the super-periodic nano-hole array for TE polarization.

Figure 4.12 show the false-color images when different chemicals are applied on the surface of the super-periodic nanohole arrays. The top, middle and bottom images correspond to the first order diffraction captured for air, methanol and IPA refractive index respectively. By simply comparing the position of the bright spots for the different refractive index, the bright spots shift to the right when methanol and IPA were applied. The false-color images translate to the intensity of the first order diffraction recorded as a function of the diffracted wavelength.

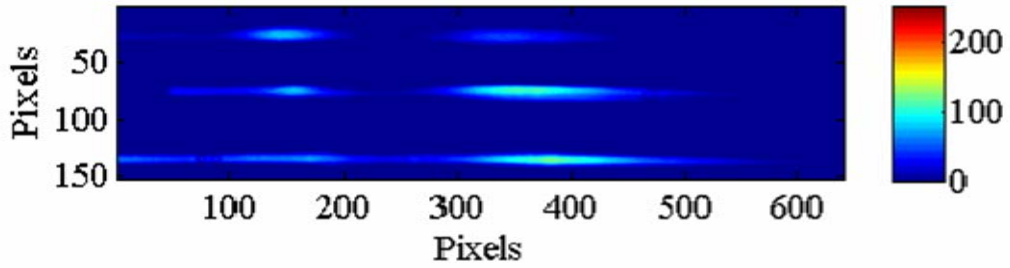

Figure 4.12 Angular dispersed first order diffraction captured by the CCD when the device was exposed (a) in the air, (b) methanol, and (c) isopropyl-alcohol.

Figure 4.13(a) shows the zeroth order transmission spectra for the different chemicals and Figure 4.13(b) shows the first order diffractions spectra for different chemicals. The vertical axis in Fig. 4.13(b) has an arbitrary unit that is proportional to the

intensity of the first order diffraction. For each row of the 640x480 CCD, the signal in each pixel of the columns is summed up. The signal is then corrected with the responsitivity of the CCD to obtain the first order diffraction. After conversion, two resonance peaks are seen. When chemicals were applied, the peak wavelengths in the first order diffraction were shifted. It can be seen that the strength of the shorter wavelength resonance was reduced with increased refractive index. Tracking the resonance at the longer wavelength for first order diffraction, Figure 4.13(b), the resonance wavelength shifted from 778.4 nm (air) to 796.1 nm when the methanol was applied to the surface area, and shifted to 808.6 nm for IPA. For the zeroth order transmission, tracking the resonance at the longer wavelength, the resonance wavelength shifted from 790.1 nm (air) to 805.9 nm when methanol is applied and to 813.9 nm when IPA is applied.

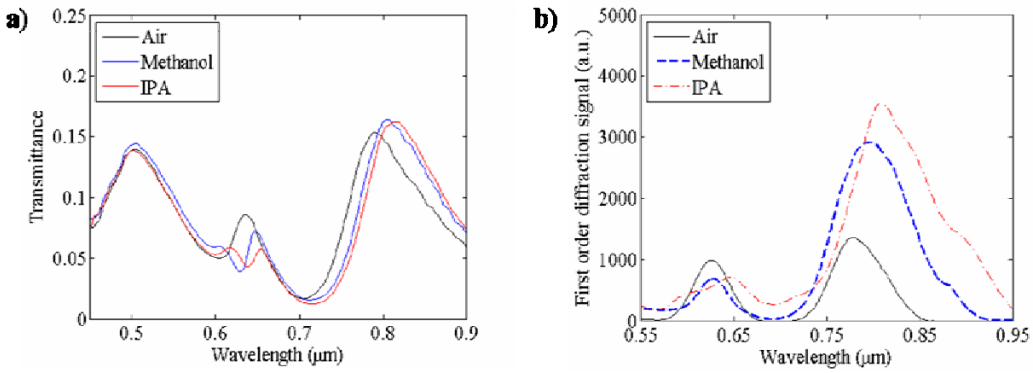

Figure 4.13 Measured surface plasmon resonance spectra with different chemical liquids applied in the super-periodic nanohole arrays from: (a) zeroth order transmission using a spectrometer, and (b) the first order diffraction using the CCD.

The peaks observed in the zeroth order transmission correspond to the excitation of surface plasmons generated by the nanohole arrays. In the first order diffraction, the

surface plasmon resonances are blue-shifted that of the resonance observed in the zeroth order transmission. The discrepancy observed here in the zeroth and first order diffractions show that plasmonic resonance is red-shifted relative to the near-field resonance, as was shown in Figure 4.6. Calculating the sensitivity based on the resonance wavelength shift from methanol to IPA observed in the first order diffraction, the sensitivity is 256 nm per RIU.

4.4 Surface plasmon resonance in a super-periodic gold nanohole array under the TM polarized light excitation

The characteristics of surface plasmons in the super-periodic nanohole arrays illuminated with TE polarized light have been presented in the previous section. When the super-periodic nanohole arrays are illuminated with TE polarized light, the surface plasmon resonance not only manifests itself in the zeroth order transmission spectrum, but also in the first order diffraction, which was previously not possible with the regular periodic hole arrays, as the surface plasmon resonance always occur at wavelengths larger than the period, where the first order diffraction is evanescent. It was found that at resonance, the surface plasmons tend to congregate more at the edges of the centre holes than the edges of the holes at the extremities. At the center holes, the near-field electric field intensity spectrum resembles the first order diffraction spectrum, although the resonance in the first order diffraction peaks at a slightly different wavelength.

In this section, the surface plasmons in the super-periodic nanohole arrays when illuminated with TM polarized light at normal incidence is investigated. The zeroth order transmission and the first order diffraction from the super-periodic nanohole arrays were calculated using the commercial software, Lumerical Solutions, Inc. The simulation setup

is similar to the TE polarization case, except that the electric field polarization of the incident field is in the x-direction, along the super-period vector and the boundary conditions in x and y directions are different. The boundary conditions in x and y directions were set at ‘anti-symmetric’ and ‘symmetric’, respectively as shown in Figure 4.14.

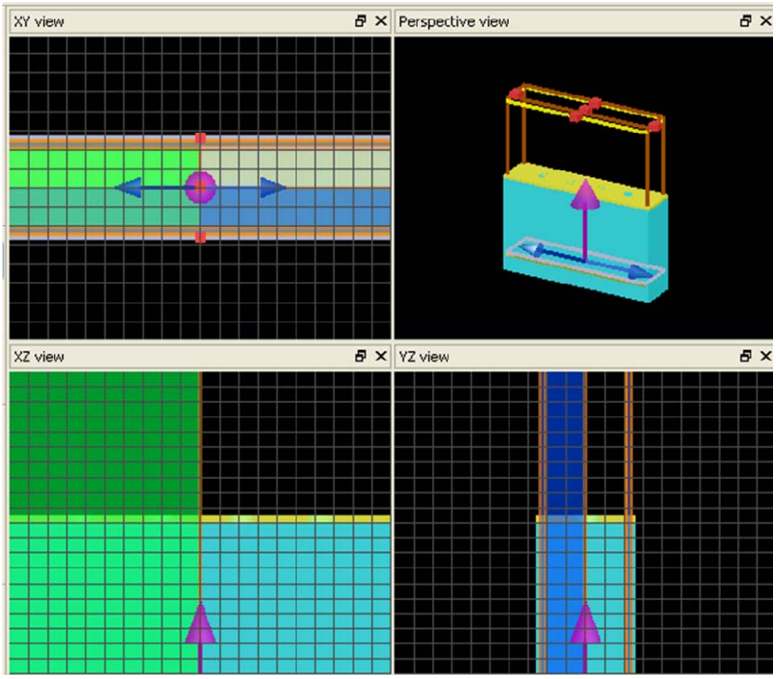

Figure 4.14 Simulation setup of the super-periodic nanohole arrays when illuminated with TM polarized light. The electric field polarization (blue arrows) is in the x-direction, parallel to the super-period grating vector.

The zeroth order transmission and the first order diffraction spectrums were calculated and are shown in Figure 4.15. The zeroth order transmission and the first order diffraction spectrums are represented by the black dashed line and the solid red line, respectively. The super-periodic nanohole array under TM polarization presents a different kind of excitation as the periodic chain of nanoholes perpendicular to the grating

line, is perturbed by an 'empty' space after every four equally spaced holes. Fig. 4.15 shows the calculated spectra of the zero-order transmission (black dashed line) and the first order diffraction (solid red line) from the device. There are three resonances observed here, more explicitly in the first order diffraction. The resonances in TM polarization appear in a similar manner when illuminated under TE polarization, where the highest resonance frequency exhibits lesser strength to the resonances at the longer wavelengths. In the zeroth order transmission, the two peaks at the longer wavelengths are at 758.5 nm and at 838.7 nm. In the first order diffraction, the two peaks are at 731.5 nm and at 835.7 nm.

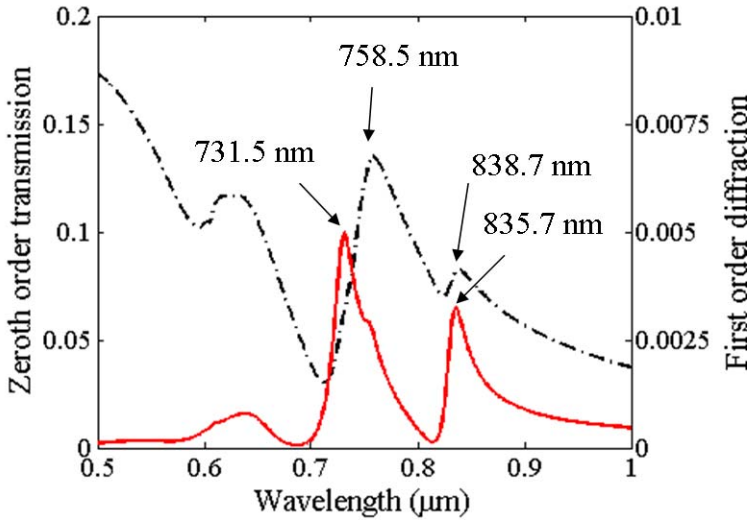

Figure 4.15 Calculated zeroth order transmittance (black dashed curve) and the first order diffraction (red line curve) from a superperiodic nanohole array device under the TM polarization excitation.

The resonances observed in the first order diffraction when the device was illuminated with TM polarization shows that the resonance wavelengths occur either at a shorter or longer wavelength than the resonance wavelength observed in the first order diffraction when the device is illuminated with TE polarization. For the TE polarization,

the resonance wavelength in the first order diffraction, at the longer wavelength is at 751.3 nm, in between the resonance wavelengths at 731.5 nm and 835.7 nm for TM polarization. This indicates that the surface plasmon mode observed for TE polarization has been split into two modes, each at a higher and a lower energy. The splitting of the surface plasmon mode is caused by the super-period, when the electric field polarization is polarized parallel to the super-period grating vector. For regular periodic nanohole arrays, the surface plasmon mode is excited by the grating period. For the super-periodic nanohole arrays, the surface plasmon mode is excited by the 'inner period', but is then split into two surface plasmon modes by the super-period. The super-period effect on the surface plasmon mode can be seen in Figure 4.16. The zeroth order transmission and the first order diffraction are plotted as functions of incidence wavelength, with varying super-period lengths from four times the length of the inner period to eight times the length of the inner period. The definition of the super-period as defined earlier means that after a certain multiple of 'inner period', one array of nanoholes is being 'removed'. As an example, four times the length of the super-period means that after three columns of nanoholes, a column of nanoholes is 'removed'. Eight times the length of the 'inner period' would mean that there are seven columns of nanoholes and one column with no nanoholes. The mode-splitting effect be easily seen in the first order diffraction and it shows how the super-period effects the shift of the longest resonance wavelength. As the super-period is increased from four times the length of the 'inner period' to seven times the length of the 'inner period', the longest resonance wavelength is seen moving to a shorter wavelength. However, when the super-period is at eight times the length of the 'inner period', it can be seen that both the resonances at the longer wavelength has been

'merged' into one resonance at the center. The resonance wavelength at the center is only slightly affected by the super-period, slightly shifting about the 731.5 nm wavelength as shown in Figure 4.17 where the resonance wavelengths are plotted as a function of the super-period. To further see the relationship between the two resonances and the super-period, the difference in the resonance of the wavevectors is plotted as a function of the super-period grating vector and is shown in Figure 4.18.

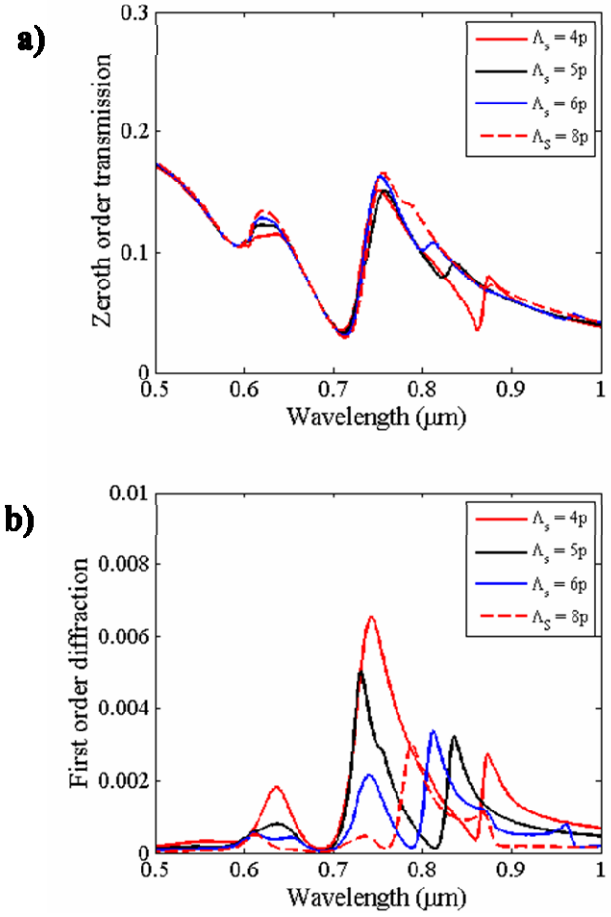

Figure 4.16 (a) The zeroth order transmission and (b) first order diffraction of the super-periodic nanohole arrays with different super-period lengths. The super-period lengths are displayed in terms of the multiples of the inner period.

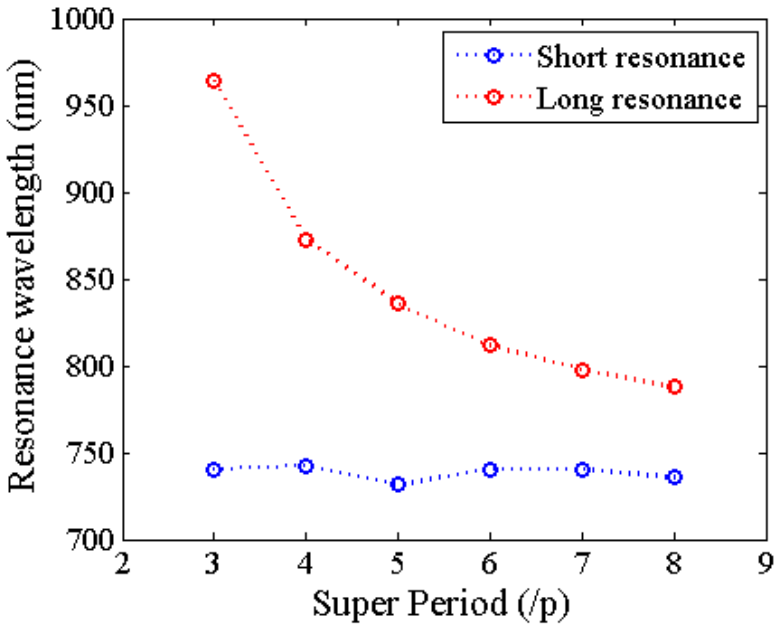

Figure 4.17 The resonance wavelengths in both the short (blue) and long (red) range plotted as a function of the super-period.

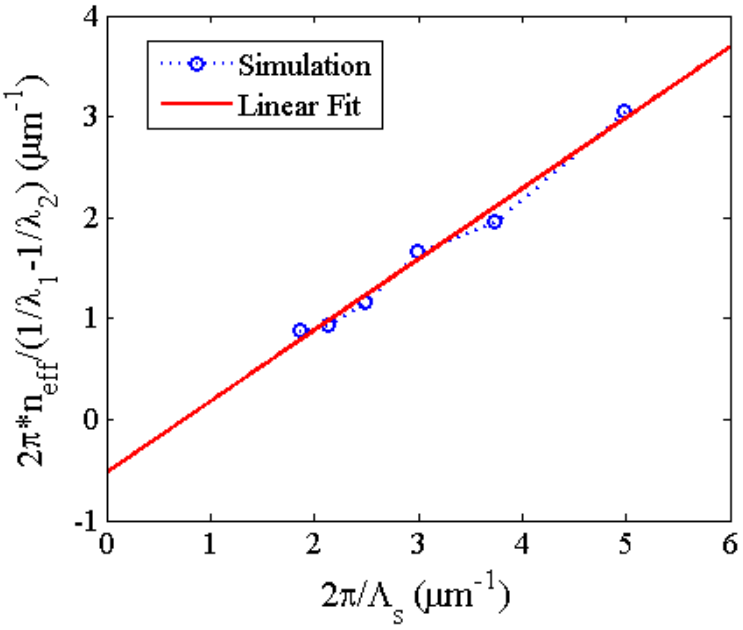

Figure 4.18 The difference in wavevector of the short and long resonance wavelengths plotted as a function of the super-period grating vector.

This mode-splitting effect can be seen in Figure 4.19, where it compares the resonances observed from the regular periodic nanohole arrays against the resonances observed from the super-periodic nanohole arrays. On the left axis of the figure, the zeroth order transmission of the regular periodic nanohole arrays and the super-periodic nanohole arrays are displayed, where else the first order diffraction is displayed on the right axis of Figure 4.19. In the zeroth order transmission the resonance wavelength of the regular periodic nanohole array is at 760.5 nm, in between the resonance wavelengths 758.5 nm and 838.7 nm, the resonance wavelengths for the super-periodic nanohole arrays. The presence of the super-period splits the surface plasmon mode at 760.5 nm into two degenerate surface plasmon modes at 758.5 nm and at 838.7 nm. The resonances seen in the first order diffraction are slightly blue-shifted from the resonances observed in the zeroth order transmission and they occur at 731.5 nm and the 835.7 nm. This is a unique characteristic of the super-periodic nanohole arrays, where the resonances in the first order diffraction are slightly blue-shifted to the resonances seen in the zeroth order transmission. This is also occurs when the super-periodic nanohole arrays are illuminated with TE polarized light. The resonances in the first order diffraction also have a better full width at the half maximum (FWHM) compared the resonances in the zeroth order transmission.

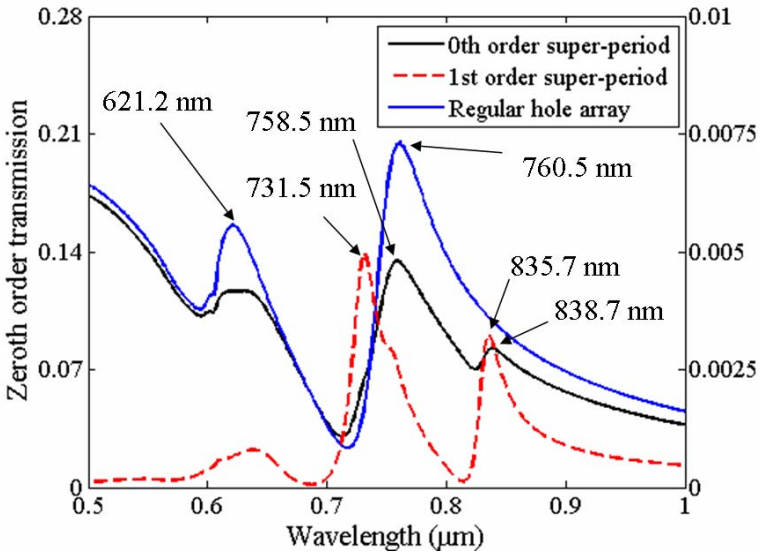

Figure 4.19 Calculated zeroth order transmission of the super-periodic nanohole array (black dashed curve) and the regular periodic nanohole array (blue solid line), and the first order diffraction (red dashed-line curve) from the super-periodic nanohole arrays.

The strength of the electric field intensity enhancement in the near-field, 20 nm away from the surface of the metal film is plotted as a function of wavelength in Figure 4.20 and this shows at which wavelength the electric field intensity enhancement is the strongest. The strength of the near-field electric field enhancement corresponds to the strength of the surface plasmon mode that was excited. Here, in Figure 4.20 the electric field intensity enhancement is taken 20 nm away from the surface of the metal film. The red and black solid lines correspond to the electric field enhancement captured above the center of the inner and outer holes, respectively. The near-field enhancement above the inner hole shows that in the longer wavelength, it peaks at two different wavelengths, 732.5 nm and 836.7 nm. The near-field peaks at slightly longer wavelengths than the peak wavelengths of the first order diffraction but shorter than the wavelengths observed in the zeroth order transmission. Unlike the near-field enhancement captured above the

inner hole, the near-field enhancement captured above the outer hole only presents one peak at the wavelength 749.5 nm. This shows that not all of the nanoholes within the unit cell of the super-period radiate equally, as oppose to the case when the super-periodic nanohole arrays are illuminated with TE polarized light. From this figure, one can identify that it is the inner hole that contributes to the resonance observed in the 800 nm region both in the zeroth order transmission and in the first order diffraction and that the surface plasmon modes radiating light from the inner and outer holes contribute to the resonance seen in the 700 nm region.

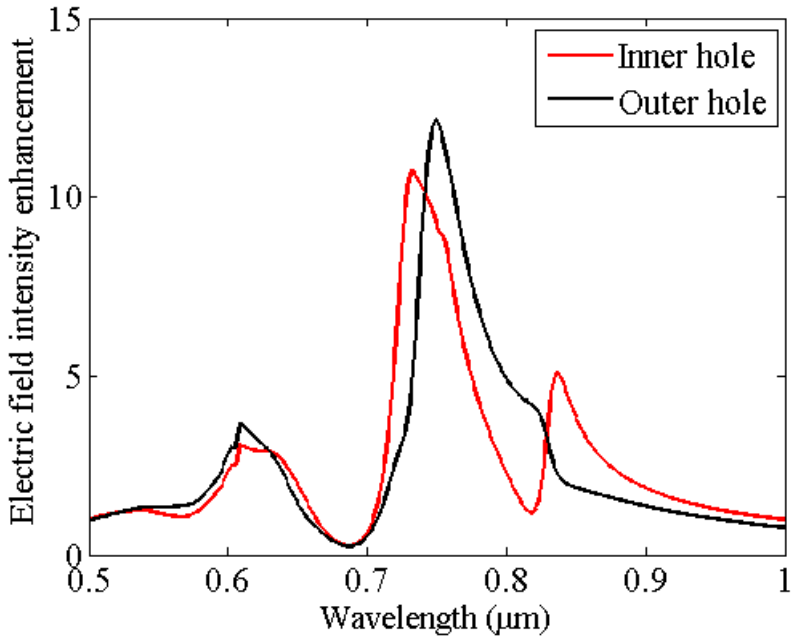

Figure 4.20 Electric field intensity enhancement of the super-periodic nanohole array, 20 nm away from the surface of the metal film. The red and black solid lines correspond to the electric field enhancement captured above the inner and outer holes, respectively.

The electric field intensity enhancement distributions were calculated on the plane 20 nm above the super-periodic nanohole arrays in a single unit cell of the super-period. First, the electric field intensity distribution of the resonances found in the near-field

monitor as shown in Figure 4.20 is plotted in Figure 4.21. The field distribution at the wavelengths 732.5 nm, 749.5 nm and 836.7 nm are plotted in Figure 4.21(a), (b) and (c), respectively. Between the figures (a), (b) and (c), the electric field intensity enhancement distributions are all possessing different patterns, indicating three different surface plasmons that were excited. In Figure 4.21(a), the field in all four nanoholes appears to be strongest at the edges in the direction towards the center of the unit cell. This implies that the surface plasmons are congregated towards the center of the unit cell, when this surface plasmon mode is excited. In Figure 4.21(b), the field distribution shows that the near-field enhancement is strongest at the edges in the outer holes, pointing towards the direction in the center of the unit cell. The field distribution in the inner holes however does not point in the direction towards the center, but rather to the edges of the unit cell. The field intensity enhancement is also greater than the field enhancement in Figure 4.21(b). In Figure 4.21(c), the field distribution shows that only that surface plasmons in the inner holes were excited. The field distribution within the inner holes is equal on both edges, unlike the field distribution in Figure. 4.21(a) and Figure 4.21(b). The electric field enhancement is weak and therefore shows that the surface plasmon mode is strongly coupled to the incident field.

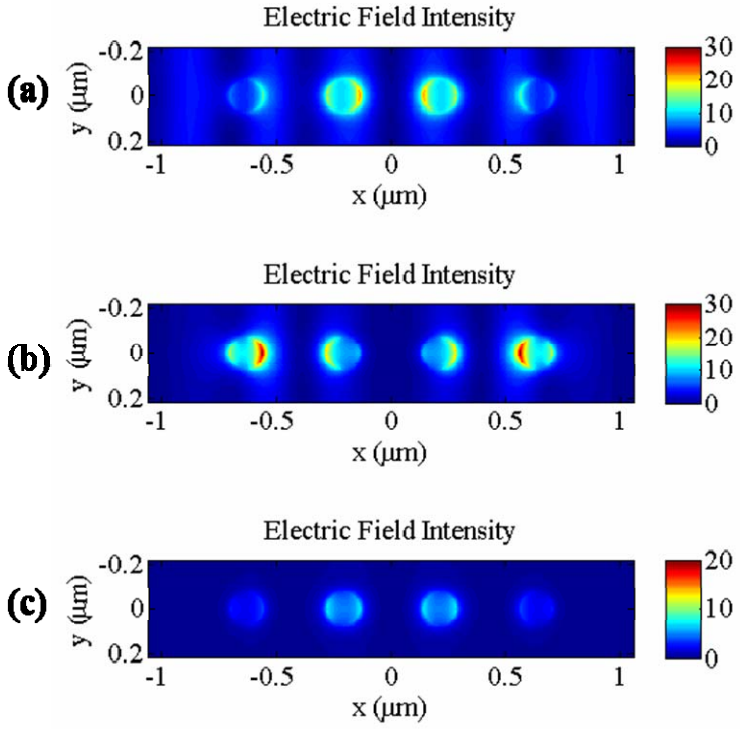

Figure 4.21 Electric field intensity enhancement distribution of the super-periodic nanohole array, 20 nm away from the surface of the metal film at wavelengths (a) 732.5 nm, (b) 749.5 nm and (c) 836.7 nm.

Next, the electric field intensity enhancement distributions of the resonances found in the zeroth order transmission and the first order diffraction of the super-periodic nanohole arrays are plotted in Figure 4.22. The field distribution of those resonances are compared against the surface plasmon modes seen in Figure 4.21 to determine which surface plasmon modes contribute the resonance observed in the far-field. Figure 4.22(a) and (b) plots the electric field intensity enhancement distribution of the resonance wavelengths, 731.5 nm and 835.7 nm. They are the resonance wavelengths observed in the first order diffraction. Figure 4.22(c) and (d) plots the electric field intensity enhancement distribution of the resonance wavelengths, 758.5 nm and 838.7 nm. These are the resonance wavelengths observed in the zeroth order transmission. Comparing the

Figure 4.22(a) with Figure 4.21(a), one can see that both the field distributions have similar patterns. Figure 4.22(c) and Figure 4.21(b) have the same patterns and lastly Figures 4.22(b) and (d) possess the same patterns as Figure 4.21(c). This means that the resonance observed in the first order diffraction at 731.5 nm is due to the surface plasmon mode excited at wavelength 732.5 nm. The discrepancy in wavelength values is due to the decrease in radiative damping. And the resonance observed in the zeroth order transmission at the wavelength 758.5 nm is due to the surface plasmon mode that is excited at the wavelength 749.5 nm. The shift to a longer wavelength is due to the increase in radiative damping. Lastly, the resonance wavelengths seen in the zeroth order transmission and first order diffraction at wavelengths, 835.7 nm and 838.7 nm, are due to the radiation of the surface plasmon mode at 836.7 nm as they share the same electric field intensity distribution.

Figures 4.21 and 4.22 implies that the surface plasmon mode excited at the wavelength of 732.5 nm only radiates strongly in the first order diffraction at the resonance wavelength of 731.5 nm and not in the zeroth order transmission, for at the resonance wavelength of 758.5 nm, the surface plasmon mode that was excited is different than the surface plasmon mode observed at the wavelength 732.5 nm. This is an indication that the resonances observed in the first order diffraction come mostly from the surface plasmon modes excited at the two inner holes, scattering more light at an angle. The resonances observed in the zeroth order transmission come from both the surface plasmon modes excited at all of the holes, but more so at the outer holes as shown in Figures 4.22(c) and (d).

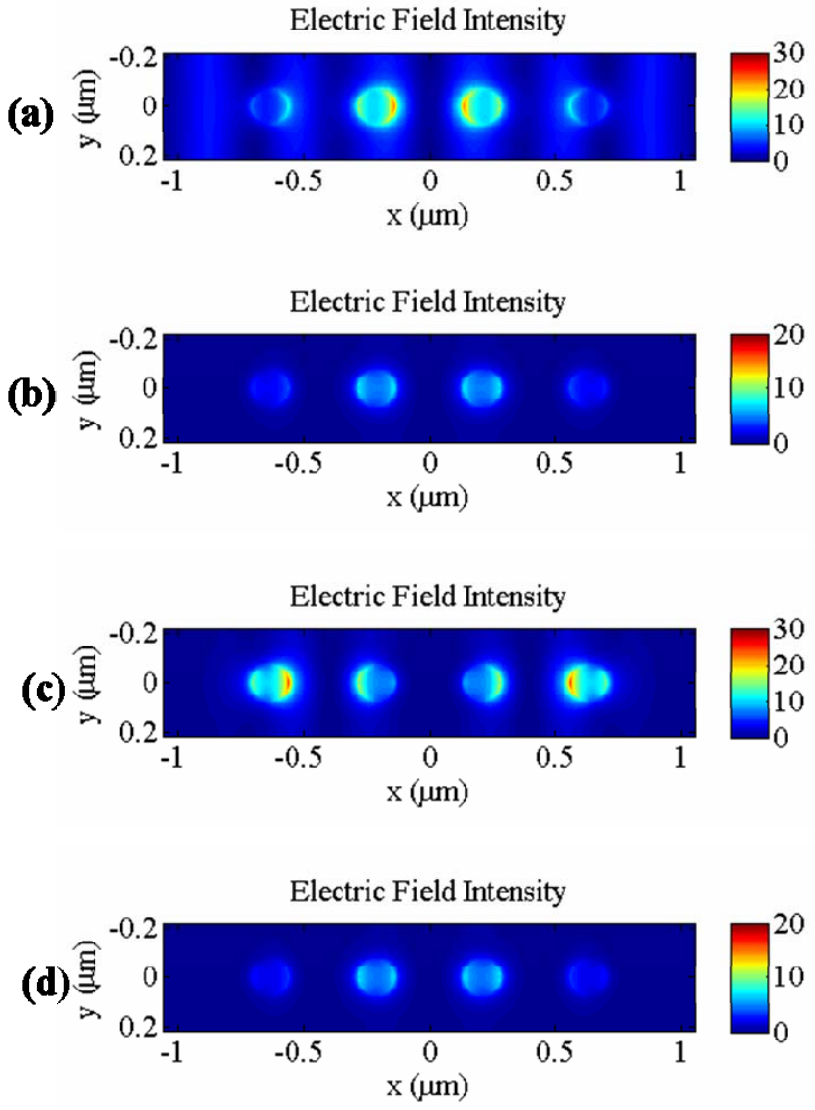

Figure 4.22 Electric field intensity enhancement distribution of the super-periodic nanohole array, 20 nm away from the surface of the metal film at wavelengths (a) 731.5 nm, (b) 835.7 nm, (c) 758.5 nm and (d) 838.7 nm.

The zeroth order transmission and the first order diffraction of the super-periodic nanohole arrays when illuminated with TM polarized light at normal incidence were confirmed experimentally. The same super-periodic nanohole arrays and the same experimental setup were used to obtain the spectrums of the zeroth order transmission and the first order diffraction. To change the polarization of the incident light from TE

polarization to TM polarization, the polarizer was simply rotated ninety degrees such that the electric field is perpendicular to the grating lines. To determine maximum diffraction was possible, the super-periodic nanohole arrays were aligned such that all of the beam power would fall within the total area of the device. The procedure that was used to determine the distance between the super-periodic nanohole arrays and the CCD during the TE polarization case was used in the TM polarization case. The distance between the CCD and the device was found to be 11.5055 mm. Figure 4.23 shows the false-color image of the first order diffraction captured by the CCD for TM polarization. Unlike, the image seen for TE polarization, there are three bright spots seen in the image. The color bar represents the amount of signal generated by the pixels.

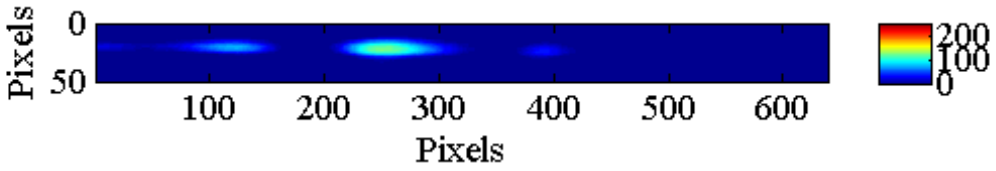

Figure 4.23 False-color image of the first order diffraction captured by the CCD when no chemical is present on the super-periodic nanohole array for TM polarization.

Once the image was captured, using the calibration process used in the TE polarization case, the image was then processed accordingly to obtain the first order diffraction spectrum of the device. The spectrum was normalized to the responsitivity of the CCD, a silicon detector but was not normalized to the spectrum of the broadband laser. The spectrum was generated by summing up the values in the vertical direction to include the energy in the beam that has diverged in the vertical direction. Figure 4.24 plots the signal generated from the CCD. As can be seen, the signal generated by the

CCD shows close resemblance with the first order diffraction obtained from the FDTD calculations. There are three distinct peaks at 610.5 nm, 728 nm and 838.1 nm.

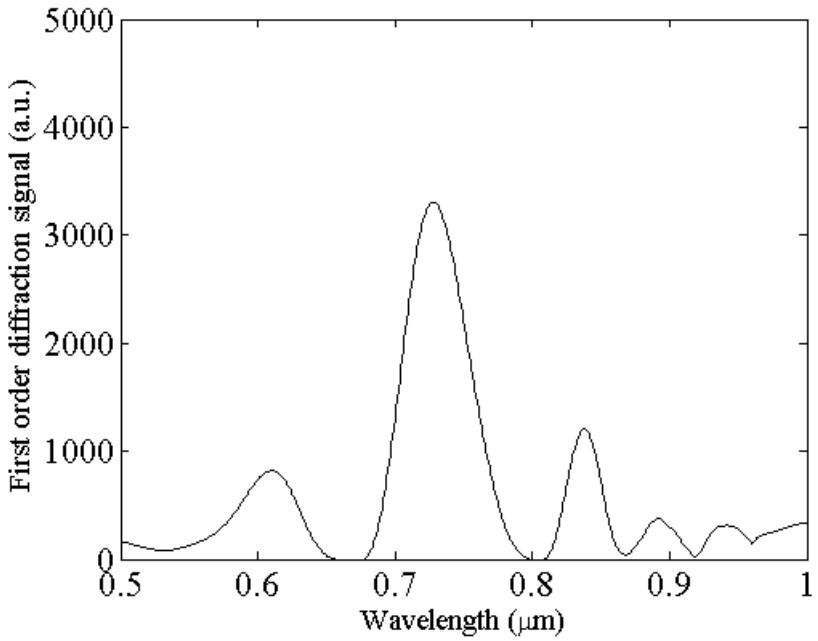

Figure 4.24 The first order diffraction signal after the calibration of the captured image in Figure 4.23.

The zeroth order transmission of the super-periodic nanohole arrays when illuminated with TM polarization is shown in Figure 4.25. The zeroth order transmission was obtained using the Ocean Optics USB 2000 spectrometer. From the plot, one can see two distinct peaks at 634.7 nm and at 758.3 nm. There is small but still discernable peak that occurs at the wavelength 836.8 nm. The resonance wavelength of 836.8 nm corresponds to the weakly excited surface plasmon mode as was discussed earlier. The jitters at the wavelength region from 900 nm to 1000 nm onwards were due to the lack of response of the silicon detector to the first order diffraction at those wavelengths.

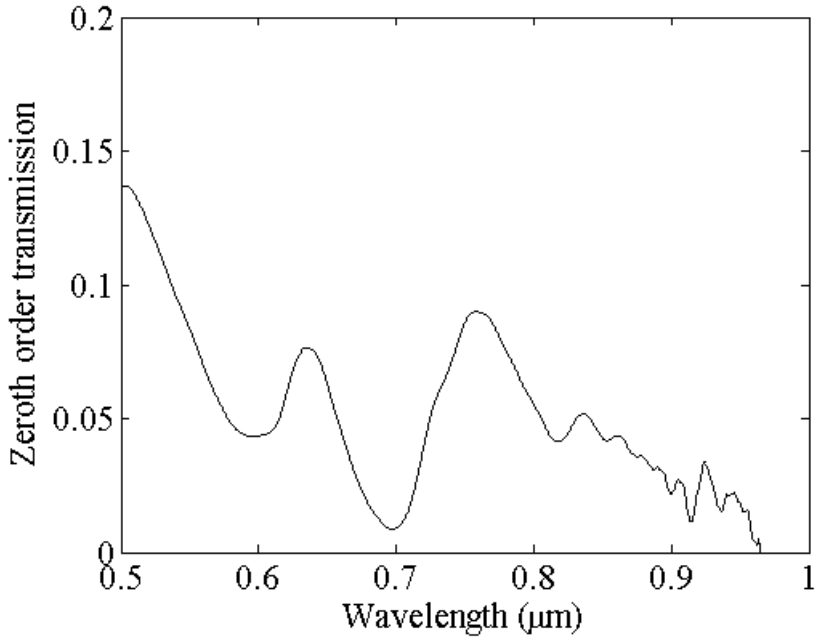

Figure 4.25 The zeroth order transmission from the super-periodic nanohole array when it is illuminated with TM polarized light.

Figure 4.26 helps compare the resonance wavelengths observed in the zeroth order transmission and the first order diffraction. The peaks at 600 nm region appears to not coincide well as they do in simulation but the position of the peak in the 700 nm region observed in the first order diffraction appears to be at right place relative to the peak observed in the zeroth order transmission. The peak in the first order diffraction is at a shorter wavelength than the peak in the zeroth order transmission. However, we find that the peak in the 800 nm region does not appear to be in the right position as expected from the FDTD calculations. The peak in the first order diffraction at the wavelength 838.1 nm is at a longer wavelength than the resonance observed in the zeroth order transmission. This appears to be inconsistent with the FDTD calculations and due to the radiation damping; it is supposed that first order diffraction peak should be at the shorter wavelength relative to the position of the zeroth order transmission peak. This

discrepancy with the FDTD calculations, although small could be due to the small errors in the calibration procedure.

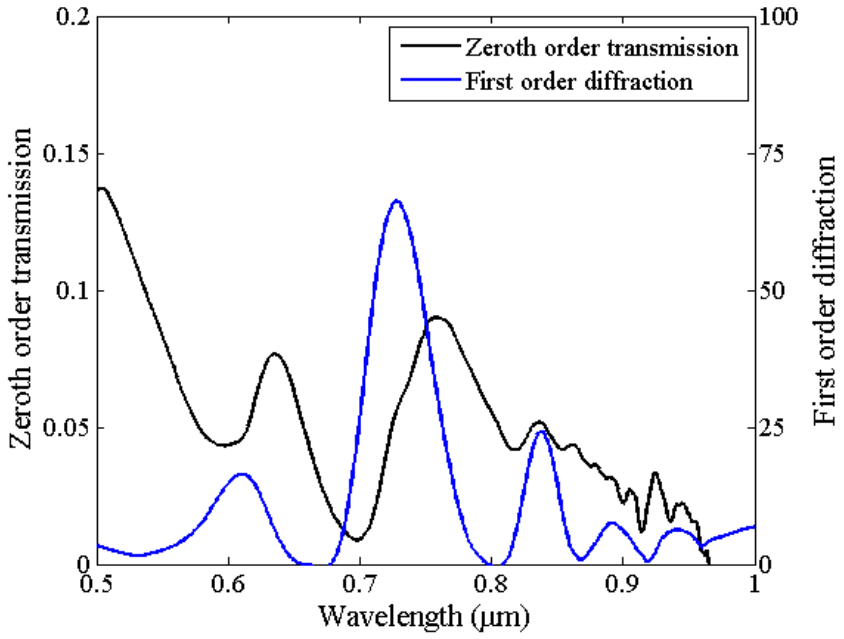

Figure 4.26 The zeroth order transmission of the super-periodic nanohole arrays when illuminated with TM polarized light.

The experimental results confirmed that the first order diffraction peak wavelength 728 nm is blue-shifted relative to the zeroth order transmission peak wavelength at 758.3 nm. And the difference between the simulation and experimental results are small, with less than 3 nm error.

Plasmonic devices are known to be good sensors for they are sensitive to the changes in the surface. The FWHM of the first diffraction order peak has a better smaller width than the zeroth order transmission which makes it easier to tell the shift in resonance wavelength. Here, the use of the super-periodic nanohole arrays when illuminated with TM polarized light as a sensor is investigated. Sensitivity here is defined as the slope in the change of resonance wavelength when a change in the refractive index

at the surface of the device is induced. And a figure-of-merit is designated to be the sensitivity divided by the FWHM of the resonance. Using FDTD calculations, the figure-of-merit of the super-periodic nanohole arrays versus regular hole arrays were computed and plotted in Figure 4.27. And it is clearly seen that due to the smaller FWHM of the resonance in the first order diffraction, the super-periodic nanohole arrays have an advantage over the regular periodic nanohole arrays.

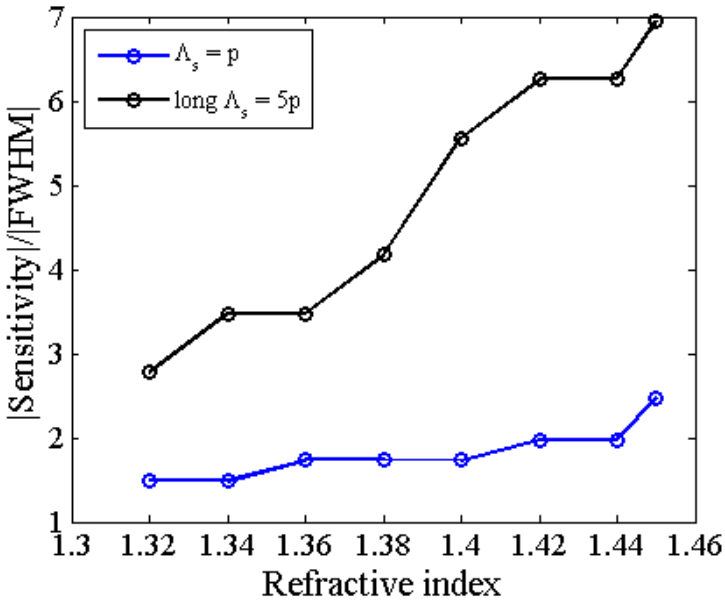

Figure 4.27 Figure-of-merit of the super-periodic nanohole arrays (black) and the regular periodic nanohole arrays.

An experiment to test the function of the super-periodic nanohole arrays were also carried out. Figure 4.28 show the false-color images when different chemicals are applied on the surface of the super-periodic nanohole array. Like the color images taken for TE polarization, the top, middle and bottom images correspond to the first order diffraction captured for air, methanol and IPA refractive index respectively. By simply comparing

the position of the bright spots for the different refractive index, it can be seen that all three bright spots shift to the right when methanol and IPA were applied.

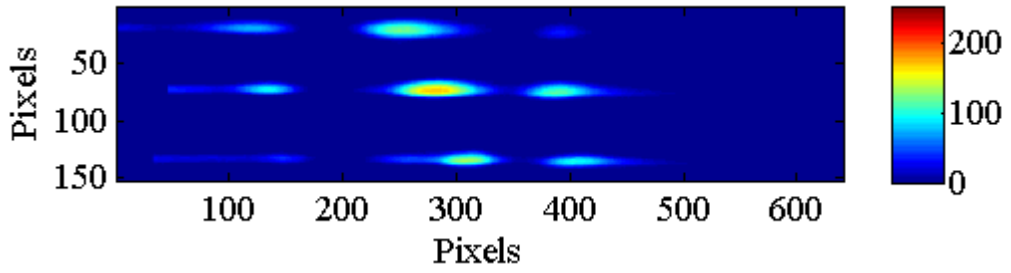

Figure 4.28 Angular dispersed first order diffraction captured by the CCD for TM polarization when the device was exposed (a) in the air, (b) methanol, and (c) isopropyl-alcohol.

Figure 4.29(a) shows the zeroth order transmission spectra for the different chemicals and Figure 4.29(b) shows the first order diffractions spectra for different chemicals. The vertical axis in Fig. 4.29(b) has an arbitrary unit that is proportional to the intensity of the first order diffraction. When chemicals were applied, the peak wavelengths in the first order diffraction shifted. It can be seen that the strength of the shorter wavelength resonance was reduced with increased refractive index. Tracking the resonance at the longer wavelength for first order diffraction, Figure 4.29(b), the resonance wavelength shifted from 728 nm (air) to 765.7 nm when methanol was applied and to 771.3 nm for IPA. Calculating the shift from methanol to IPA, the sensitivity is 301 nm/RIU. For the zeroth order transmission, tracking the resonance at the longer wavelength, the resonance wavelength shifted from 758.6 nm (air) to 771.3 nm when methanol is applied and to 777.5 nm when IPA is applied. Calculating the shift from methanol to IPA, the sensitivity is 127 nm/RIU.

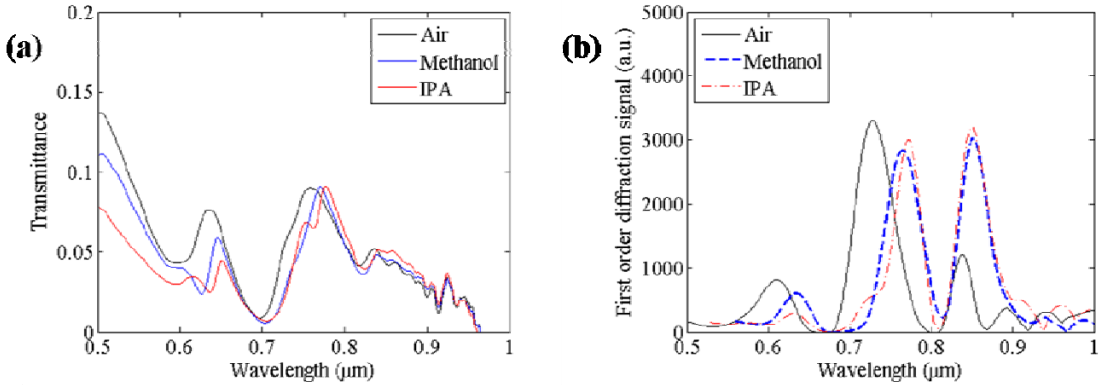

Figure 4.29 Measured surface plasmon resonance spectra with different chemical liquids applied in the super-period nanohole arrays from: (a) zeroth order transmission using a spectrometer, and (b) the first order diffraction using the CCD.

CHAPTER 5

SUMMARY

5.1 Summary

Surface plasmon resonance in subwavelength regular periodic metallic nanohole and nanoslit arrays is manifested as peaks in the zeroth order transmission. These resonances occur at wavelengths greater than the period of the arrays where all diffraction orders are evanescent. In this dissertation, a new surface plasmon resonance metal nanostructure concepts was proposed and was applied to the regular periodic metallic nanohole and nanoslit arrays. The surface plasmon resonances in the super-periodic nanoslit and nanohole arrays in metal films were investigated numerically and experimentally.

First, the surface plasmon resonance in super-periodic gold nanoslits array was investigated. The super-periodic nanoslits array has two periods in it. The small period which is subwavelength, provides the surface plasmon resonance while the large period or super-period provides the diffraction and the angular dispersion of the surface plasmon radiations. The zeroth order transmission and the first order diffraction versus the

wavelength from various super-period gold nanoslit arrays upon TM optical wave excitations were calculated. The peak diffraction wavelength in the first order diffraction is very close to but not exactly the same as the zeroth order transmission peak wavelength. The peak wavelength in first order diffraction is the same as the peak transmission wavelength of the regular nanoslit array with the same period. The resonance observed in the first order diffraction spectrum reveals more accurately the surface plasmon resonance in the super-period nanoslit device. It is also found that the change of the number of nanoslits in the unit cell of the super-period nanoslit array does not affect the surface plasmon resonance frequency. The surface plasmon resonance frequency is primarily controlled by the small period of nanoslits in the unit cell and does not change with the nanoslits width and the number of nanoslits in the super-period unit cell. The angular dispersion of the diffractions enables the surface plasmon resonance spectra to be measured with a CCD. And in the experiment, it was found that the surface plasmon resonance measured in the first order diffraction agrees well with what is measured in the zeroth-order transmission.

The surface plasmon resonance in super-period metal nanohole arrays was investigated by calculating resonance spectra of the zeroth order transmission, the first order diffraction, and the near field resonance. Unlike the super-periodic nanoslit arrays, the super-periodic nanohole arrays exude different transmission characteristics when illuminated with TE and TM polarized light.When illuminated with TE polarized light, there are two surface plasmon resonances seen in both the zeroth order transmission and in the first order diffraction. It is found that the first order diffraction resonance peak wavelength is slightly blue-shifted from the zeroth order transmission peak wavelength. It

is also found that the first order diffraction peak wavelength is approximately the same as the near field resonance wavelength although near field resonance wavelength slightly varies with the location of measurements.

When the super-periodic nanohole arrays were illuminated with TM polarized light, there are three resonances seen in both the zeroth order transmission and in the first order diffraction. Similar to the case when the device was illuminated with TE polarized light, the surface plasmon resonance observed in the first order diffraction is blue-shifted to the surface plasmon resonance observed in the zeroth order transmission. However, the resonance in the near-field spectrum is slightly red-shifted relative to the resonance in the first order diffraction. Through calculations, we find that the super-period grating vector splits the surface plasmon resonance mode of the nanohole array at the longer wavelength. And this mode splitting phenomenon is controlled by varying the super-period grating length.

Since surface plasmon resonance is widely used in the bio-chemical sensing field [114-125], the sensing characteristics of the super-periodic gold nanoslit and nanohole arrays are also studied. Because the surface plasmon resonance also appears in the first order diffraction, the super-periodic metallic nanostructures integrate the functions of a spectrometer and a surface plasmon sensor into a single device, performing them simultaneously. Also, it was found that the full-width at the half maximum (FWHM) of the resonance in the first order diffraction is narrower than the resonance in the zeroth order transmission. The surface plasmon resonance spectrometer can measure surface plasmon resonance from the spatially dispersed first order diffraction with a single shot CCD data image capture. These devices can be integrated with nano- and micro-fluidic

devices and are potentially useful for chemical and biomedical measurement and sensing applications. The findings in this work provide new insights to the surface plasmon resonance phenomena in super-period metal nanoslit arrays.

5.2 Suggested future works

While the properties of super-periodic metal nanohole and nanoslit arrays have been investigated by characterizing the transmission resonances observed in the zeroth order transmission and first order diffraction, more work can be done to further understand the behavior of surface plasmons in super-periodic metal nanostructures and to optimize the near and far field properties for bio-chemical sensing and filtering applications.

The studies of the super-periodic nanohole and nanoslit arrays thus far have demonstrated that the resonance wavelength in the first order diffraction does not coincide with the resonance wavelength in the zeroth order transmission and the resonance wavelength in the near-field spectrum. For all the cases, the resonance wavelengths observed in the first order diffraction are always blue-shifted relative to the resonance wavelengths in the zeroth order transmission. However, the difference between the resonance wavelengths in the first order diffraction and in the near-field is not the same. For the super-periodic nanohole array, when the structure is illuminated with TE polarized light, the resonance wavelength in the first order diffraction is red-shifted relative to the position of the resonance wavelength in the near-field spectrum, but when the super-periodic nanohole array is illuminated with TM polarized light, the resonance wavelength in the first order diffraction is slightly blue-shifted to the position of the resonance wavelength in the near-field spectrum. The inconsistency in wavelength

positions between the first order diffraction and the near-field spectrum makes it hard to pinpoint the cause of the shift in resonance wavelength. Determination of the reason behind the shift in resonance wavelength will present a better understanding of the mechanism of the resonances observed in the first order diffraction spectrum.

Super-periodicity can be applied to various metallic nanostructures, as was shown in this study. The super-periodicity effect was seen both in the nanoslit and in the nanohole arrays, where there are surface plasmon resonances in the first order diffraction with a narrower full-width at the half maximum (FWHM) than the FWHM seen in the zeroth order transmission. Hence, the application of the super-periodicity on other nanostructures that possess more enhanced near-field intensities such as the bowtie and I-shape apertures should be investigated as they provide better sensitivity than the nanoholes and nanoslits. Also, application of the super-periodic effect can be applied to nanostructures that surface plasmons resonance appears to be dip rather than a peak. Such nanostructures were not investigated here and it would be interesting to observe the kind of result one would have.

REFERENCES

[1] A. Ruivo, C. Gomes, A. Lima, M. L. Botelho, R. Melo, A. Belchior, and A. Pires de Matos, "Gold nanoparticles in ancient, and contemporary ruby glass," *Journal of Cultural Heritage*, vol. 9, pp. 134-137, 2008.

[2] R. W. Wood, "On a remarkable case of uneven distribution of light in a diffraction grating spectrum," *Proceedings of the Physical Society of London*, vol. 18, p. 269, 1902.

[3] U. Fano, "The theory of anomalous diffraction gratings, and of quasi-stationary waves on metallic surfaces (Sommerfeld's Waves)," *J. Opt.Soc. Am.*, vol. 31, pp. 213-222, 1941.

[4] D. Pines and D. Bohm, "A collective description of electron interactions: II. collective vs individual particle aspects of the interactions," *Physical Review*, vol. 85, p. 338, 1952.

[5] R. H. Ritchie, "Plasma losses by fast electrons in thin films," *Physical Review*,vol. 106, p. 874, 1957.

[6] E. A. Stern and R. A. Ferrell, "Surface plasma oscillations of a degenerate electron gas," *Physical Review*,vol. 120, p. 130, 1960.

[7] R. H. Ritchie, E. T. Arakawa, J. J. Cowan, and R. N. Hamm, "surface-plasmon resonance effect in grating diffraction," *Physical Review Letters*, vol. 21, p. 1530, 1968.

[8] E. Kretschmann and H. Raether, "Radiative decay of non-radiative surface plasmons excited by light," *Z. Naturforschung*, vol. 23A, pp. 2135-2136, 1968.

[9] A. Sommerfeld, "Über die Fortpflanzung electrodynamischer Wellen längs eines Drahtes," *Ann. Phys. und Chemie*, vol. 67, pp. 233-290, 1899.

[10] J. Zenneck, "Über die Fortpflanzung ebener elektromagnetischer Wellen längs einer ebenen Leiterfläche und ihre Beziehung zurdrahtlosen Telegraphie," *Ann. d. Phys*, vol. 23, pp. 846-866, 1907.

[11] J. A. Stratton, *Electromagnetic Theory*, New York, McGraw Hill Company, Inc. 1941.

[12] J. B. Pendry, L. Martín-Moreno, and F. J. Garcia-Vidal, "Mimicking surface plasmons with structured surfaces," *Science*, vol. 305, pp. 847-848, 2004.

[13] S. A. Maier, S. R. Andrews, L. Martín-Moreno, and F. J. Garcia-Vidal, "Terahertz surface plasmon-polariton propagation, and focusing on periodically corrugated metal wires," *Physical Review Letters*, vol. 97, p. 176805, 2006.

[14] W. L. Barnes, A. Dereux, and T. W. Ebbesen, "Surface plasmon subwavelength optics," *Nature*, vol. 424, pp. 824-830, 2003.

[15] H. T. Miyazaki, and Y. Kurokawa, "Squeezing visible light waves into a 3-nm-thick and 55-nm-long plasmon cavity," *Physical Review Letters*, vol. 96, p. 097401, 2006.

[16] T. W. Ebbesen, H. J. Lezec, H. F. Ghaemi, T. Thio, and P. A. Wolff, "Extraordinary optical transmission through sub-wavelength hole arrays," *Nature*, vol. 391, pp. 667-669, 1998.

[17] V. G. Veselago, "The electrodyanmics of substances with simultaneously negative values of ε and μ," *Sov. Phys. Usp*, vol. 10, pp. 509-514, 1968.

[18] J. B. Pendry, "Negative refraction makes a perfect lens," *Physical Review Letters*, vol. 85, p. 3966, 2000.

[19] J. B. Pendry, D. Schurig, and D. R. Smith, "Controlling electromagnetic fields," *Science*, vol. 312, pp. 1780-1782, 2006.

[20] U. Leonhardt, "Optical conformal mapping," *Science*, vol. 312, pp. 1777-1780, 2006.

[21] A. Andrea, and E. Nader, "Plasmonic and metamaterial cloaking: Physical mechanisms and potentials," *Journal of Optics A: Pure and Applied Optics*, vol. 10, p. 093002, 2008.

[22] H. Raether, *Surface Plasmon on Smooth and Rough Surfaces, and on Gratings*, Berlin, Springer-Verlag, 1988.

[23] S. A. Maier, *Plasmonics: Fundamental and Applications*, UK, Springer (2007.

[24] A. D. Rakic, A. B. Djuri?ic, J. M. Elazar, and M. L. Majewski, "Optical Properties of Metallic Films for Vertical-Cavity Optoelectronic Devices," *Appl. Opt*., vol. 37, pp. 5271-5283, 1998.

[25] E. D. Palik, *Handbook of Optical Constant of Solids*, Orlando, FL, Academic 1985.

[26] Baptiste Auguie , and W. L. Barnes, "Collective resonances in gold nanoparticle arrays," *Physical Review Letters*, vol. 101, pp. 143902, 2008.

[27] S. Zou and G. C. Schatz, "Narrow plasmonic/photonic extinction and scattering line shapes for one and two dimensional silver nanoparticle arrays," *The Journal of Chemical Physics*, vol. 121, pp. 12606-12612, 2004.

[28] W. L. Barnes, T. W. Preist, S. C. Kitson, and J. R. Sambles, "Physical origin of photonic energy gaps in the propagation of surface plasmons on gratings," *Physical Review B*, vol. 54, pp. 6227-6244, 1996.

[29] W. C. Tan, T. W. Preist, J. R. Sambles, and N. P. Wanstall, "Flat surface-plasmon-polariton bands and resonant optical absorption on short-pitch metal gratings," *Physical Review B*, vol. 59, pp. 12661-12666, 1999.

[30] I. R. Hooper and J. R. Sambles, "Dispersion of surface plasmon polaritons on short-pitch metal gratings," *Physical Review B*, vol. 65, pp. 165432, 2002.

[31] J. Chandezon, M. T. Dupuis, G. Cornet, and D. Maystre, "Multicoated gratings: A differential formalism applicable in the entire optical region," *J. Opt. Soc. Am*., vol. 72, pp. 839-846, 1982.

[32] J. A. Porto, Garc, iacute, F. J. a-Vidal, and J. B. Pendry, "Transmission Resonances on Metallic Gratings with Very Narrow Slits," *Physical Review Letters*, vol. 83, p. 2845, 1999.

[33] M. Masale, "The theory of attenuated total reflection by surface polaritons on one-sided corrugated thin films," *Physica B: Condensed Matter*, vol. 325, pp. 385-393, 2003.

[34] U. Schröter and D. Heitmann, "Grating couplers for surface plasmons excited on thin metal films in the Kretschmann-Raether configuration," *Physical Review B*, vol. 60, pp. 4992-4999, 1999.

[35] S. M. Rytov, "Electromagnetic properties of a finely stratified medium," *Soviet. Journal of Experimental and Theoretical Physics*, vol. 2, p. 8, 1956.

[36] J. Elser, V. A. Podolskiy, I. Salakhutdinov, and I. Avrutsky, "Nonlocal effects in effective-medium response of nanolayered metamaterials," *Applied Physics Letters,* vol. 90, pp. 191109-191103, 2007.

[37] J. Elser, R. Wangberg, V. A. Podolskiy, and E. E. Narimanov, "Nanowire metamaterials with extreme optical anisotropy," *Applied Physics Letters*, vol. 89, pp. 261102-261103, 2006.

[38] H. Kogelnik, "Coupled wave theory for thick hologram gratings," *The Bell System Technical Journal,* vol. 48, no.9, pp. 2909-2947, 1969.

[39] M. G. Moharam and T. K. Gaylord, "Rigorous coupled-wave analysis of planar-grating diffraction," *J. Opt. Soc. Am.*, vol. 71, pp. 811-818, 1981.

[40] M. G. Moharam, E. B. Grann, D. A. Pommet, and T. K. Gaylord, "Formulation for stable and efficient implementation of the rigorous coupled-wave analysis of binary gratings," *J. Opt. Soc. Am. A*, vol. 12, pp. 1068-1076, 1995.

[41] M. G. Moharam, D. A. Pommet, E. B. Grann, and T. K. Gaylord, "Stable implementation of the rigorous coupled-wave analysis for surface-relief gratings: enhanced transmittance matrix approach," *J. Opt. Soc. Am. A*, vol. 12, pp. 1077-1086, 1995.

[42] L. Li, "Formulation and comparison of two recursive matrix algorithms for modeling layered diffraction gratings," *J. Opt. Soc. Am. A*, vol. 13, pp. 1024-1035, 1996.

[43] T. Tamir, H. C. Wang, and A. A. Oliner, "Wave propagation in sinusoidally stratified dielectric media," *Microwave Theory and Techniques, IEEE Transactions*, vol. 12, pp. 323-335, 1964.

[44] C. B. Burckhardt, "Diffraction of a plane wave at a sinusoidally stratified dielectric grating," *J. Opt. Soc. Am.*, vol. 56, pp. 1502-1508, 1966.

[45] K. M. Byun, S. J. Yoon, D. Kim, and S. J. Kim, "Experimental study of sensitivity enhancement in surface plasmon resonance biosensors by use of periodic metallic nanowires," *Opt. Lett.*, vol. 32, pp. 1902-1904, 2007.

[46] J. Cesario, R. Quidant, G. Badenes, and S. Enoch, "Electromagnetic coupling between a metal nanoparticle grating and a metallic surface," *Opt. Lett.*, vol. 30, pp. 3404-3406, 2005.

[47] Y. Kanamori, K. Hane, H. Sai, and H. Yugami, "100 nm period silicon antireflection structures fabricated using a porous alumina membrane mask," *Applied Physics Letters*, vol. 78, pp. 142-143, 2001.

[48] S. Park, G. Lee, S. H. Song, C. H. Oh, and P. S. Kim, "Resonant coupling of surface plasmons to radiation modes by use of dielectric gratings," *Opt. Lett.*, vol. 28, pp. 1870-1872, 2003.

[49] H.-S. Leong, J. Guo, R. G. Lindquist, and Q. H. Liu, Surface plasmon resonance in nanostructured metal films under the Kretschmann configuration, *J. Applied Physics*, vol. 106, p. 124314, 2009.

[50] K. Yee, "Numerical solution of initial boundary value problems involving maxwell's equations in isotropic media," *IEEE Transactions on Antennas and Propagation* , vol. 14, pp. 302-307, 1966.

[51] F. J. García-Vidal, and J. B. Pendry, "Collective theory for surface enhanced raman scattering," *Physical Review Letters*, vol. 77, pp. 1163-1166, 1996.

[52] A. A. Maradudin, A. V. Shchegrov, and T. A. Leskova, "Resonant scattering of electromagnetic waves from a rectangular groove on a perfectly conducting surface," *Optics Communications*, vol. 135, pp. 352-360, 1997.

[53] M. B. Sobnack, W. C. Tan, N. P. Wanstall, T. W. Preist, and J. R. Sambles, "Stationary surface plasmons on a zero-order metal grating," *Physical Review Letters*, vol. 80, pp. 5667-5670, 1998.

[54] T. López-Rios, D. Mendoza, F. J. García-Vidal, J. Sánchez-Dehesa, and B. Pannetier, "Surface shape resonances in lamellar metallic gratings," *Physical Review Letters*, vol. 81, pp. 665-668, 1998.

[55] F. J. Garcia-Vidal, J. Sanchez-Dehesa, A. Dechelette, E. Bustarret, T. Lopez-Rios, T. Fournier, and B. Pannetier, "Localized surface plasmons in lamellar metallic gratings," *Journal of Lightwave Technology*, vol. 17, pp. 2191-2195, 1999.

[56] P. Lalanne, J. P. Hugonin, S. Astilean, M. Palamaru, and K. D. Möller, "One-mode model and Airy-like formulae for one-dimensional metallic gratings," *Journal of Optics A: Pure and Applied Optics*, vol. 2, p. 48, 2000.

[57] Q. Cao and P. Lalanne, "Negative role of surface plasmons in the transmission of metallic gratings with very narrow slits," *Physical Review Letters,* vol. 88, pp. 057403, 2002.

[58] Z. Sun, Y. S. Jung, and H. K. Kim, "Role of surface plasmons in the optical interaction in metallic gratings with narrow slits," *Applied Physics Letters,* vol. 83, pp. 3021-3023, 2003.

[59] Z. Sun, Y. S. Jung, and H. K. Kim, "Dynamic evolution of surface plasmon resonances in metallic nanoslit arrays," *Applied Physics Letters,* vol. 86, pp. 023111-023113, 2005.

[60] S. Collin, F. Pardo, R. Teissier, and J. L. Pelouard, "Strong discontinuities in the complex photonic band structure of transmission metallic gratings," *Physical Review B*, vol. 63, p. 033107, 2001.

[61] S. Astilean, P. Lalanne, and M. Palamaru, "Light transmission through metallic channels much smaller than the wavelength," *Optics Communications*, vol. 175, pp. 265-273, 2000.

[62] M. M. J. Treacy, "Dynamical diffraction explanation of the anomalous transmission of light through metallic gratings," *Physical Review B,* vol. 66, pp. 195105, 2002.

[63] A. M. Dykhne, A. K. Sarychev, and V. M. Shalaev, "Resonant transmittance through metal films with fabricated and light-induced modulation," *Physical Review B*, vol. 67, pp. 195402, 2003.

[64] Y. Xie, A. Zakharian, J. Moloney, and M. Mansuripur, "Transmission of light through slit apertures in metallic films," *Opt. Express*, vol. 12, pp. 6106-6121, 2004.

[65] P. Lalanne, J. P. Hugonin, and J. C. Rodier, "Theory of surface plasmon generation at nanoslit apertures," *Physical Review Letters*, vol. 95, p. 263902, 2005.

[66] D. Crouse, and P. Keshavareddy, "Polarization independent enhanced optical transmission in one-dimensional gratings and device applications," *Opt. Express*, vol. 15, pp. 1415-1427, 2007.

[67] Y. S. Jung, J. Wuenschell, H. K. Kim, P. Kaur, and D. H. Waldeck, "Blue-shift of surface plasmon resonance in a metal nanoslit array structure," *Opt. Express*, vol. 17, pp. 16081-16091, 2009.

[68] D. Pacifici, H. J. Lezec, H. A. Atwater, and J. Weiner, "Quantitative determination of optical transmission through subwavelength slit arrays in Ag films: Role of surface wave interference and local coupling between adjacent slits," *Physical Review B*, vol. 77, p. 115411, 2008.

[69] J. Wuenschell, and H. K. Kim, "Surface plasmon dynamics in an isolated metallic nanoslit," *Opt. Express*, vol. 14, pp. 10000-10013, 2006.

[70] K.-L. Lee, C.-W. Lee, W.-S. Wang, and P.-K. Wei, "Sensitive biosensor array using surface plasmon resonance on metallic nanoslits," *Journal of Biomedical Optics*, vol. 12, p. 044023, 2007.

[71] H. A. Bethe, "Theory of diffraction by small holes," *Physical Review*, vol. 66, p. 163, 1944.

[72] C. J. Bouwkamp, "Diffraction theory," *Reports on Progress in Physics*, vol. 17, p. 35, 1954.

[73] W. L. Barnes, W. A. Murray, J. Dintinger, E. Devaux, and T. W. Ebbesen, "Surface plasmon polaritons and their role in the enhanced transmission of light

through periodic arrays of subwavelength holes in a metal film," *Physical Review Letters*, vol. 92, p. 107401, 2004.

[74] K. J. K. Koerkamp, S. Enoch, F. B. Segerink, N. F. van Hulst, and L. Kuipers, "Strong influence of hole shape on extraordinary transmission through periodic arrays of subwavelength holes," *Physical Review Letters*, vol. 92, p. 183901, 2004.

[75] A. Degiron and T. W. Ebbesen, "The role of localized surface plasmon modes in the enhanced transmission of periodic subwavelength apertures," *Journal of Optics A: Pure and Applied Optics,* vol. 7, pp. 90, 2005.

[76] P. L. Rochon and L. Lévesque, "Standing wave surface plasmon mediated forward and backward scattering," *Opt. Express*, vol. 14, pp. 13050-13055, 2006.

[77] D. S. Kim, S. C. Hohng, V. Malyarchuk, Y. C. Yoon, Y. H. Ahn, K. J. Yee, J. W. Park, J. Kim, Q. H. Park, and C. Lienau, "Microscopic origin of surface-plasmon radiation in plasmonic band-gap nanostructures," *Physical Review Letters*, vol. 91, p. 143901, 2003.

[78] E. Altewischer, M. P. van Exter, and J. P. Woerdman, "Polarization analysis of propagating surface plasmons in a subwavelength hole array," *J. Opt. Soc. Am. B*, vol. 20, pp. 1927-1931, 2003.

[79] Q.-j. Wang, J.-q. Li, C.-p. Huang, C. Zhang, and Y.-y. Zhu, "Enhanced optical transmission through metal films with rotation-symmetrical hole arrays," *Applied Physics Letters*, vol. 87, pp. 091105-091103, 2005.

[80] H. Gao, J. Henzie, and T. W. Odom, "Direct evidence for surface plasmon-mediated enhanced light transmission through metallic nanohole arrays," *Nano Letters*, vol. 6, pp. 2104-2108, 2006.

[81] H. Gao, J. M. McMahon, M. H. Lee, J. Henzie, S. K. Gray, G. C. Schatz, and T. W. Odom, "Rayleigh anomaly-surface plasmon polariton resonances in palladium and gold subwavelength hole arrays," *Opt. Express*, vol. 17, pp. 2334-2340, 2009.

[82] W.-C. Liu and D. P. Tsai, "Optical tunneling effect of surface plasmon polaritons and localized surface plasmon resonance," *Physical Review B*, vol. 65, p. 155423, 2002.

[83] A. Degiron, H. J. Lezec, W. L. Barnes, and T. W. Ebbesen, "Effects of hole depth on enhanced light transmission through subwavelength hole arrays," *Applied Physics Letters*, vol. 81, pp. 4327-4329, 2002.

[84] J. Bravo-Abad, A. Degiron, F. Przybilla, C. Genet, F. J. Garcia-Vidal, L. Martin-Moreno, and T. W. Ebbesen, "How light emerges from an illuminated array of subwavelength holes," *Nature Physics*, vol. 2, pp. 120-123, 2006.

[85] Mart, iacute, L. n-Moreno, Garc, F. J. a-Vidal, H. J. Lezec, K. M. Pellerin, T. Thio, J. B. Pendry, and T. W. Ebbesen, "Theory of extraordinary optical transmission through subwavelength hole arrays," *Physical Review Letters*, vol. 86, p. 1114, 2001.

[86] E. Popov, M. Nevière, S. Enoch, and R. Reinisch, "Theory of light transmission through subwavelength periodic hole arrays," *Physical Review B*, vol. 62, pp. 16100-16108, 2000.

[87] A. K. Sarychev, V. A. Podolskiy, A. M. Dykhne, and V. M. Shalaev, "Resonance transmittance through a metal film with subwavelength holes," *IEEE Journal of Quantum Electronics*, vol. 38, pp. 956-963, 2002.

[88] P. Lalanne, J. C. Rodier, and J. P. Hugonin, "Surface plasmons of metallic surfaces perforated by nanohole arrays," *Journal of Optics A: Pure and Applied Optics*, vol. 7, p. 422, 2005.

[89] R. Müller, V. Malyarchuk, and C. Lienau, "Three-dimensional theory on light-induced near-field dynamics in a metal film with a periodic array of nanoholes," *Physical Review B*, vol. 68, p. 205415, 2003.

[90] H. Liu, and P. Lalanne, "Light scattering by metallic surfaces with subwavelength patterns," *Physical Review B*, vol. 82, p. 115418, 2010.

[91] S. G. Rodrigo, L. Martín-Moreno, A. Y. Nikitin, A. V. Kats, I. S. Spevak, and F. J. García-Vidal, "Extraordinary optical transmission through hole arrays in optically thin metal films," *Opt. Lett.*, vol. 34, pp. 4-6, 2009.

[92] H. Liu and P. Lalanne, "Microscopic theory of the extraordinary optical transmission," *Nature*, vol. 452, pp. 728-731, 2008.

[93] H. Liu and P. Lalanne, "Comprehensive microscopic model of the extraordinary optical transmission," *J. Opt. Soc. Am. A*, vol. 27, pp. 2542-2550, 2010.

[94] A. Y. Nikitin, Garc, iacute, F. J. a-Vidal, Mart, and L. n-Moreno, "Surface electromagnetic field radiated by a subwavelength hole in a metal Film," *Physical Review Letters*, vol. 105, p. 073902, 2010.

[95] S.-H. Chang, S. Gray, and G. Schatz, "Surface plasmon generation and light transmission by isolated nanoholes and arrays of nanoholes in thin metal films," *Opt. Express*, vol. 13, pp. 3150-3165, 2005.

[96] A. Krishnan, T. Thio, T. J. Kim, H. J. Lezec, T. W. Ebbesen, P. A. Wolff, J. Pendry, L. Martin-Moreno, and F. J. Garcia-Vidal, "Evanescently coupled resonance in surface plasmon enhanced transmission," *Optics Communications*, vol. 200, pp. 1-7, 2001.

[97] L. Salomon, F. Grillot, A. V. Zayats, and F. de Fornel, "Near-field distribution of optical transmission of periodic subwavelength holes in a metal film," *Physical Review Letters*, vol. 86, pp. 1110-1113, 2001.

[98] Y. Alaverdyan, B. Sepulveda, L. Eurenius, E. Olsson, and M. Kall, "Optical antennas based on coupled nanoholes in thin metal films," *Nat. Phys.*, vol. 3, pp. 884-889, 2007.

[99] J. Bravo-Abad, A. I. Fernández-Domínguez, F. J. García-Vidal, and L. Martín-Moreno, "Theory of extraordinary transmission of light through quasiperiodic arrays of subwavelength holes," *Physical Review Letters*, vol. 99, pp. 203905, 2007.

[100] R. Biswas, S. Neginhal, C. G. Ding, I. Puscasu, and E. Johnson, "Mechanisms underlying extraordinary transmission enhancement in subwavelength hole arrays," *J. Opt. Soc. Am. B*, vol. 24, pp. 2589-2596, 2007.

[101] A. Degiron, H. J. Lezec, N. Yamamoto, and T. W. Ebbesen, "Optical transmission properties of a single subwavelength aperture in a real metal," *Optics Communications*, vol. 239, pp. 61-66, 2004.

[102] Q. H. Park, "Optical antennas and plasmonics," *Contemporary Physics*, vol. 50, pp. 407-423, 2009.

[103] J. T. Robinson and M. Lipson, "Far-field control of radiation from an individual optical nanocavity: analogue to an optical dipole," *Physical Review Letters*, vol. 100, pp. 043902, 2008.

[104] J. Zuloaga and P. Nordlander, "On the energy shift between near-field and far-field peak intensities in localized plasmon systems," *Nano Letters*, vol. 11, pp. 1280-1283, 2011.

[105] R. Adato, A. A. Yanik, J. J. Amsden, D. L. Kaplan, F. G. Omenetto, M. K. Hong, S. Erramilli, and H. Altug, "Ultra-sensitive vibrational spectroscopy of protein monolayers with plasmonic nanoantenna arrays," *Proc. of the National Academy of Sciences*, vol. 106, pp. 19227-19232, 2009.

[106] D. Sinton, R. Gordon, and A. Brolo, "Nanohole arrays in metal films as optofluidic elements: progress and potential," *Microfluidics and Nanofluidics*, vol. 4, pp. 107-116, 2008.

[107] A. G. Brolo, R. Gordon, B. Leathem, and K. L. Kavanagh, "Surface plasmon sensor based on the enhanced light transmission through arrays of nanoholes in gold films," *Langmuir*, vol. 20, pp. 4813-4815, 2004.

[108] R. Gordon, D. Sinton, K. L. Kavanagh, and A. G. Brolo, "A New generation of sensors based on extraordinary optical transmission," *Accounts of Chemical Research*, vol. 41, pp. 1049-1057, 2008.

[109] K. L. Kelly, E. Coronado, L. L. Zhao, and G. C. Schatz, "The optical properties of metal nanoparticles: The influence of size, shape and dielectric environment," *The Journal of Physical Chemistry B*, vol. 107, pp. 668-677, 2002.

[110] B. M. Ross and L. P. Lee, "Comparison of near- and far-field measures for plasmon resonance of metallic nanoparticles," *Opt. Lett.*, vol. 34, pp. 896-898, 2009.

[111] N. K. Grady, N. J. Halas, and P. Nordlander, "Influence of dielectric function properties on the optical response of plasmon resonant metallic nanoparticles," *Chemical Physics Letters*, vol. 399, pp. 167-171, 2004.

[112] M. A. Kats, N. Yu, P. Genevet, Z. Gaburro, and F. Capasso, "Effect of radiation damping on the spectral response of plasmonic components," *Opt. Express*, vol. 19, pp. 21748-21753, 2011.

[113] C. Dahmen, B. Schmidt, and G. Von Plessen, "Radiation damping in metal nanoparticle pairs," *Nano Letters*, vol. 7, pp. 318-322, 2007.

[114] L. Pang, H. M. Chen, L. Wang, J. M. Beechem, and Y. Fainman, "Controlled detection in composite nanoresonant array for surface plasmon resonance sensing," *Opt. Express*, vol. 17, pp. 14700-14709, 2009.

[115] H. M. Chen, L. Pang, A. Kher, and Y. Fainman, "Three-dimensional composite metallodielectric nanostructure for enhanced surface plasmon resonance sensing," *Applied Physics Letters*, vol. 94, pp. 073117-073113, 2009.

[116] G. M. Hwang, P. Lin, E. H. Mullen, and Y. Fainman, "Plasmonic sensing of biological analytes through nanoholes," *Sensors Journal, IEEE*, vol. 8, pp. 2074-2079, 2008.

[117] L. Pang, G. M. Hwang, B. Slutsky, and Y. Fainman, "Spectral sensitivity of two-dimensional nanohole array surface plasmon polariton resonance sensor," *Applied Physics Letters*, vol. 91, pp. 123112-123113, 2007.

[118] K. A. Tetz, L. Pang, and Y. Fainman, "High-resolution surface plasmon resonance sensor based on linewidth-optimized nanohole array transmittance," *Opt. Lett.*, vol. 31, pp. 1528-1530, 2006.

[119] J. N. Anker, W. P. Hall, O. Lyandres, N. C. Shah, J. Zhao, and R. P. Van Duyne, "Biosensing with plasmonic nanosensors," *Nat. Materials*, vol. 7, pp. 442-453, 2008.

[120] C. E. H. Berger, T. A. M. Beumer, R. P. H. Kooyman, and J. Greve, "Surface plasmon resonance multisensing," *Analytical Chemistry*, vol. 70, pp. 703-706, 1998.

[121] C. Boozer, G. Kim, S. Cong, H. Guan, and T. Londergan, "Looking towards label-free biomolecular interaction analysis in a high-throughput format: a review of new surface plasmon resonance technologies," *Current Opinion in Biotechnology*, vol. 17, pp. 400-405, 2006.

[122] X. D. Hoa, A. G. Kirk, and M. Tabrizian, "Towards integrated and sensitive surface plasmon resonance biosensors: A review of recent progress," *Biosensors and Bioelectronics*, vol. 23, pp. 151-160, 2007.

[123] J. Homola, "Surface plasmon resonance sensors for detection of chemical and biological species," *Chemical Reviews*, vol. 108, pp. 462-493, 2008.

[124] B. Liedberg, C. Nylander, and I. Lunström, "Surface plasmon resonance for gas detection and biosensing," *Sensors and Actuators*, vol. 4, pp. 299-304, 1983.

[125] J. Ji, J. G. O'Connell, D. J. D. Carter, and D. N. Larson, "High-throughput nanohole array based system to monitor multiple binding events in real time," *Analytical Chemistry*, vol. 80, pp. 2491-2498, 2008.